



Terms and Conditions of Use of Digitised Theses from Trinity College Library Dublin

Copyright statement

All material supplied by Trinity College Library is protected by copyright (under the Copyright and Related Rights Act, 2000 as amended) and other relevant Intellectual Property Rights. By accessing and using a Digitised Thesis from Trinity College Library you acknowledge that all Intellectual Property Rights in any Works supplied are the sole and exclusive property of the copyright and/or other IPR holder. Specific copyright holders may not be explicitly identified. Use of materials from other sources within a thesis should not be construed as a claim over them.

A non-exclusive, non-transferable licence is hereby granted to those using or reproducing, in whole or in part, the material for valid purposes, providing the copyright owners are acknowledged using the normal conventions. Where specific permission to use material is required, this is identified and such permission must be sought from the copyright holder or agency cited.

Liability statement

By using a Digitised Thesis, I accept that Trinity College Dublin bears no legal responsibility for the accuracy, legality or comprehensiveness of materials contained within the thesis, and that Trinity College Dublin accepts no liability for indirect, consequential, or incidental, damages or losses arising from use of the thesis for whatever reason. Information located in a thesis may be subject to specific use constraints, details of which may not be explicitly described. It is the responsibility of potential and actual users to be aware of such constraints and to abide by them. By making use of material from a digitised thesis, you accept these copyright and disclaimer provisions. Where it is brought to the attention of Trinity College Library that there may be a breach of copyright or other restraint, it is the policy to withdraw or take down access to a thesis while the issue is being resolved.

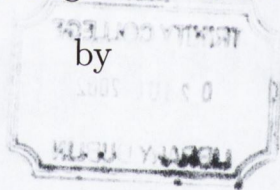
Access Agreement

By using a Digitised Thesis from Trinity College Library you are bound by the following Terms & Conditions. Please read them carefully.

I have read and I understand the following statement: All material supplied via a Digitised Thesis from Trinity College Library is protected by copyright and other intellectual property rights, and duplication or sale of all or part of any of a thesis is not permitted, except that material may be duplicated by you for your research use or for educational purposes in electronic or print form providing the copyright owners are acknowledged using the normal conventions. You must obtain permission for any other use. Electronic or print copies may not be offered, whether for sale or otherwise to anyone. This copy has been supplied on the understanding that it is copyright material and that no quotation from the thesis may be published without proper acknowledgement.

Surface reconstructions of $\text{Fe}_3\text{O}_4(001)$

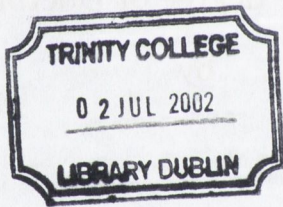
A thesis submitted to the University of Dublin, Trinity College,
in application for the degree of Doctor in Philosophy



Guido Mariotto

Physics Department
Trinity College Dublin

October 2001



Thesis
6751

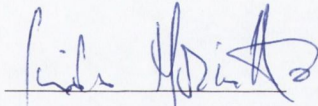
Declaration

This thesis is submitted by the under signed for the degree of Doctor in Philosophy at the University of Dublin.

It has not been submitted as an exercise for a degree at any other university.

Apart from the advice, assistance and joint effort mentioned in the under signed and in the text, this thesis is entirely my own work.

I agree that the library may lend or copy this thesis freely on request.



Guido Mariotto

October 2001

Acknowledgements

I would like to thank my supervisor Prof. I.V. Shvets for giving me the opportunity of working in his group and introducing me to the field of surface science. I much appreciated the independence I benefited of during my research and the discussions and encouragement he gave me during the past four years. I'd also like to thank his wife Irina and their family for welcoming the group into their house.

A great contribution to what I learned about magnetite goes to Dr. Ciarán Seoighe, who also taught me the difficult art of transferring tips and samples inside a UHV chamber. I'd like to thank Dr. Shane Murphy for introducing me to the UHV world; I am indebted to him for many useful discussions and good ideas. Thanks too to Dr. Jürgen Osing, for his help during my early days. I would like to acknowledge all members of the Nanotechnology group, past and present; Roman Kantor, who started his Ph.D. with me and was my rival in endless squash games; Anselm Gademann, who welcomed me in his house for dinners and parties; Dmitry Kashanin, for his help in programming and electronics and the "Vodka" dinners; Sergei Makarov for his help during the Nanojet project; Luca Seravalli, who shared with me the joys and sorrows of living abroad; William Signac, the master of capillary pulling; Vivienne Williams for bringing a feminine touch in a lads' world; Diarmaid MacMathuna for taking over magnetite; Viktor Oussov for relieving me of the "lustrous film"; Sergio "el gato" Ceballos who has brought some Mediterranean flavor in the lab; Alex, Ken and Giuseppe for bringing new enthusiasm in the group. Thanks too, to the visiting researchers Yuri, Michael and Nicolai and the summer students Marie and Michael for making my job easier and more enjoyable.

The group could not operate without the efforts of all the departmental staff; Tom Burke, John Kelly, Jim Kavanagh, Dave Grouse, James Egan, Mick Reilly, Ken Concannon, Joe McCauley, Pat Flanagan, Jackie Ballentine-Armstrong, Chris Smith and all the secretarial staff, especially Liz, Natalie, Michelle, Marie and Elaine.

Thanks to all my friends outside the physics world who enlightened my social life. Chisco”the night bike-rider”Ruiz was always ready to cheer me up when I was in a bad mood; Geoff Coy was a tough challenger on the climbs of Irish hills and mountains. The suffering of hours of *StarTrek* they subjected me to was fully repaid by their friendship. Bettina, for challenging the physics laws by pirouetting into the Liffey. Valerie, for her delicious dinners. Jeremy, for taking a photograph of a ”provolone” and Micha for her pink bike. Thank you to my friends from Italy for keeping in touch and supporting me.

Thank you to my Julia, who coped with our long-distance relationship and visited me and supported me when I needed her.

Finally, I would like to thank my family, my parents Angelo and Angela and my brother Andrea. They always respected my decisions and supported me to get through rough times. This thesis is dedicated to them.

Abstract

In this thesis, the (001) surface of magnetite artificial single crystals has been studied using low-energy electron diffraction (LEED), Auger electron spectroscopy (AES) and Scanning Tunneling Microscopy (STM). STM investigations were carried out in constant current mode at room temperature using non-magnetic tips (PtIr and W) and antiferromagnetic tips (MnNi). Extensive investigation was used to find an adequate sample preparation procedure. Although several methods have been proposed, ranging from in-situ cleavage to annealing in Ultra High Vacuum (UHV) or in an oxygen partial pressure, to Ar⁺ sputtering, each of these methods has drawbacks, and the preparation parameters (such as annealing temperature and oxygen partial pressure) may vary drastically according to the type of system used, whether single crystals or thin films.

Two different procedures were used to prepare the crystals surface. A mechanical polishing of the crystal, followed by annealing in UHV, gave rise to a contamination of the surface; the main contaminants detected by AES were Ca and K. LEED provided evidence of a p(1×4) reconstruction of the surface, which was visible in the STM images as domains of long rows running along the <110> directions and separated by about four times the length of the primitive unit cell. A 1.0 ± 0.1 Å step height between adjacent terraces was observed, indicating some degree of intermixing between tetrahedral and octahedral planes. A significant amount of calcium was detected on the surface, which points to a non-stoichiometric surface. We believe this reconstruction is driven by the segregation of Ca from the bulk as a consequence of the annealing, leading to the formation of a Ca_xFe_{3-x}O₄-like compound.

A combination of Ar⁺ sputtering, annealing in oxygen partial pressure

and in UHV produced a magnetite surface where no contaminants were detected by our AES setup. A $(\sqrt{2} \times \sqrt{2})R45^\circ$ was routinely observed by LEED measurements. Large and atomically flat terraces, separated by integer multiples of $2.1 \pm 0.2 \text{ \AA}$ were imaged with STM. We believe that the surface of the crystal is terminated at the B plane, exposing rows of Fe^{2+} and Fe^{3+} ions in octahedral sites. Atomic resolution was achieved on several terraces using antiferromagnetic MnNi tips, showing Fe rows separated by $\sim 6 \text{ \AA}$ running along the $[110]$ direction. Anomalous corrugations of $\sim 6 \text{ \AA}$ and 12 \AA were measured along these rows, instead of the expected 3 \AA separation. A possible explanation of this anomaly is a "Wigner localization" leading to a static arrangement of pairs of Fe^{2+} and pairs of Fe^{3+} ions. The different spin polarization of the two Fe species may have been resolved by the antiferromagnetic probe, which acts like a spin filter providing magnetic contrast.

Publications

G. Mariotto, S. Murphy and I.V. Shvets. *Charge ordering on the surface of $Fe_3O_4(001)$* . *Phys. Rev. B*, to be submitted.

J. Voigt, B. Reinker, I.W. Rangelow, G. Mariotto, I.V. Shvets, P. Güthner, H. Löschner. *Nanojet: Nanostructuring via a downstream plasmajet*. *J. Vac. Sci. Technol.*, B 17(6):1, 1999

G. Mariotto, M. D'Angelo and I.V. Shvets. *Dynamic behavior of a piezowalker, inertial and frictional configurations*. *Rev. Sci. Instrum.*, 70(9):3651, 1999

G. Mariotto, M. D'Angelo, J. Kresnin and I.V. Shvets. *Study of the dynamic behaviour of a piezo-walker*. *Appl. Surf. Sci.*, 144-145:530, 1999

List of abbreviations

1D - one dimensional

2D - two dimensional

3D - three dimensional

AES - Auger electron spectroscopy

AF - antiferromagnetic

b.c.c. - body centered cubic

CMA - cylindrical mirror analyzer

DOS - density of states

e -beam - electron beam

E_F - Fermi energy

ESD - electron stimulated desorption

f.c.c. - face centered cubic

HOPG - highly oriented pyrolytic graphite

L - Langmuir

LDOS - local density of states

LEIS - low energy ion scattering

LEED - low energy electron diffraction

LT - low-temperature

LTSTM - low-temperature scanning tunneling microscopy

MBE - molecular beam epitaxy

ML - monolayer

O.D. - outer diameter
OFHC - oxygen free high conductivity
PZT - lead zirconium titanate
RFA - retarding field analyzer
RHEED - reflection high energy electron diffraction
RT - room temperature
RTSTM - room-temperature scanning tunneling microscopy
SPM - scanning probe microscopy
SPSTM - spin polarized scanning tunneling microscopy
SRO - short range order
STM - scanning tunneling microscopy
STS - scanning tunneling spectroscopy
TMR - tunneling magneto resistance
TSP - titanium sublimation pump
UHV - ultra high vacuum
XPD - X-ray photoelectron diffraction
XPS - X-ray photoelectron spectroscopy
XRD - X-ray diffraction

List of Figures

2.1	Top view schematic of the UHV system	4
2.2	Schematic of the resistive heater	8
2.3	Schematic illustration of the e -beam heater	10
2.4	Schematic illustration of the e -beam evaporator	12
2.5	Schematic representation of a STM tunneling junction	16
2.6	Schematic illustration of a STM head	18
2.7	Schematic of four-grid optics in LEED mode	20
2.8	Laue diffraction from a one-dimensional array of scatterers	21
2.9	Laue diffraction from a one-dimensional array of scatterers	23
2.10	Schematic of LEED screen geometry	25
2.11	Top view of the (001) surface of magnetite showing only the O^{2-} ions	26
2.12	The $p(1\times 1)$ and the $(\sqrt{2}\times\sqrt{2})R45^\circ$ surface structures in real and reciprocal space	27
2.13	LEED pattern of a clean $Fe_3O_4(001)$ surface. $E = 93$ eV	28
2.14	Schematic illustration of a cylindrical mirror analyser	29
2.15	Schematic of the sample stage for AES analysis	31
3.1	Applications of iron oxides	38
3.2	$FeO-Fe_2O_3$ phase diagram	39

3.3	Unit cell of wüstite	40
3.4	Unit cell of magnetite	42
3.5	Unit cell of hematite	43
4.1	Ionic model	46
4.2	Oxygen bonds with Fe atoms	48
4.3	(a): Fe _{tetr} -O bonds. (b): Fe _{oct} -O bonds	49
4.4	Bulk-terminated surface: full A layer	51
4.5	Bulk-terminated surface: full B layer	52
4.6	Tetrahedrally terminated surface: half-filled A layer	53
4.7	Octahedrally terminated surface: oxygen vacancies in the B layer	55
5.1	X-ray powder diffractogram	59
5.2	<i>R vs. T</i> curve for an artificial Fe ₃ O ₄ crystal	61
5.3	Auger spectrum after UHV annealing at 990 ± 50 K for a total of 36 hours	66
5.4	Auger spectrum after mechanical polishing	69
5.5	Auger spectrum after annealing in UHV at 1030 ± 50 K for ~ 20 hours	71
5.6	Auger spectrum after Ar ⁺ ion sputtering	72
5.7	Auger spectrum after annealing in UHV at 990 ± 50 K for ~ 2 hours following the Ar ⁺ ion sputtering	73
5.8	Reference Auger spectra of FeO, Fe ₃ O ₄ and Fe ₂ O ₃	75
5.9	Fe(MVV) Auger spectra after 360 L O ₂ exposure at various temperatures.	76
5.10	Fe(MVV) Auger lineshape changes after a 2160 L oxygen ex- posure at 990 K ± 50 K	79

5.11	O(509 eV) Auger spectra.	81
5.12	Fe(649 eV, 701 eV) Auger spectra.	82
5.13	Fe(MVV) Auger lineshape changes after a long annealing in UHV	84
6.1	First annealing cycle. Auger spectrum after a 4 hours UHV annealing at 990 ± 50 K	88
6.2	(a) First annealing cycle. LEED pattern observed with a primary electron energy of 93 eV. (b) Schematic of a p(1×4) reconstruction LEED pattern	89
6.3	(2000×2000) Å ² (a) and (800×800) Å ² (b) STM image of a p(1×4) reconstructed surface of Fe ₃ O ₄ (001)	91
6.4	(600×600) Å ² (a) and (400×400) Å ² (b) STM image of a p(1×4) reconstructed surface of Fe ₃ O ₄ (001).	92
6.5	Second annealing cycle. Auger spectrum of Fe ₃ O ₄ (001) after a further 18 hours UHV annealing at 990 ± 50 K	94
6.6	LEED pattern of Fe ₃ O ₄ (001) after a further 18 hours UHV annealing at 990 ± 50 K	95
6.7	(a) (2000×2000) Å ² STM image. (b) (1000 × 750) Å ² STM image showing a 1 Å and a 2 Å step height between different terraces. (c) Line profile taken along the scan line labelled <i>t-t</i>	98
6.8	(a) (600×600) Å ² STM image showing a 90° rotation between two terraces separated by 2.1 ± 0.2 Å. (b) Line profile taken along the scan line labelled <i>v-v</i> . (c) (1000 × 1000) Å ² image showing domains with rows oriented at a $\pm 60^\circ$ angle with the <110> directions. (d) (330 × 530) Å ² image. The domains are separated by rows running along the <1 $\bar{1}$ 0> directions.	99
6.9	(2000×2000) Å ² STM image after the third annealing cycle	100

6.10	Fourth annealing cycle. Auger spectrum of $\text{Fe}_3\text{O}_4(001)$ after a 14 hours UHV annealing at 1030 ± 50 K	101
6.11	(a) LEED pattern of $\text{Fe}_3\text{O}_4(001)$ after a 14 hours UHV annealing at 1030 ± 50 K. (b) (2000×2000) \AA^2 STM image after the fourth annealing cycle	102
6.12	(a) (200×200) \AA^2 STM image of a $p(1 \times 4)$ reconstructed surface of a natural $\text{Fe}_3\text{O}_4(001)$ single crystal. (b) Line profile along the a–b line	105
7.1	LEED pattern of a clean $\text{Fe}_3\text{O}_4(001)$ surface. $E = 52$ eV . . .	111
7.2	3D view of a (1000×1000) \AA^2 image	113
7.3	(a) (770×1000) \AA^2 image. (b) Line profile. (c) (620×800) \AA^2 image. (d) Line profile.	114
7.4	(a) 2D view of a (300×400) \AA^2 image. (b) Line profile. (c) 3D view of the same image. (d) Line profile.	116
7.5	Atomically resolved (140×210) \AA^2 STM image	119
7.6	(a) Atomically resolved (70×70) \AA^2 STM. (b) Line profile . . .	120
7.7	3D view of terraces "2" and "3". The insert reveals an atomically resolved structure	122
7.8	3D view of terraces "2", "3" and "4". The insert reveals an atomically resolved structure	123
7.9	(a), (b) 3D views of terraces "3" and "4". (c) 2D view of a (95×140) \AA^2 image. (d) Line profile	125
7.10	Mizoguchi's patterns of Fe_3O_4	129
7.11	Schematic model of the structure proposed by Voogt	131
7.12	Schematic model of the structure observed in fig. 7.6	132
A.1	Calibration curve for the resistive heater	140

B.1 (30×30) Å² image of HOPG 143

B.2 Warped image of HOPG 144

List of Tables

2.1	Typical parameters for Ar ⁺ ion etching of W STM tips	34
5.1	Typical parameters for Ar ⁺ ion etching of a Fe ₃ O ₄ (001) surface	68
5.2	Typical parameters for the preparation of a Fe ₃ O ₄ (001) surface	70
6.1	Contamination levels of potassium and calcium after four an- nealing cycles in UHV at various temperatures	93

Contents

1	Introduction	1
2	Experimental details	3
2.1	The experimental setup	3
2.1.1	The STM	13
2.1.2	Four-grid LEED/AES optics	18
2.1.3	Cylindrical-Mirror Analyzer for AES	29
2.2	STM tips	33
3	Iron oxides	37
3.1	Introduction	37
3.2	Wüstite, Fe_{1-x}O	40
3.3	Magnetite, Fe_3O_4	41
3.4	Maghemite, $\gamma\text{-Fe}_2\text{O}_3$	42
3.5	Hematite, $\alpha\text{-Fe}_2\text{O}_3$	43
4	The (001) surface of Fe_3O_4	44
4.1	Introduction	44
4.2	The electrostatic model	45
4.3	The electron counting model	47
4.3.1	Fe–O dangling bonds	47

4.3.2	Tetrahedrally bulk-terminated surface: full <i>A</i> layer	50
4.3.3	Octahedrally bulk-terminated surface: full <i>B</i> layer	50
4.3.4	Tetrahedrally terminated surface: half-filled <i>A</i> layer	52
4.3.5	Octahedrally terminated surface: oxygen vacancies in the <i>B</i> layer	54
4.4	Literature review	56
5	Characterization and preparation	58
5.1	Introduction	58
5.2	Mechanical polishing	62
5.3	Annealing in UHV	63
5.4	Ar ⁺ ion sputtering and annealing	68
5.5	AES analysis	74
6	p(1×4) reconstruction on Fe₃O₄(001)	86
6.1	Introduction	86
6.2	Experimental results	86
6.2.1	First annealing cycle	87
6.2.2	Second annealing cycle	93
6.2.3	Third annealing cycle	100
6.2.4	Fourth annealing cycle	101
6.2.5	p(1×4) reconstruction on a natural Fe ₃ O ₄ (001) single crystal	103
6.3	Conclusion	106

7 Atomic-scale contrast on Fe₃O₄(001)	109
7.1 Introduction	109
7.2 LEED data	111
7.3 STM data	112
7.4 Discussion	126
8 Summary	134
8.1 Conclusion	134
8.2 Further work	136
A Heater calibration curve	139
B STM calibration	141

Chapter 1

Introduction

Iron oxides are of fundamental importance in several technological applications associated with molecular geochemistry, corrosion and catalysis. Magnetite in particular, due to its peculiar magnetic properties, plays a crucial role in many electronics and magneto-recording applications. Although magnetite was the subject of intensive studies in the last decades, many of its electronic and magnetic properties are not well understood, and they seem to strongly depend on the stoichiometry and the purity of the crystals used. Since the electro-magnetic properties are intimately related to the atomic geometry of a surface, the knowledge of its structure on an atomic scale is of fundamental importance. In this respect, the invention of Scanning Probe Microscopy (SPM) provided a powerful tool for the investigation of surfaces. In the last decade, the possibility of applying SPM to obtain atomic scale information on the magnetic structure of surfaces was investigated; one of these techniques, involving the use of an Scanning Tunneling Microscope (STM), is referred to as Spin-Polarized Scanning Tunneling Microscope (SPSTM) [1–8]. A relatively high conductivity at room temperature ($\sim 200 \Omega^{-1}\text{cm}^{-1}$) [9] makes STM investigations of magnetite possible. Furthermore, magnetite

was theoretically predicted to be a half-metallic ferromagnet [10] with a high degree of spin polarization near the Fermi level and its inverse spinel structure provides different crystal planes with different magnetization directions; these facts make magnetite a potential model system for SPSTM.

In this study, the (001) surface of magnetite artificial single crystal has been studied using low-energy electron diffraction (LEED), Auger electron spectroscopy (AES) and (STM). This thesis is organized as follows. In chapter 2 a description of the experimental setup is given; AES, LEED and STM techniques are described and one section is dedicated to the preparation of STM tips. In chapter 3 we provide an overview of the iron-oxygen system and a description of $\text{Fe}_{(1-x)}\text{O}$, Fe_3O_4 , $\gamma\text{-Fe}_3\text{O}_4$ and $\alpha\text{-Fe}_3\text{O}_4$ is given. In chapter 4 the electrostatic and the electron counting models are presented; these two models are useful in the interpretation of the reconstruction of the $\text{Fe}_3\text{O}_4(001)$ surface. A literature review of the $\text{Fe}_3\text{O}_4(001)$ surface reconstructions observed in the last decade is given. The preparation and characterization of the surface are described in chapter 5; two preparation procedures, giving rise to different surface reconstructions are described in detail. In chapter 6 we analyze the influence of contaminant segregation and a $p(1 \times 4)$ reconstruction is discussed. In chapter 7 we report the observation of a $(\sqrt{2} \times \sqrt{2})R45^\circ$ reconstruction of an atomically resolved surface. The anomalous periodicity of Fe atoms observed using antiferromagnetic tips has been explained in terms of a "Wigner localization" on the surface, leading to a static arrangement of pairs of Fe^{2+} and pairs of Fe^{3+} ions.

Chapter 2

Experimental details

2.1 The experimental setup

The UHV system consists of three chambers: the room-temperature STM (RTSTM) chamber, the low-temperature STM (LTSTM) chamber and the preparation chamber. A full description of the construction and operation of the RTSTM is given by Quinn [11], the LTSTM chamber is detailed by [12] and the preparation chamber by [13]. The layout of the system is shown in figure 2.1.

Each chamber can be valved off from the rest of the system via a series of UHV gate valves (VAT [14]) and brought to atmospheric pressure for maintenance without breaking vacuum in the other chambers. Samples and tips are introduced in the system via a fast-entry loadlock connected to the preparation chamber by a gate valve. The loadlock is maintained in the low 10^{-10} mbar range by a $20 \text{ l}\cdot\text{s}^{-1}$ differential ion-pump (Perkin-Elmer [15]). Tip and sample transfer through out the chambers is achieved by a series of wobblesticks and magnetically-coupled linear drives (Vacuum Generators Ltd. [16]). The pressure in each chamber is monitored using nude Bayard-

2. Experimental details

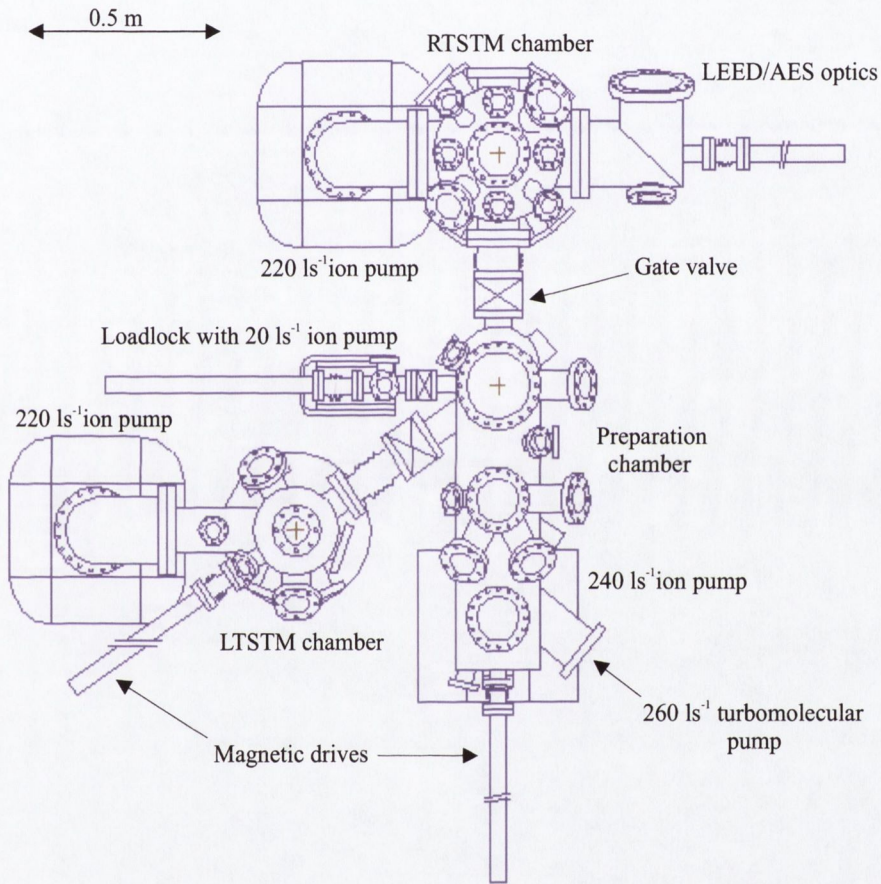


Figure 2.1: Top view schematic of the UHV system.

Alpert type ionisation gauges (Perkin-Elmer). The entire system is mounted onto a stainless steel box-section frame which can be floated on pneumatic dampers to isolate the system from low-frequency vibration during STM measurements. The box-section is filled with gravel to minimise hollow pipe vibrations.

The RTSTM chamber

The RTSTM chamber is a standard outer diameter (O.D.) 457 mm commercial chamber (Perkin-Elmer) with two modified ports, for a total of twenty-one ports. The RTSTM is mounted inside this chamber via the O.D. 254 mm base flange. A customised mitred elbow (VG) to the side of the main chamber provides the annexe that houses the four-grid LEED/Auger optics. This chamber also contains a tip and sample storage carousel. The chamber is pumped by a $220 \text{ l}\cdot\text{s}^{-1}$ differential ion-pump with TSP and cryoshroud, which is connected to a mitred elbow on the opposite side of the chamber. This eliminates stray magnetic fields from the vicinity where LEED and (magnetic) STM experiments are carried out. The chamber is pumped down from atmosphere by a $60 \text{ l}\cdot\text{s}^{-1}$ turbo pump which is connected via a right-angle UHV valve (VG) and a 1 metre long formed bellows. The chamber is baked inside a custom-designed oven [11] which encloses the chamber, LEED annexe and ion-pump. There are two 840 W radiative heaters mounted on the base of the oven, while the ion-pump houses eight 200 W heating strips. The temperature inside this oven is maintained at $120\text{--}130 \text{ }^\circ\text{C}$ (this temperature is below the maximum withstandable temperature of the STM $I\text{--}V$ pre-amplifier) for 2–3 days to achieve a base pressure in the $\text{mid-}10^{-11}$ mbar.

The preparation chamber

The preparation chamber was designed by Dr. S. Murphy [13] and manufactured by Caburn-MDC Ltd. [17]. It is an O.D. 209 mm \times 3.0 mm stainless steel (304 grade) cylinder approximately 0.8 m long, with one hemispherical end and one plated. There are a total of twenty-seven access ports. This chamber contains the following facilities for *in-situ* tip and sample preparation:

- a resistive heater to anneal samples to a temperature up to 1100 K.
- an e -beam heater to anneal samples to a temperature up to 2600 K
- a liquid nitrogen cooled evaporator
- a quartz crystal deposition monitor (Inficon [18])
- an ion gun (VG Microtech [19])
- precision leak valves for introduction of high purity oxygen, argon and hydrogen gases.

The preparation chamber also contains an AES setup (Perkin-Elmer) for chemical analysis of the samples. The chamber is usually baked for 2 days at 170-180 °C by three heating tapes with a total radiative power of 2175 W. The temperature is measured by two thermocouples, the first feeds the Eurotherm 91e controller which controls the bakeout [11], while the second feeds an Omega CN375 controller which acts as a fail-safe against over-heating. The chamber is wrapped in aluminium foil and a heavy bake-out blanket to provide thermal insulation. A number of pumps are used to achieve UHV conditions in the chamber. A TMU 260 $\text{l}\cdot\text{s}^{-1}$ turbomolecular pump (Pfeiffer Vacuum [20]), backed up by a 0.7 $\text{l}\cdot\text{s}^{-1}$ two-stage rotary vane pump is used to pump the chamber down from atmospheric pressure. This pump is also used to handle heavy gas loads during ion sputtering and

oxidation procedures. A double-ended $240 \text{ l}\cdot\text{s}^{-1}$ differential ion-pump (Physical Electronics [15]) is used to maintain UHV conditions. A liquid nitrogen cryoshroud is inserted in the base flange of the ion-pump which houses a titanium sublimation pump (TSP). The maximum pumping speed obtainable when titanium is deposited on a surface at 300 K is $3\text{--}9 \text{ l}\cdot\text{s}^{-1}\cdot\text{cm}^{-2}$ for hydrogen and oxygen, while it is increased by a factor of $2\text{--}5$ upon cooling to 70 K [21]. A non-evaporable getter pump (NEG) from SAES Getters [22] is positioned mid-way along the chamber.

A base pressure in the mid- 10^{-11} mbar is usually obtained in this chamber after bakeout.

The LTSTM chamber

The LTSTM chamber was also designed by Dr. S. Murphy [13] and built by Caburn-MDC. It has dimensions O.D. $209 \text{ mm} \times 3.0 \text{ mm} \times 270 \text{ mm}$ (height) with one dished end. The chamber is connected to the UHV insert of a 60 l liquid He cryostat, for cryogenic experiments. A bakeout system has not yet been constructed for this system, the chamber is pumped by a $220 \text{ l}\cdot\text{s}^{-1}$ differential ion-pump with TSP and cryoshroud and a NEG pump. A base pressure of 1×10^{-9} mbar is usually obtained.

The resistive heater

The resistive heater (see figure 2.2) was designed by C. Kempf and assembled by J. Naumann. A 0.2 mm diameter W wire is wrapped around an alumina crucible with spiral grooves machined along its circumference. A Ta insert is placed inside the crucible. Both the crucible and the Ta insert have a concentric aperture drilled along their axes. The crucible fits inside a stainless steel can which is connected to a linear translation drive; this allows to position

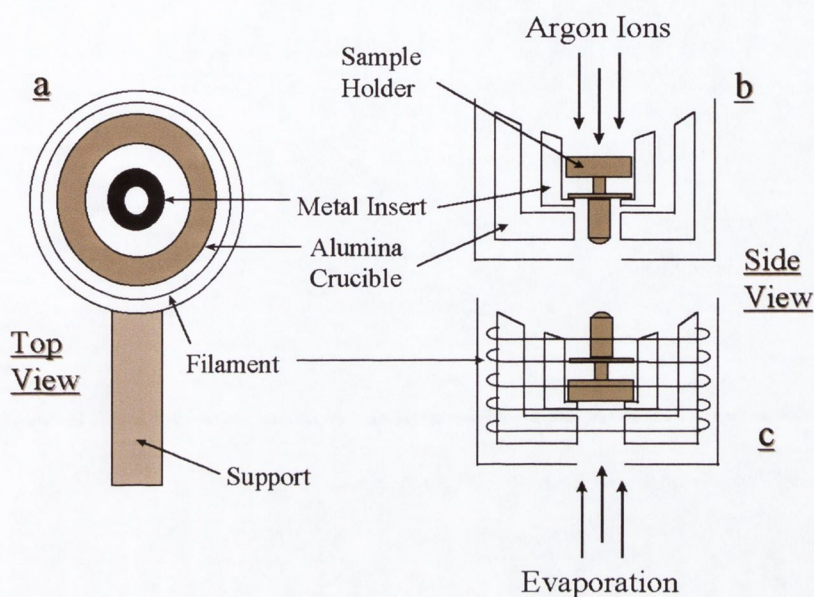


Figure 2.2: Schematic illustration of the resistive heater. The sample can sit face-down in the heater so that Fe can be deposited on it through the aperture in the base. Alternatively, the sample (or tip) is inserted face-up for ion-etching. Reproduced from [24].

the sample above the e -beam evaporator or below the ion gun. The sample can fit in the Ta insert either face-down or face-up. A quartz crystal sensor is positioned some 10 cm behind the stainless steel can; two pipes carry the water to cool down the sensor and one BNC feedthrough carries the signal from the sensor to the quartz crystal monitor. The temperature during annealing is monitored by a K-type (Omega Inc. [23]) thermocouple which is spot-welded to the Ta insert. The heater was calibrated for temperature (K) *versus* filament power (W) with the thermocouple attached to the face of a sample-holder mounted face-down in the heater. The calibration curve is given in appendix A.

The electron beam heater

The e -beam heater was designed and assembled by Dr. J. Osing [12]. It is used to clean refractory metal samples such as W and Mo, since conventional resistance heaters are not suitable to heat samples to very high temperatures, in the range $2200 \text{ K} \leq T \leq 2600 \text{ K}$, in a short period of time. Figure 2.3 shows a schematic of the e -beam heater fitted in the UHV chamber. The sample holder is mounted into a Ta stage which is held at a potential of $+1 \text{ kV}$. A current ($2.5 \text{ A} \leq I \leq 4.5 \text{ A}$) is passed through a grounded thoriated tungsten filament ($\phi = 0.15 \text{ mm}$, 0.6% Th) which generates thermionic emission of electrons. These electrons are accelerated towards the cap of the sample holder, where upon collision, their kinetic energy is transferred to the sample as heat. Because the filament is situated to one side of the sample there will be a temperature gradient across the sample, however, this set-up produces a contamination free surface. Surface temperatures are measured from outside the chamber using an infra-red pyrometer (Altimex UX-20/600 [25]).

The ion gun

The preparation chamber is fitted with a cold-cathode type ion gun (VG Microtech), which is used for cleaning sample surfaces and for Ar^+ ion etching of STM tips. During operation the chamber is pumped using the $260 \text{ l}\cdot\text{s}^{-1}$ turbo pump. The argon gas is introduced by leak-valve directly into the gas-cell of the ion-gun, the base pressure in the chamber rises to $5 \times 10^{-6} \leq P_{\text{Ar}} \leq 1 \times 10^{-5} \text{ mbar}$. The gas-cell contains a cylindrical anode, while the casing of the cell acts as the cathode. Applying a potential difference of a few kilovolts between these electrodes strikes an electric discharge in the cell, which generates the positive ions. These ions are confined in a helical path in the cell by an externally mounted cylindrical permanent mag-

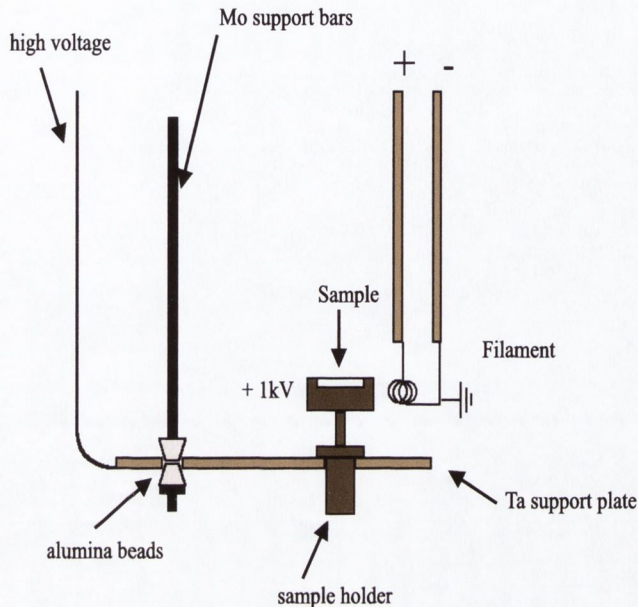


Figure 2.3: A schematic illustration of the e -beam heater used to clean refractory metal samples. Reproduced from [12].

net. The ion beam is accelerated with a beam energy between 500 eV and 5 keV, through the gas-cell aperture and focussed by a series of concentric electrostatic lenses. The spot size could be varied between 19 mm and 25 mm with a sample/gun working distance of 250 mm.

The target diameter is taken as 11 mm, which is the diameter of the circular Ta insert in the resistive heater, into which the sample/tip is mounted for ion-etching. This insert is isolated from ground by the surrounding ceramic crucible. The thermocouple spot-welded to this insert allows the target current to be measured. This is typically of the order of $3.0 \mu\text{A} \leq I \leq 20.0 \mu\text{A}$ for a 1-2 keV beam energy and a chamber pressure of 1×10^{-5} mbar. The target current is measured using the ion-gun control unit, which biases the sample with +15 V to suppress low energy secondary electrons generated by the impacting ions.

An estimate of the amount of material removed from the surface by sputtering can be calculated knowing the incident ion flux (calculated from the target current) and the sputter yield Y (the number of target atoms ejected per incident ion). The sputter rate ν is obtained from the relation [26]:

$$\nu = \frac{JYM}{\rho e N_A n} \quad [\text{m}\cdot\text{s}^{-1}] \quad (2.1)$$

where J is the ion current density ($\text{A}\cdot\text{m}^{-2}$), Y the sputter yield (atoms/incident ion), M the molar mass of the target matrix ($\text{kg}\cdot\text{mol}^{-1}$), ρ the density ($\text{kg}\cdot\text{m}^{-3}$), e the electron charge ($\text{A}\cdot\text{s}$), N_A is Avogadro's constant (mol^{-1}) and n the number of components yielded per matrix molecule ($n = 1$ for an elemental target). For a circular target, this can be re-written as:

$$\nu = \frac{4IYM}{e\pi D^2 \rho N_A} \quad [\text{m}\cdot\text{s}^{-1}] \quad (2.2)$$

where I is the target current (A) and D is the sample diameter (m).

The electron beam evaporator

Ultra thin Fe films can be deposited using an electron beam evaporator (see figure 2.4) designed and assembled by C. Kempf. The principle of operation is the same as that for the e -beam heater. Electrons originating from a hot (thoriated tungsten) filament are accelerated towards a 3N purity $\phi = 1.6$ mm Fe rod which is at a potential of + 1.9 kV with respect to ground. A heat-shield is formed around the Fe rod and filament by a tube of Ta foil which sits into grooves cut in the Mo end-caps of the cell. Alumina beads isolate the filament from these end-caps. Apertures in each Mo cap allow the Fe rod into the cell at one end and the evaporated Fe out through the other. The entire cell fits inside a double-walled liquid N_2 cooled cryoshroud. During operation, cooling this cryoshroud minimises outgassing from the en-

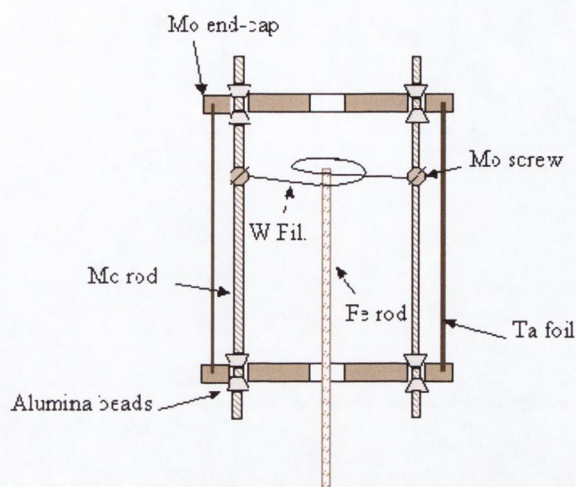


Figure 2.4: A schematic illustration showing a cross-sectional view of the e -beam evaporator used to deposit ultrathin Fe films. Reproduced from [11].

virons of the evaporator. A new Fe rod is outgassed for several hours before it is suitable for use, it is also outgassed for a further 3-4 hours before each subsequent deposition. Typical values for the filament and emission currents during deposition are 2.5 A and 4 mA respectively. The chamber pressure usually rises to no more than the mid- 10^{-10} mbar.

The sample sits upside-down inside the resistive heater (described above), which has an aperture machined in its base. This set-up allows the sample surface to be heated for depositions at elevated temperatures. The resistive heater is also equipped with a water-cooled quartz crystal deposition monitor (Inficon) which is calibrated to monitor the deposition of b.c.c. Fe. The entire stage is mounted on a linear drive so that alternately, the sample or quartz monitor can be moved into position over the evaporator aperture. During a deposition the quartz crystal is first positioned over the evaporator aperture. The filament current is slowly increased until a stable deposition rate is

achieved, this is usually about $0.5 \text{ ML}\cdot\text{min}^{-1}$ ($0.015 \text{ \AA}\cdot\text{s}^{-1}$). Then the sample, which is cleaned 20-45 minutes prior to deposition, is rapidly moved into the deposition beam – this takes roughly 10 seconds. As a result the amount of material deposited upon the surface is not exactly controlled, however, the deposition rate is typically so low that only a very small fraction of the total coverage can be deposited in this time. Once the required deposition time has elapsed the filament current and accelerating voltage are quickly ramped down.

2.1.1 The STM

Comprehensive reviews of the theory and operating principles of scanning tunneling microscopy (STM) and spectroscopy (STS) are given in dedicated texts by Chen and Wiesendanger [27,28]. The fundamental theory of STM is modelled on the quantum-mechanical description of an electron with energy E travelling in a 1D potential $U(z)$ of the form shown in figure 2.5(a). This electron is described by a wavefunction $\psi(z)$, which satisfies the Schrödinger equation:

$$-\frac{\hbar^2}{2m} \frac{d^2}{dz^2} \psi(z) + U(z)\psi(z) = E\psi(z) \quad (2.3)$$

where m is the electron mass and $\hbar = h/2\pi$ (where h is Planck's constant). In the classically allowed region where $E > U(z)$, this equation has solutions of the form:

$$\psi(z) = \psi(0)e^{\pm ikz}, \quad k = \frac{\sqrt{2m(E - U)}}{\hbar} \quad (2.4)$$

where the electron can move in either the positive or negative sense of direction. In the classically forbidden *barrier* region where $E < U(z)$, the Schrödinger equation has the solution:

$$\psi(z) = \psi(0)e^{-\kappa z}, \quad \kappa = \frac{\sqrt{2m(U - E)}}{\hbar} \quad (2.5)$$

The κ term describes the decay of the electron wavefunction within the barrier region. For a finite potential $U(z)$, there is a non-zero probability P of finding the electron at a position z inside the barrier region, which is given by:

$$P \propto |\psi(0)|^2 e^{-2\kappa z} \quad (2.6)$$

Consequently, if the width of the tunnel barrier is sufficiently narrow, there is a finite probability that the electron can tunnel through the barrier region.

In the tip-vacuum-sample configuration of an STM junction (figure 2.5(b)), the height of the tunnel barrier is determined by the *work function* ϕ of the tip and sample (assumed to be identical for convenience), which is the minimum energy required to remove an electron from the metal to vacuum. An electron at the tip or sample surface, with Fermi energy $E_F = -\phi$, will have the greatest opportunity to tunnel through the barrier, since by definition the *Fermi level* denotes the upper limit of electron occupancy in the metal. In the absence of an externally applied bias, the electron can tunnel through the barrier in either direction so that there is no net tunnel current. By applying an external voltage V , electrons in the sample within the energy range $E_F - eV \leq E \leq E_F$ have an opportunity to tunnel through the barrier. If $eV \ll \phi$, then only electron states very near to the Fermi level are probed. The probability for an electron in the n th of these states to tunnel through a barrier of width W is given by:

$$P \propto |\psi_n(0)|^2 e^{-2\kappa W}, \quad \kappa = \frac{\sqrt{2m\phi}}{\hbar} \quad (2.7)$$

Taking all the possible states in the energy range $E_F - eV \leq E \leq E_F$ into account, the tunnel current is:

$$I_t \propto \sum_{E=E_F-eV}^{E_F} |\psi(0)|^2 e^{-2\kappa W} \quad (2.8)$$

This equation may be re-written in terms of the *local density of states* (LDOS) at the Fermi level of the sample surface $\rho_s(0, E_F)$:

$$I_t \propto V \rho_s(0, E_F) e^{-2\kappa W} \quad (2.9)$$

It is clear from this equation that: (1) the tunnel current is directly proportional to the bias applied across the junction, (2) it decays exponentially as the distance between the tip apex and the sample surface is increased and (3) the local density of states of the surface is sampled.

The significance of the probe-tip LDOS contribution is realised through a time-dependent perturbation model of metal-insulator-metal tunneling proposed by Bardeen [29]. Here, a *Transfer Hamiltonian* H_T is used to describe the transfer of a tunneling electron from a sample state ψ to a tip state χ . The tunnel current can be taken as a convolution of the sample LDOS ρ_s and the tip LDOS ρ_t .

$$I_t = \frac{4\pi e}{\hbar} \int_0^{eV} \rho_s(E_F - eV + E) \rho_t(E_F - E) |M|^2 dE \quad (2.10)$$

I_t also includes a tunneling matrix element M , describing the amplitude of electron transfer across the tunnel barrier (through the overlap of the ψ and χ states). The integral describing M is evaluated over any surface lying within the barrier region.

$$M = \frac{\hbar}{2m} \int (\chi^* \frac{\partial \psi}{\partial z} - \psi \frac{\partial \chi^*}{\partial z}) dS \quad (2.11)$$

All STM images described in this thesis were obtained by scanning the tip across the surface in constant current mode. In this configuration the tip-sample separation is maintained at a constant value by means of a feedback-loop which controls a piezoelectric tube scanner holding the tip. The sample is biased and the tip is earthed. The room-temperature microscope (RTSTM)

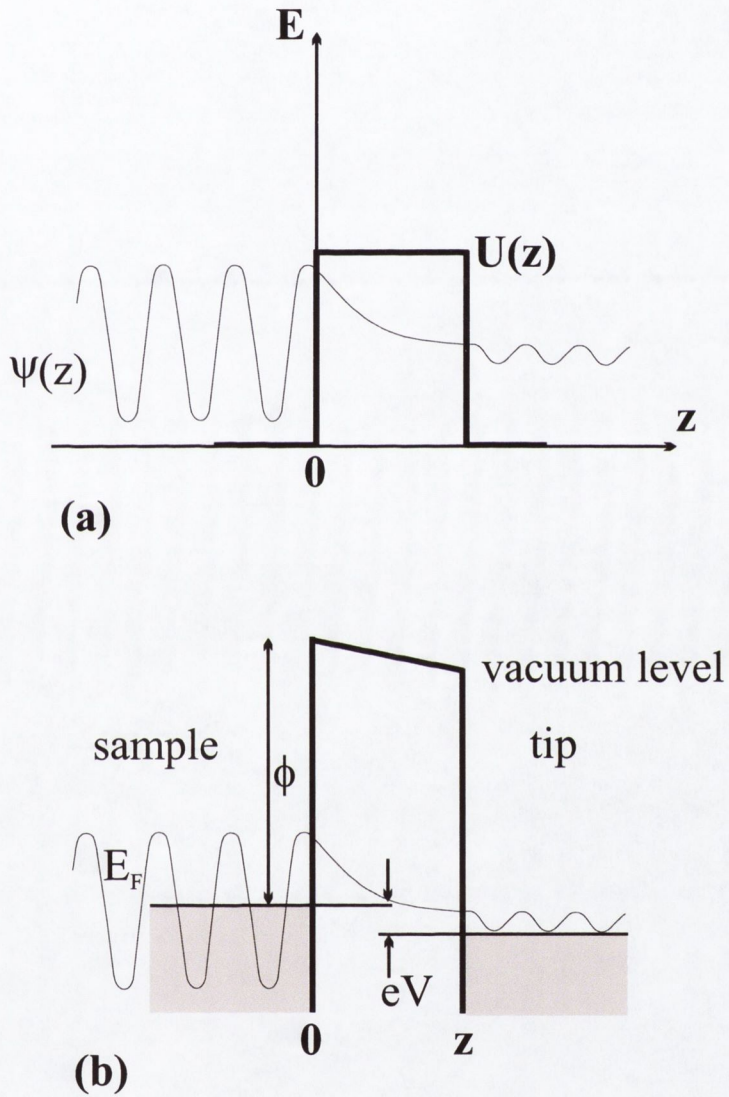


Figure 2.5: Schematic representations of (a) an electron described by the wavefunction $\psi(z)$ travelling in a one-dimensional potential $U(z)$ and (b) a STM junction under an applied bias V .

used in this study was built by Dr. A. Quinn [11]. The STM head is constructed from machinable ceramic (Macor) and comprises a piezo tube scanner and a fine approach piezo-walker based upon the system developed by Dr. S.H. Pan at the University of Basel, Switzerland [30]. The sample is mounted on top of a polished quasi-cylindrical sapphire rod which is clamped between a set of six piezo stacks. These piezo stacks are arranged pairwise in a triangular fashion about the sapphire rod with one pair of stacks spring-loaded against it. A signal composed of quarter sections of a period of a sine wave is applied to the piezo stacks. To make one step the piezos first deform quickly in one direction and slip under the rod leaving its position virtually unchanged. Then they deform slowly back simultaneously and drag the rod with them. The fine approach piezo-walker can operate both in an inertial and a frictional modes. A full description of this mechanism is discussed in [31, 32]. This fine approach system is controlled using a home-built control unit [11].

The tube scanner is sectioned into four outer Ag electrodes which carry the $Z-X$, $Z+X$, $Z-Y$ and $Z+Y$ voltages, while the inner electrode is grounded. The scanner has a dynamic range of $\pm 13000 \text{ \AA}$ in the z -direction and $\pm 20600 \text{ \AA}$ in the x - and y - directions. These ranges were calibrated on Cu(100) monoatomic steps and highly oriented pyrolytic graphite (HOPG) atomic resolution images respectively. The STM head is isolated from vibrations by a two-stage spring system [11] which works in conjunction with the pneumatic dampers on the system frame.

The RTSTM chamber is also fitted with an electromagnet, designed and assembled by J. Naumann, to carry out magnetic STM experiments. This consists of two Permanorm 5000 poles with Kapton-insulated copper wire windings. Three thermocouples are fitted to monitor the heat output generated by the magnet. This magnet can be positioned so that the sample in the

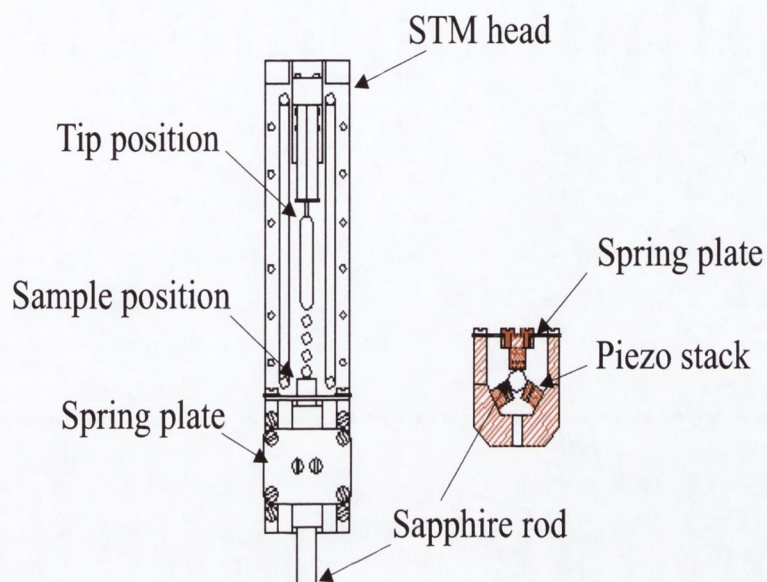


Figure 2.6: Schematic representation of a STM head similar to the RTSTM used. A front view and cross-section of the fine approach walker are shown.

STM lies between the poles. An in-plane magnetic field of 90 mT is possible without significant overheating of the sample.

Two STM controllers were used for these experiments: a TOPS II system by WA Technology [33] and a SCALA system by Omicron GmbH [34]. The accompanying softwares provide some functions for data analysis, however data was also analysed using commercial software from NTMDT, Russia [35] and from Nanotec Electronica S.L. [36].

2.1.2 Four-grid LEED/AES optics

The RVLO 900 four-grid reverse view optics were manufactured by VG Microtech. Primarily used for low-energy electron diffraction (LEED), these optics can also be operated as a retarding-field analyser for Auger electron spectroscopy (AES). The optics are mounted on a O.D. 200 mm CF cus-

tom elbow which is tilted at an angle of 30° to the horizontal. The optics are surrounded by a mu-metal cylinder to provide shielding from stray magnetic fields. The sample sits in the transfer fork of a magnetic drive, which is grounded by a stainless steel braid to an oxygen free high conductivity (OFHC) copper block at the bottom of the LEED annexe. The sample is rotated in this drive so that its surface faces the electron gun. Scattered electrons are collected by the grids and screen located behind the gun.

LEED operation

A schematic illustration of the four-grid LEED is shown in figure 2.7. The grid nearest the sample M1 is earthed so that electrons scattered by the sample, initially travel in field-free space. A negative potential is applied to the two centre grids M2a and M2b to suppress inelastically scattered electrons, while elastically scattered electrons are accelerated towards the phosphorescent screen by its +5 keV potential. The fourth mesh M3 is also grounded to reduce the field penetration of the suppressing grids by the screen. Although the RVLO 900 four-grid reverse view optics can be operated as a retarding-field analyzer for AES, the performance of this set-up is very poor. All the AES measurements presented in this thesis have been done using a Cylindrical-Mirror Analyzer described in the next section.

LEED patterns were taken at energies between 40 eV and 200 eV, using an emission current of 0.5 mA, the target current could not be measured. LEED patterns were recorded by photographing the screen. The spot-separation in these photographs could be used to calculate the surface net parameters of the surfaces analysed [11].

For surface diffraction in a $2D$ system, the assumption of infinite periodicity is a fair approximation in two dimensions, but not in the third dimension

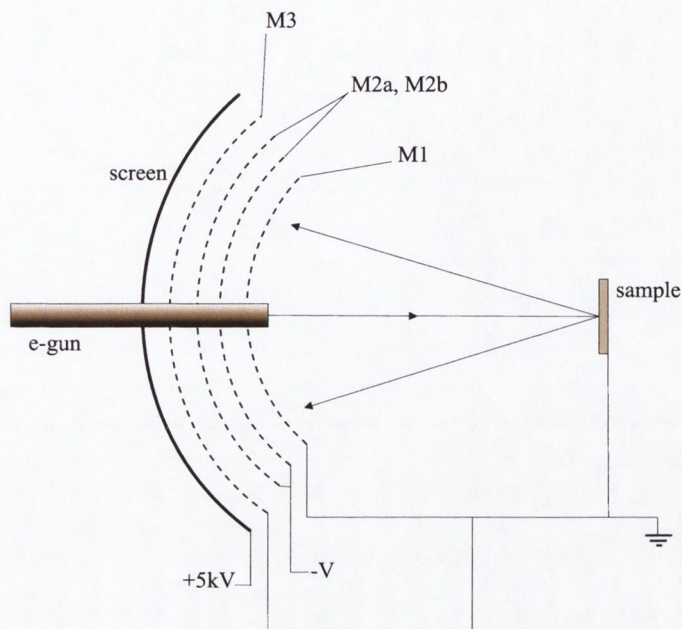


Figure 2.7: Schematic of four-grid optics operating in LEED mode (*c.f.* reference [37]).

which is truncated by the presence of the surface itself. The crystal structure probed by LEED may therefore be considered to be a slab, infinitely periodic in two dimensions, but comprising only a few layers in the third dimension. The real space two-dimensional lattice is specified by two lattice vectors \mathbf{a}_1 and \mathbf{a}_2 . These define the boundaries of a parallelogram which form the boundaries of the unit cell.

A plane wave incident on an atom or atoms within a unit cell will be scattered in all directions, but interference between waves scattered from neighbouring unit cells will restrict the net flux to those directions in which the scattered waves from all unit cells are in phase. This requires that the scattered waves from neighbouring cells differ only by an integral number of wavelengths λ .

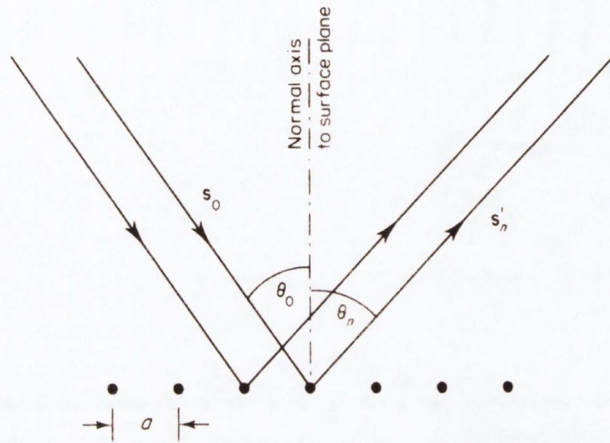


Figure 2.8: Laue diffraction from a one-dimensional array of scatterers.

In the simple case of a one-dimensional lattice (see Fig. 2.8), the in-phase condition is met for all integers n which satisfy the condition

$$a(\sin\theta_n - \sin\theta_0) = n\lambda \quad (2.12)$$

where a is the distance between scatterers, λ is the wavelength of the incident wave and θ_0 is the angle of the plane wave with respect to the lattice. This is known as the *Laue condition*. If the incident and emergent beams are described by unit vectors \mathbf{s}_0 and \mathbf{s}'_n then this can be written in vector form as

$$\mathbf{a} \cdot (\mathbf{s}'_n - \mathbf{s}_0) = n\lambda \quad (2.13)$$

or

$$\mathbf{a} \cdot \Delta\mathbf{s}_n = n\lambda \quad (2.14)$$

where

$$\Delta\mathbf{s}_n = (\mathbf{s}'_n - \mathbf{s}_0) \quad (2.15)$$

The diffracted beams are determined by $\Delta\mathbf{s}_n$ and, in the one-dimensional case, they are given by integral multiples

of the basic unit $(\lambda/|\mathbf{a}|)$. This involves the *reciprocal* of the real space lattice vector \mathbf{a} . We can define a *reciprocal lattice vector* $a^* = (1/a)$.

A simple construction – known as the Ewald sphere – permits the diffraction beam angles to be derived from the reciprocal lattice. Only elastically scattered waves contribute to the diffraction process, so that their wavelengths are the same on incidence and emergence. Propagating waves in reciprocal space can be represented by lines of length $(1/\lambda)$, and we shall assume that the incident wave will have a direction at an angle θ with respect to the crystal planes. We shall give this vector the symbol \mathbf{k}_0 . The construction is illustrated in Fig. 2.9 for the one-dimensional case, where the reciprocal lattice planes have been illustrated as lines. The wave vector \mathbf{k}_0 is positioned so that one end touches a lattice line, and the other end provides the centre for a circle of radius $(1/\lambda)$ or $|\mathbf{k}_0|$. Wave vectors which touch this circle have the same energy as the incident beam, and whenever this circle cuts a reciprocal lattice line the difference between the components of the resulting \mathbf{k} and the incident \mathbf{k}_0 in a direction parallel to \mathbf{a} must equal an integral number of reciprocal lattice vectors $n\mathbf{a}^*$. This satisfies the condition given in equation 2.13 for possible diffraction beams. In other words, the Ewald sphere defines the locus of beam vectors which have the same energy as the incident beam, and the intersection of this sphere with the reciprocal lattice rods defines the conditions under which both the diffraction condition and the conservation of beam energy are satisfied simultaneously. As the incident energy is increased, so the sphere radius will also increase. As a consequence, the number of diffraction beams increases and the angle between each diffraction beam decreases: the diffraction beam will appear to condense towards the specular beam.

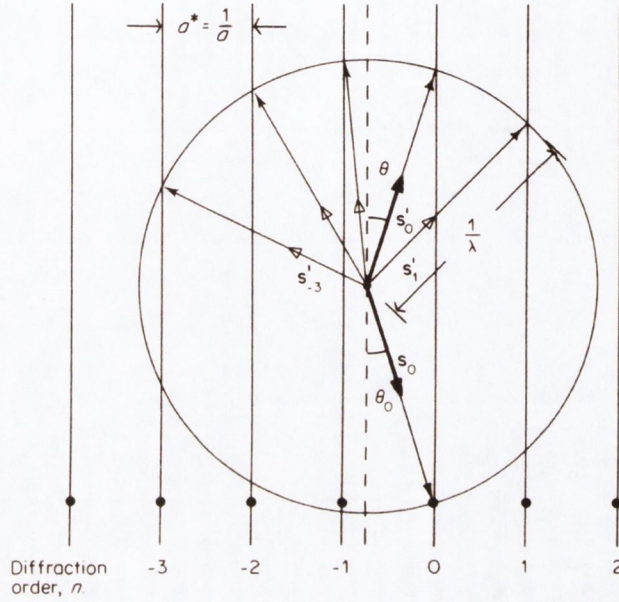


Figure 2.9: Laue diffraction from a one-dimensional array of scatterers.

In two dimensions, the real space lattice is described by two lattice vectors \mathbf{a}_1 and \mathbf{a}_2 , and a corresponding reciprocal lattice can be constructed from basis vectors \mathbf{a}_1^* and \mathbf{a}_2^* , defined by the following relations:

$$\mathbf{a}_1 \cdot \mathbf{a}_1^* = \mathbf{a}_2 \cdot \mathbf{a}_2^* = 2\pi \quad (2.16)$$

and

$$\mathbf{a}_1 \cdot \mathbf{a}_2^* = \mathbf{a}_1^* \cdot \mathbf{a}_2 = 0 \quad (2.17)$$

The second relation requires that \mathbf{a}_2^* be perpendicular to \mathbf{a}_1 and \mathbf{a}_1^* be perpendicular to \mathbf{a}_2 . Any vector relating two reciprocal lattice points must take the form

$$|\mathbf{g}_{hk}| = |h\mathbf{a}_1^* + k\mathbf{a}_2^*| = |\mathbf{k}| \sin\alpha = \frac{\sqrt{2m_e E_{eV}}}{\hbar} \sin\alpha \quad (2.18)$$

where h and k are integers, E_{eV} is the beam energy, m_e is the electron mass and α is the diffraction angle.

Diffraction from the two-dimensional lattice must satisfy the two Laue conditions

$$\mathbf{a}_1 \cdot \Delta \mathbf{s} = h\lambda \quad (2.19)$$

and

$$\mathbf{a}_2 \cdot \Delta \mathbf{s} = k\lambda \quad (2.20)$$

and these can be solved whenever

$$\Delta \mathbf{s} = \lambda(h\mathbf{a}_1^* + k\mathbf{a}_2^*) = \lambda\mathbf{g}_{hk} \quad (2.21)$$

This shows the direct correspondence between the observed diffraction pattern and the reciprocal lattice of the surface. The reciprocal lattice vector \mathbf{g}_{hl} lies in a direction that is orthogonal to the plane of the real space lattice that is denoted by the Miller indices h and l . The Miller indices of the diffracting planes are used to index the diffraction spots of the LEED pattern. The angle α may be determined from the spot-separation d_r between indexed spots in the LEED pattern by using the geometry of the LEED screen, shown in figure 2.10. The actual spot-separation can be calculated from the distance d_{photo} measured in a photograph of the pattern using:

$$d_r = \frac{d_{photo}D_r}{D_{photo}} \quad (2.22)$$

where D_r is the actual screen diameter and D_{photo} is the screen diameter measured in the photograph.

LEED on $\text{Fe}_3\text{O}_4(001)$

The structure of magnetite is that of an inverse spinel. It has a face-centered cubic unit cell based on O^{2-} ions. The Fe cations occupy $\frac{1}{8}$ of the 64 available tetrahedral A sites and $\frac{1}{2}$ of the 32 available octahedral B sites. There are 8 formula units (Fe_3O_4) per conventional unit cell, for a total of 32 O^{2-} and

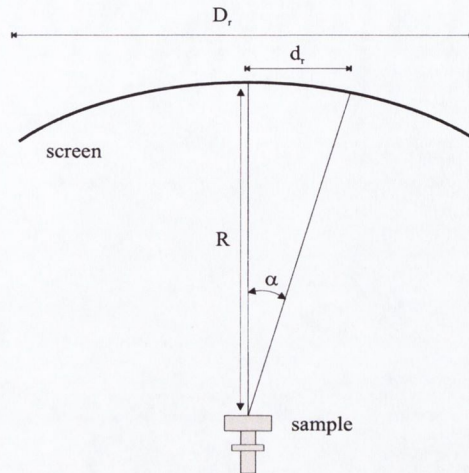


Figure 2.10: Schematic of the LEED screen geometry. The sample is placed at the focal point of the screen. The angle α can be determined from $\tan \alpha = d_r/R$. The distance d_r is the separation between the hk spot and the specular spot.

24 Fe ions. The conventional unit cell length is $a \cong 8.4 \text{ \AA}$. The top view of a (001) bulk-terminated face-centered cubic (f.c.c.) crystal surface is shown in fig. 2.11.

Figure 2.12 shows the $p(1 \times 1)$ and the $(\sqrt{2} \times \sqrt{2})R45^\circ$ surface structures in real and reciprocal space. Filled circles correspond to the (1×1) lattice, while open circles represent the superlattice in the real space and fractional-order beams in the reciprocal space.

Figure 2.13 shows a LEED pattern observed with a primary electron energy of 93 eV. A $(\sqrt{2} \times \sqrt{2})R45^\circ$ mesh is visible, and the $(\sqrt{2} \times \sqrt{2})R45^\circ$ superlattice is indicated by a red solid square. The superlattice edge was measured to be $a = 8.3 \pm 1.7 \text{ \AA}$, in very good agreement with the value expected for the conventional unit cell edge. The $p(1 \times 1)$ unit cell is marked by a yellow dashed square. The interpretation of the pattern is facilitated by a comparison with fig. 2.12 (d).

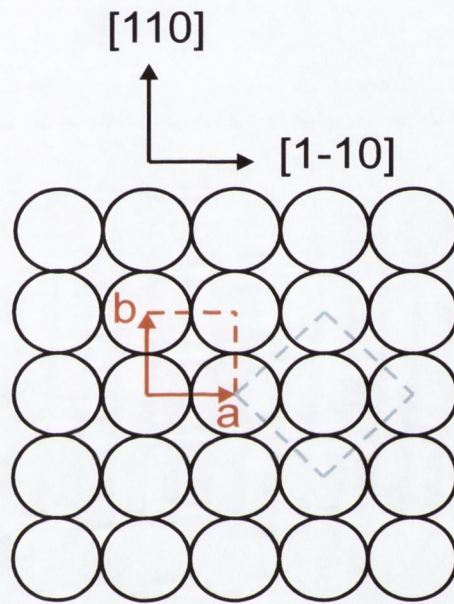


Figure 2.11: Top view of the (001) surface of magnetite. (for simplicity only the O^{2-} ions, forming an f.c.c. lattice, are shown). The conventional unit cell is marked by a dashed blue square. The primitive unit cell is indicated by a red square, together with the primitive lattice vectors. The conventional unit cell edge is $a \cong 8.4 \text{ \AA}$, and the primitive unit cell edge is $a \cong 5.9 \text{ \AA}$.

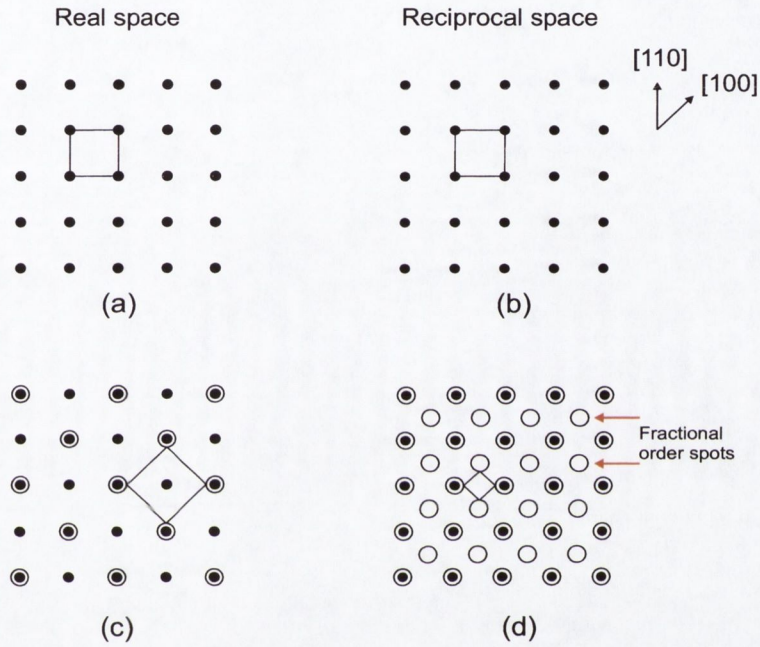


Figure 2.12: The $p(1\times 1)$ surface structure in real space (a) and in reciprocal space (b). The primitive unit cell is marked by a solid square; its edge $a \cong 5.9 \text{ \AA}$ is oriented along the $\langle 110 \rangle$ directions.

The $(\sqrt{2} \times \sqrt{2})R45^\circ$ surface structure in real space (c) and in reciprocal space (d). The $(\sqrt{2} \times \sqrt{2})R45^\circ$ superlattice is marked by a solid square; its edge $a \cong 8.4 \text{ \AA}$ is oriented along the $\langle 100 \rangle$ directions and is equal to the edge of the conventional bulk unit cell of magnetite.

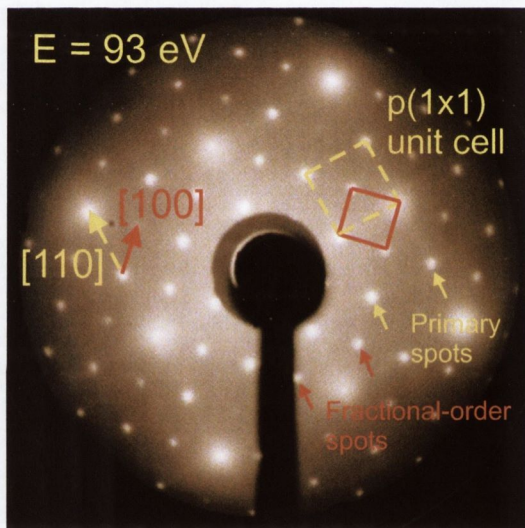


Figure 2.13: LEED pattern of a clean $\text{Fe}_3\text{O}_4(001)$ surface observed with a primary electron energy of 93 eV. A $(\sqrt{2} \times \sqrt{2})R45^\circ$ mesh is visible. The primitive $p(1 \times 1)$ unit cell and the $(\sqrt{2} \times \sqrt{2})R45^\circ$ superlattice are indicated by a yellow dashed square and a red solid square, respectively.

2.1.3 Cylindrical-Mirror Analyzer for AES

A model 10–155A Physical Electronics cylindrical mirror analyser was used for AES analysis of $\text{Fe}_3\text{O}_4(001)$ samples. The cylindrical mirror analyser (CMA) operates as an electrostatic deflection analyser. It consists of concentric inner (radius r_1) and outer (radius r_2) cylinders, with a coaxially mounted electron gun (figure 2.14). A primary electron beam is produced by thermionic emission from a hot filament (F1 and F2) and acceleration through a potential V_2 . The beam current can be varied by changing the extraction voltage V_1 to vary the level of emission. The primary beam could be focussed on the sample to produce a beam diameter of $100\ \mu\text{m}$.

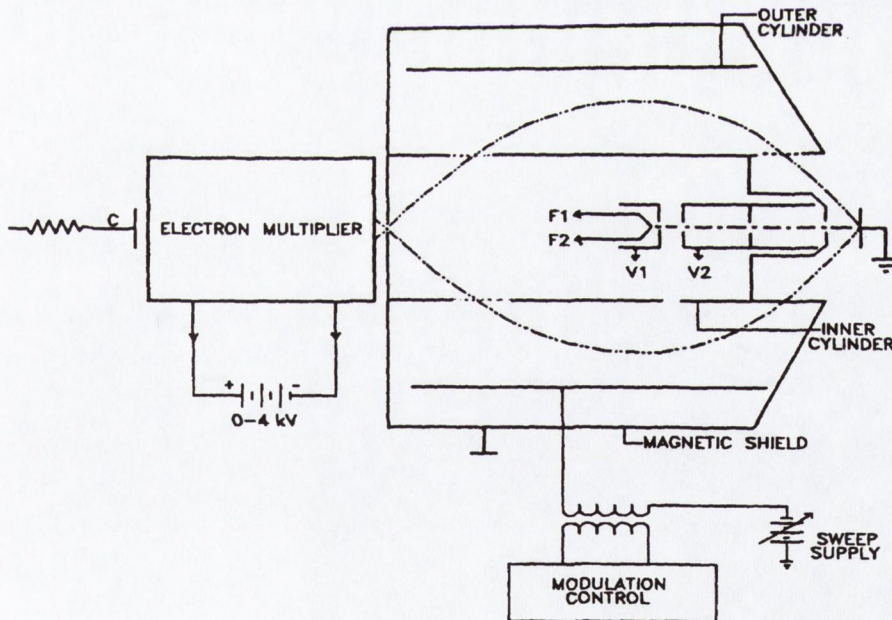


Figure 2.14: A schematic illustration of the layout of a cylindrical mirror analyser. Reproduced from [38].

Backscattered electrons enter the analyser through an annular aperture in the inner cylinder. This cylinder is grounded, while a deflecting potential is applied to the outer cylinder. The trajectory of electrons travelling in the resulting electrostatic field will be deflected by an amount which depends inversely upon their kinetic energy. Electrons with lower energies will be deflected to a greater extent than those with higher energies. The deflecting potential is chosen so that only electrons of a particular energy E_0 will have the correct trajectory to pass through the exit aperture at the opposite end of inner cylinder. The analyser current will be given by the number of electrons $N(E_0)$ passing through the exit aperture. Between the exit aperture and the collector, an electron multiplier is used to amplify the analyser current to a level which can be detected by a lock-in amplifier. Sinusoidal modulation of the deflecting potential shifts the energy window for electron transmission above and below the value specified by the d.c. component. The first harmonic component of this signal, which can be measured using lock-in detection, gives the differential signal $dN(E)/dE$.

Because the primary beam is generated from a hot filament source, the incident electrons will have a finite angular spread. As a result, electrons with the same energy may be backscattered so that they enter the analyser at different angles. This means that the signal passing through the exit aperture will display an energy spread which is degraded by the angular spread of the incident electrons. As a result, both the energy resolution and transmission of the analyser are degraded by the angular spread of the source. A good analyser should be capable of focussing electrons of the same energy but different angles of injection at the exit aperture. In the CMA this is achieved by choosing a mean injection angle such that electrons which enter at a steeper angle and so need greater deflection to reach the exit aperture, have

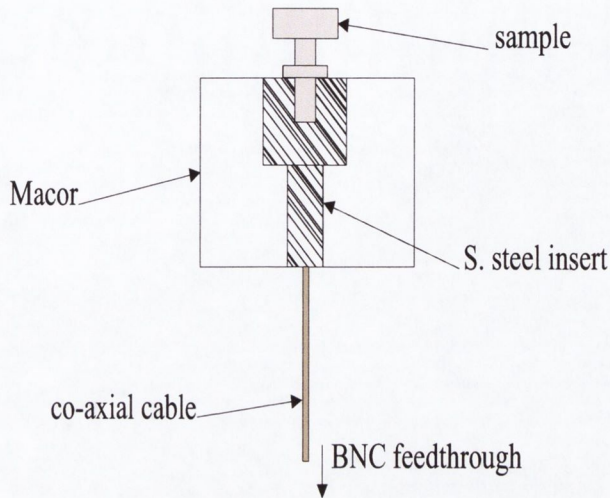


Figure 2.15: Schematic illustration of the sample stage used for AES analysis. The Macor block isolates the stainless steel insert and sample from ground. A co-axial cable connects the insert to a BNC feedthrough, which can be grounded directly or through an ammeter to measure the target current.

a larger distance to travel in the region of the deflecting field. This condition is satisfied designing the analyser in such a way that it accepts a conical annulus of electrons ($\sim \pm 6^\circ$ [39]) about a mean angle of $\alpha = 42.3^\circ$.

In the experimental set-up, the sample sits in a stainless steel insert, which is isolated from ground by a Macor block (figure 2.15). The latter is fixed to a double-sided O.D. 70 mm CF flange by three threaded stainless steel rods (~ 300 mm long). A coaxial cable connects the steel insert with a BNC feedthrough mounted on one side of the double-sided flange. The whole assembly is mounted on an $x - y - z$ translator so that the sample may be positioned directly beneath the CMA optics.

A beam energy of 3 keV and a filament current of 3.2 A were used for all measurements. The emission current ranged between 0.4 mA and 1.4 mA, giving a target current of $\sim 2\mu\text{A}$ and $\sim 8\mu\text{A}$ respectively. The deflecting po-

tential was ramped by a Perkin-Elmer 11–500A AES control unit. A SR 850 DSP lock-in amplifier from Stanford Research Systems [40] was used to output a $0.5 V_{rms}$ sinusoidal signal of frequency 12 kHz. This signal was fed into the AES control and acted as a reference for the modulation of the deflecting potential. A peak-to-peak modulation of 2 eV was used in all experiments. The current passing through the exit aperture of the analyser was amplified using a Channeltron model 4839 electron multiplier [41], held at an accelerating potential of ~ 1 kV using a Perkin-Elmer 32–100 multiplier power supply. The first harmonic of the collector current was separated and converted to a voltage using the lock-in amplifier. A lock-in sensitivity of $100 \mu\text{V}$ was used to detect the Auger signal. Originally, this signal (y -axis) and a signal proportional to the d.c. component of the deflecting potential (x -axis) were used to run a Hewlett-Packard plotter. Later, these signals were fed through one digital multimeter and the lock-in amplifier to a GPIB PC interface card, where the data was acquired in *.dat format, using a programme written by D. Kashanin in the Lab Windows CVI environment. The latter method provides a much more accurate format for quantitative analysis. The scan speed was typically set at $1 \text{ eV}\cdot\text{s}^{-1}$, with scan ranges of 0–750 eV, so that a single scan takes approximately $12\frac{1}{2}$ minutes.

Atomic concentrations are calculated in the manner described by Davis *et al.* [42] and McGuire [43]. The atomic concentration C_X of element X is given by:

$$C_X = \frac{I_X/S_X d_X}{\sum_{\alpha} (I_{\alpha}/S_{\alpha} d_{\alpha})} \quad (2.23)$$

where I_X is the peak-to-peak amplitude of the largest Auger transition measured for the element, S_X is a relative Auger sensitivity factor, taken from reference [42]. The main Auger transition peaks for pure elemental standards are marked in spectra also given in reference [42]. The summation is over one

peak per element present on the surface. The scaling factor d_X is included so that concentrations may be determined from peaks measured under different conditions, this is given by:

$$d_X = L_X E_{M,X} I_{P,X} \quad (2.24)$$

where L_X is the lock-in sensitivity, $E_{M,X}$ is the modulation energy and $I_{P,X}$ is the primary beam current. When calculating concentrations using peak-to-peak values taken from the same spectrum, this scaling factor can be disregarded.

2.2 STM tips

A range of different materials and techniques has been used to prepare the STM tips used during this work. A brief overview of the characteristics of these tips is given in the following sections.

W tips

A $\phi = 0.5 \text{ mm} \times 10 \text{ mm}$ wire was clamped into a tip holder at one end. The tip holder was fitted to a modified micrometer screw which allowed a precise positioning of the tungsten wire in a 2 M NaOH solution. The tungsten wire acts as the anode during the electrolytic process, while a fully submerged stainless steel cylindrical foil acts as the cathode. Under an applied d.c. bias, preferential etching at the air/electrolyte interface occurs, with the oxidation of the anode to form soluble WO_4^{-2} anions which flow away from the active etching region. This leads to a *necking-in* of the wire in the active etching region. The process continues until the thinned region parts under the weight of the submerged portion drops off. The etching process is controlled by an

electronic shut-off control with a ~ 9 V d.c. output built by P. Flanagan and calibrated by Dr. C. Seoighe. This unit breaks the electrolytic circuit once a pre-set etching current, corresponding to the drop-off point, is reached. The fast shut-off of the electrolytic circuit at drop-off has been found essential to produce very sharp tips [44–46]. The tips were rinsed with propanol-2-ol before insertion into vacuum. The tips were then ion-etched with Ar^+ ions to remove the layer of WO_3 oxide. The typical parameters for this process are given in table 2.1.

The procedure described above gives satisfactory results, leading to the production of very stable and sharp tips.

Alternative procedures, such as the *floating layer technique*, the *loop technique* and the *wire insulation technique* involve confining the active region to a very small volume. A more detailed description of these techniques is given in [13]. Among these techniques, only the latter has been extensively used to fabricate the tips used for this thesis. The *wire insulation* procedure consists of covering the submerged part of the W wire with an insulating layer, specifically a PTFE tube. This physically confines the active region [47] and protects the dropped-off part which can produce a sharper tip [48]. This method was used also to fabricate Manganese-Nickel, Iron and Chromium tips.

Etching time (min.)	Ion energy (keV)	Target current (mA)
20	2	15-30
10	1	5-10
5	0.5	≤ 1

Table 2.1: Typical parameters for Ar^+ ion etching of W STM tips.

PtIr tips

Platinum Iridium tips were prepared by mechanical cutting. A $\phi = 0.25$ mm Pt₈₀Ir₂₀ wire was simultaneously pulled and cut using a pair of snips. PtIr tips do not require ion-etching in vacuum since they do not oxidize. This fact makes PtIr tips very fast to fabricate. However, this method is not very reproducible and the tips produced are generally of lower quality than the electrolytically etched W tips.

MnNi tips

Antiferromagnetic (AF) tips have been proposed for magnetically-sensitive spin-polarised STM (SPSTM) studies [2, 49], as they remove the problem of tip magnetostriction, while the magnetic order of the tip does not change with an externally applied magnetic field. The family of ordered equiatomic binary alloys of manganese, MnMe where Me may be Pd, Pt, Au, Ir or Ni, are particularly attractive for this use. These alloys usually have high magnetic moments, are mechanically hard and have high Néel temperatures. MnNi tips were prepared by Dr. Murphy from a 99.9 % pure MnNi ingot. A full description of the preparation procedure is given in [13, 50]. In brief, cylindrical rods of $\phi = 0.5$ mm \times 13 mm were etched in an aqueous solution of (% 10 volume) saturated HCl. It was found necessary to physically confine the etching region: the *loop technique*, the *floating layer technique* and the *wire insulation technique* were used, the last two giving the most satisfactory results. Tips prepared in this manner were ion-etched in vacuum using the same parameters as those used for the W tips. Some excellent results were obtained using these tips, with atomic resolution images obtained on oxygen covered W(100) [50, 51], on Fe₃O₄(001) [24] and on Fe islands on Mo(110) [12, 52].

Cr tips

Cr tips were prepared by Dr. Murphy [13]. They were etched in a 2 M NaOH solution using the *wire insulation technique*. In vacuum they were ion etched to remove the oxide layer. These tips were used in a few sessions on the Mo(110) and Fe₃O₄(001) surfaces achieving a reasonable resolution.

Fe tips

Iron tips were prepared from 99.98 % pure Fe wire ($\phi = 0.25$ mm), using the *loop technique*. An aqueous solution of 10 % volume saturated HCl acid was used as the electrolyte, while the etching bias was typically 0.3-0.6 V d.c. The tips were rinsed with distilled water and propan-2-ol, immediately after drop-off.

The tips were ion-etched in vacuum, using similar parameters to those used for W tips. They were used a few times in sessions on the magnetite (Fe₃O₄) surface [24]. However, they were easily blunted by minor tip crashes and tip material tended to be deposited on the surface. Also, they were unsuitable for STM experiments in a variable magnetic field, due to their considerable magnetostriction [24].

Chapter 3

Iron oxides

3.1 Introduction

Magnetite is part of a family that includes sixteen iron oxides, hydroxides and oxide hydroxides. Iron oxides are widespread in nature and are of interest to many scientific disciplines (Figure 3.1). The major applications of iron oxides include pigments for paints and the construction industry, magnetic pigments and ferrites, catalysts for industrial syntheses and raw material for the iron and steel industry [53]. In more recent times magnetite has been extensively studied because of its half-metallic ferromagnetic properties. The electronic density of states at the Fermi level is completely spin polarized, making magnetite a potential candidate for applications in spin electronics.

Figure 3.2 shows the phase relations in the system $\text{FeO}-\text{Fe}_2\text{O}_3$ [54]. Heavy lines are boundary curves separating stability fields of the various condensed phases, and light dash-dot lines are oxygen isobars. The oxygen pressure is expressed in atmospheres.

In the following sections a brief description of each of the iron oxides is given.

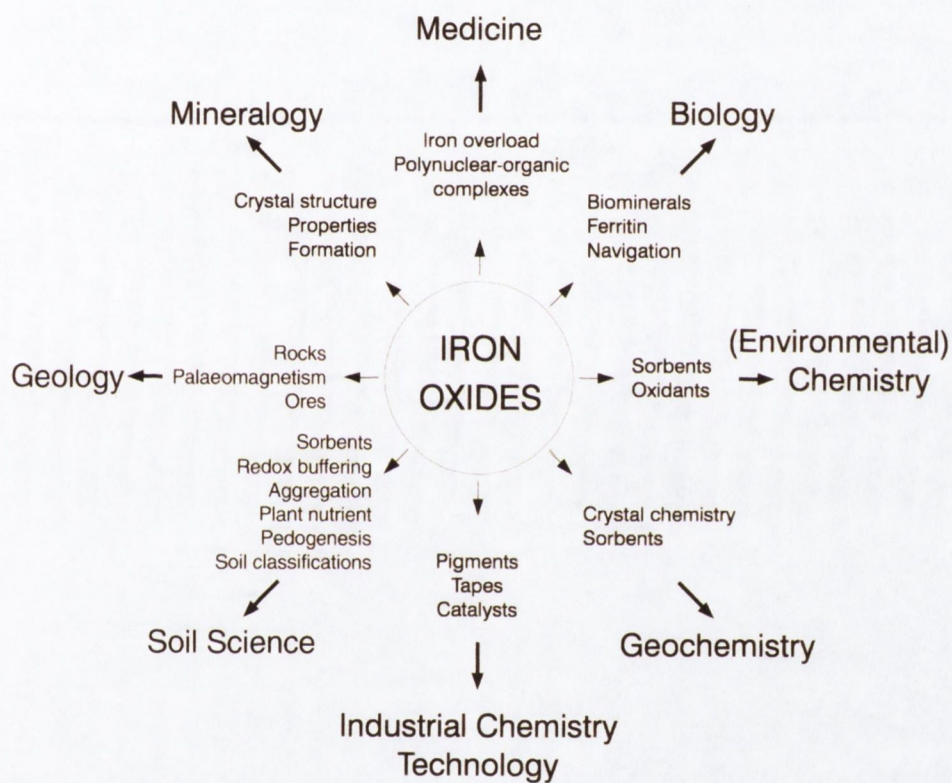


Figure 3.1: The widespread spectrum of research involving iron oxides. Reproduced from [53].

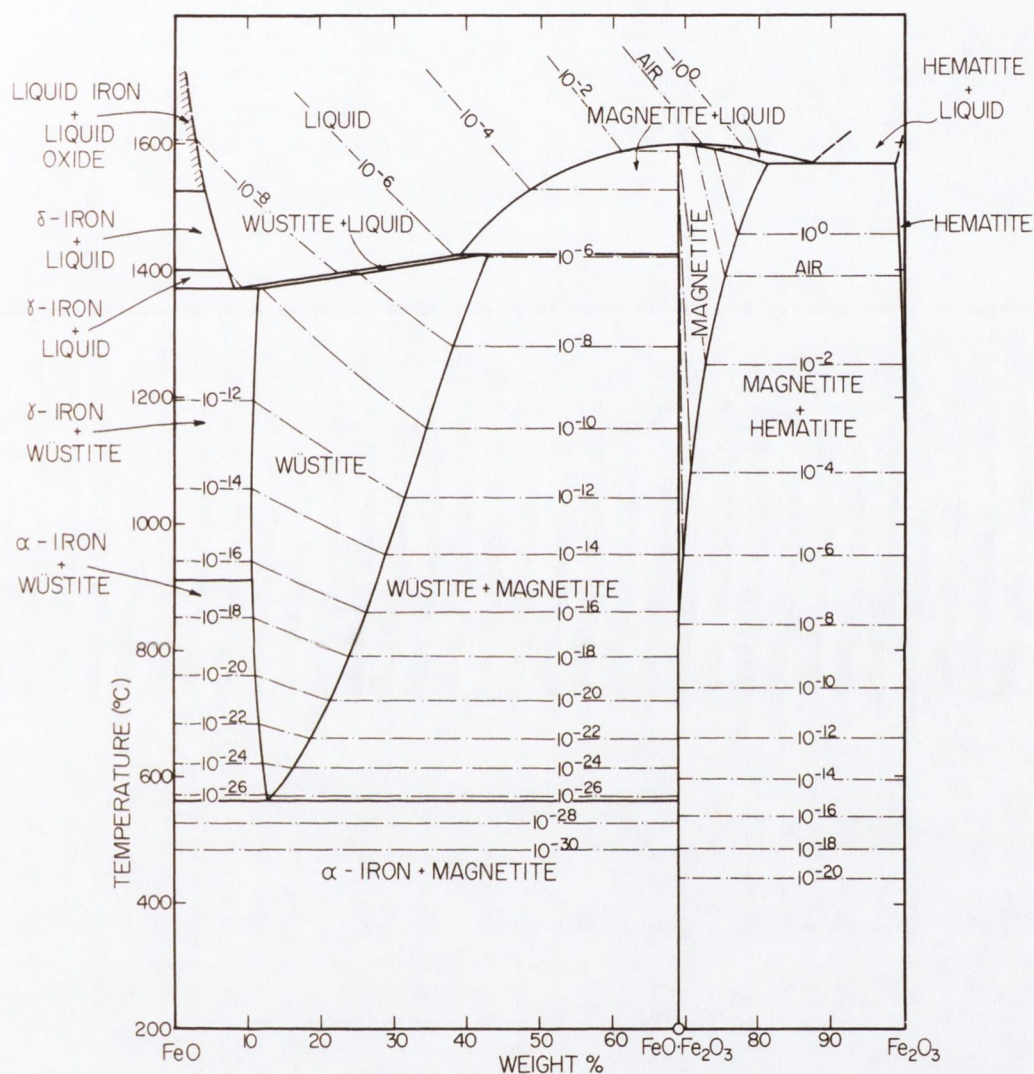


Figure 3.2: Phase relations in the system of FeO–Fe₂O₃. Heavy lines are boundary curves separating stability fields of the various condensed phases, and light dash-dot lines are oxygen isobars. The oxygen pressure is expressed in atmospheres. Reproduced from [54].

3.2 Wüstite, Fe_{1-x}O

Stoichiometric wüstite, FeO , cannot exist as a stable phase at low pressure or at pressures exceeding 10 MPa. The non-stoichiometry is accommodated by oxidation of a proportion of the metal ions and the creation of cation vacancies. A stable, cation-deficient phase, Fe_{1-x}O (with $1 - x$ ranging from 0.83 to 0.95) exists at 0.1 MPa and at temperatures higher than 840 K. At lower temperatures it disproportionates into Fe and Fe_3O_4 [53]. The formula Fe_{1-x}O indicates that the vacancies are located on the Fe^{2+} sublattice, accompanied by the oxidation of two Fe^{2+} ions to Fe^{3+} to maintain charge neutrality. Its crystal structure is similar to that of rocksalt NaCl. It can be regarded as consisting of two interpenetrating face-centred cubic structures of Fe^{2+} and O^{2-} . The cubic unit cell, shown in fig. 3.3, ranges from 0.428 – 0.431 nm, depending on the vacancy content. Wüstite is paramagnetic at room temperature and becomes antiferromagnetic at temperatures below ~ 200 K. The Neel temperature strongly depends on the deviation from the 1:1 stoichiometry [55]. Wüstite is an important intermediate in the reduction of iron ores.

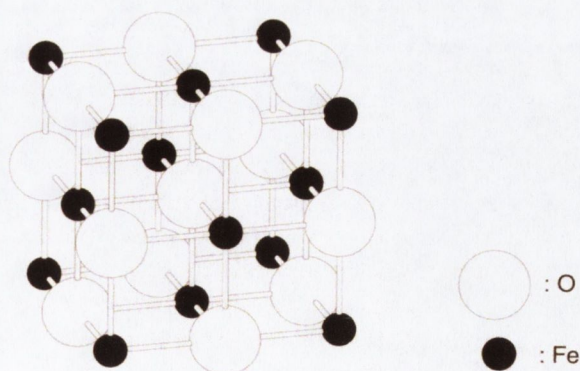


Figure 3.3: Unit cell of wüstite. Reproduced from [53].

3.3 Magnetite, Fe_3O_4

The structure of magnetite is that of an inverse spinel. It has a face-centred cubic unit cell based on 32 O^{2-} ions which are regularly cubic close packed along the $\langle 111 \rangle$ directions (see fig. 3.4). The unit cell edge constant is $a = 0.83963$ nm [56]. There are eight formula units per unit cell. Magnetite contains both divalent and trivalent iron ions. Its formula can be written as $Y_A[\text{XY}]_B\text{O}_4$, where $X = \text{Fe}^{2+}$, $Y = \text{Fe}^{3+}$ and A and B denote tetrahedral and octahedral sites, respectively. This formula means that one half of the ferric Fe^{3+} ions occupies $\frac{1}{8}$ of the available tetrahedral A sites, and the other half of the ferric ions, together with an equal amount of ferrous Fe^{2+} ions, occupy $\frac{1}{2}$ of the octahedral B sites. The Fe ions in the octahedral sites form rows running along the $\langle 110 \rangle$ directions. In stoichiometric magnetite the ratio of divalent to trivalent cations is $\text{Fe}^{2+}/\text{Fe}^{3+} = 0.5$. Non-stoichiometric magnetite has a cation deficient Fe^{3+} sublattice [53].

Rapid electron hopping between the Fe^{2+} and Fe^{3+} ions in the octahedral sites makes magnetite a moderately good electrical conductor at room temperature [57]. The electrical conductivity of magnetite at room temperature is $\sigma \approx 200 \Omega^{-1}\text{cm}^{-1}$ [9]. Below the Verwey temperature T_V magnetite undergoes a phase transition and the electrical resistivity changes by two orders of magnitude. This transition occurs in bulk crystals over a small temperature interval in the neighborhood of $T_V = 120$ K [58]. Although the Verwey transition has been the subject of intensive investigations during the past decades, the nature of the electrical transition is not fully understood. However, it is believed that at T_V the electron hopping freezes out, leading to an ordered array of Fe^{2+} and Fe^{3+} ions with static charges. Magnetite is ferrimagnetic at room temperature and has a Curie temperature T_C of 858 K. The A and B cation sites form the basis for two interpenetrating sublattices. Below T_C , the

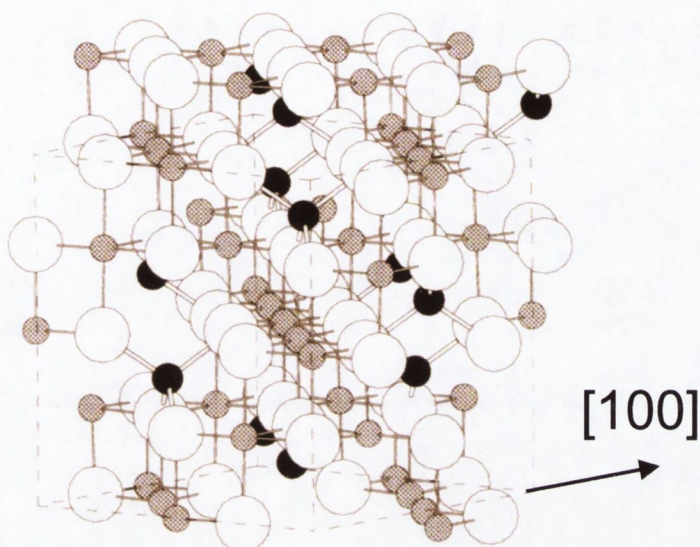


Figure 3.4: Unit cell of magnetite. Reproduced from [53].

spins on the A and B sites are antiparallel and the magnitudes of the two types of spins are different: this causes ferrimagnetism. The spin arrangement can be written as $\text{Fe}^{3+}\downarrow[\text{Fe}^{3+}\uparrow\text{Fe}^{2+}\uparrow]\text{O}_4^{2-}$. The net magnetic moment per formula unit is $4 \mu_B$, which corresponds to the magnetic moment of an octahedral B site Fe^{2+} , since the $5 \mu_B$ moments of the Fe^{3+} ions in the A and B sites are opposite and cancel each other out [59].

3.4 Maghemite, $\gamma\text{-Fe}_2\text{O}_3$

Maghemite (from *magnetite* and *hematite*) has a structure similar to that of magnetite. It differs from magnetite in that all the Fe^{2+} are oxidized to Fe^{3+} . Maghemite has a unit cell with a lattice parameter $a = 0.8352 \text{ nm}$ [56]. To maintain charge neutrality, vacancies have to be introduced. Vacancies are mainly created on the B sites [60]. Instead of $\gamma\text{-Fe}_2\text{O}_3$, one can write $\text{Fe}_{2.67}\text{O}_4$

or $\text{Fe}^{3+}_A[\text{Fe}^{3+}_{5/3}\square_{1/3}]_B\text{O}_4$, where \square indicates an octahedral vacancy. The number of vacancies δ can vary from 0 for stoichiometric Fe_3O_4 up to $\frac{1}{3}$ for stoichiometric $\gamma\text{-Fe}_2\text{O}_3$. Because no Fe^{2+} ions are present, electron hopping is not possible and maghemite is an insulator. Maghemite is a ferrimagnet with a magnetic moment of $3\frac{1}{3}\mu_B$. Maghemite is widely used as a magnetic pigment in the electronic recording devices [53].

3.5 Hematite, $\alpha\text{-Fe}_2\text{O}_3$

Hematite is the most common iron oxide, usually referred to as rust. Hematite is isostructural with corundum. It is the only iron oxide with a hexagonal close packed lattice of O^{2-} anions as its basis (see fig. 3.5). The Fe^{3+} ions fill $\frac{2}{3}$ of the octahedral sites. The unit cell is hexagonal with $a = 0.5035\text{ nm}$ and $c = 1.372\text{ nm}$ [56]. Hematite is paramagnetic above 956 K (T_C). Between T_C and 260 K (T_M , the Morin temperature), it is weakly ferromagnetic. Below T_M , hematite undergoes a phase transition to an antiferromagnetic state [53].

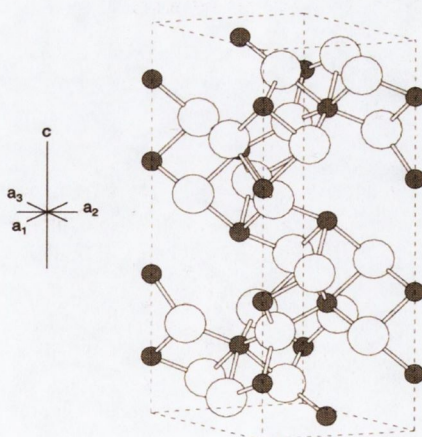


Figure 3.5: Unit cell of hematite. Reproduced from [53].

Chapter 4

The (001) surface of Fe_3O_4

4.1 Introduction

Magnetite is the oldest known magnetic material: its magnetic properties were discovered around 1500 B.C. In 1915 Bragg established the details of its structure using X-ray diffraction [61]. Spinel ferrites, which are obtained by sintering iron oxide with other oxides resulting in the mixed series $\text{M}_x\text{Fe}_{3-x}\text{O}_4$, with M a variety of metals, are the basic materials in many technological applications. They are used in the cores of electromagnets, in microwave resonant circuits, in computer memory cores and in high density magnetic recording media. Magnetite itself plays an important role in geology because of its influence on the earth's magnetic field and in biology because it's used as a navigation means by magnetotactic bacteria. Magnetite is also of fundamental importance as a catalyst in inorganic processes such as the synthesis of ammonia and the water gas shift reaction for the production of hydrogen, and in organic processes such as the dehydrogenation of ethyl benzene to styrene [53]. Furthermore, since magnetite is redox-active, it can reduce toxic species such as chlorinated organics and chromate. In the last

decade, the great demand for high density magnetic recording media, combined with the possibility of imaging the atomic structure and the electronic properties of the surface provided by STM, has boosted a great interest in magnetite and its related iron-oxides. In particular, attention was focused on the study of the surface reconstruction of magnetite and on its magnetic properties. In the following sections a short review of the main works carried out on Fe_3O_4 is given.

4.2 The electrostatic model

The electrostatic model was proposed by Tasker [62, 63] and provides an explanation of why polar surfaces (such as the $\text{Fe}_3\text{O}_4(001)$ surface) must reconstruct. As shown by Bertaut [64], when there is a dipole moment in the unit cell perpendicular to the surface, the surface energy diverges and is infinite. Therefore such surfaces cannot exist. Tasker classifies the surfaces of any ionic or partly ionic materials into three types (see Fig. 4.1). A type-1 surface is neutral with equal number of anions and cations in each plane. Examples are the (100) and (110) surfaces of rocksalt metal oxides, such as MgO and NiO. A type-2 surface is charged but there is no dipole moment perpendicular to the surface because of the symmetrical stacking sequence. The surface energies are small and limited relaxations of the surface ions may be enough to stabilize them. An example is the (111) surface of the fluorite structure terminated with an anion plane. The type-3 surface is charged and has a dipole moment perpendicular to the surface. These surfaces have an infinite surface energy and therefore cannot exist as simple bulk terminations. Examples are the (111) surfaces in the rocksalt structure: these surfaces are called *polar*. Type-3 surfaces can only occur if the surface reconstructs or

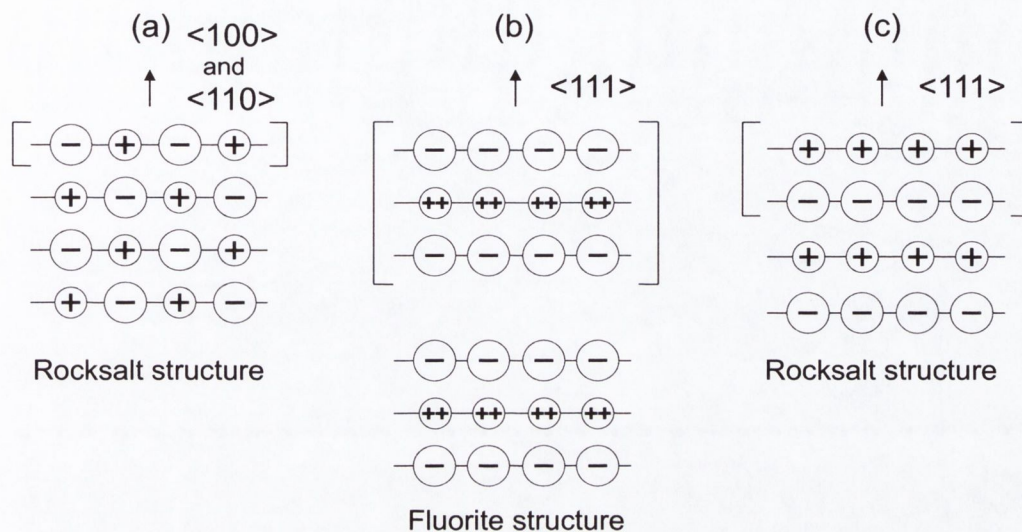


Figure 4.1: The three types of surfaces of ionic materials. (a): type-1 for $\langle 100 \rangle$ and $\langle 110 \rangle$ surfaces of rocksalt structures. (b): type-2 for $\langle 111 \rangle$ surfaces of fluorite structures. (c): type-3 for $\langle 111 \rangle$ surfaces of rocksalt structures. The repeated units for planar charge density are shown in square brackets.

if it undergoes a charge redistribution. An exception is made by ultra-thin films, in which the surface energy is still finite.

The structure of magnetite can be described as a stack of (001) alternating layers containing either Fe^{3+} cations in tetrahedral A sites or O^{2-} anions and $\text{Fe}^{2.5+}$ cations in octahedral B sites. Therefore the bulk-truncated surface of $\text{Fe}_3\text{O}_4(001)$ can be terminated either at the A or at the B plane. The charges per unit cell are $+3$ for the tetrahedral termination and -3 for the octahedral one. A dipole moment in the unit cell perpendicular to the surface is present and therefore the bulk-terminated $\text{Fe}_3\text{O}_4(001)$ surface is a polar type 3 one. Neither of the two bulk-truncated terminations is possible.

4.3 The electron counting model

A partly covalent nature of the Fe₃O₄ bonds, due to a strong mixing between the O 2*p* and Fe 3*d* orbitals was proven by de Groot [65]. Barbieri [66] has calculated that the ionic character of the Fe-O bonds is about 50 %. The electron counting model, developed by Pashley [67] to explain the reconstructions on compound semiconductors such as GaAs and ZnSe, was extended to oxides by Lafemina [68]. According to this model, the lowest energy surface structure is the one where all the dangling bonds on the electropositive elements are empty and the dangling bonds on the electronegative elements are full. Therefore, a stable surface is created when the number of available electrons exactly matches this requirement. As a consequence, no net charge is present on the surface. It must be kept in mind that this model does not uniquely determine the surface reconstruction. Several possible structures may fit the model. However, any successful structural model must satisfy the electron counting model. In other words, the electron counting model is a necessary but not sufficient condition to explain a certain surface reconstruction. Below we apply the electron counting model to the possible two bulk-terminated surfaces and to two types of reconstructions that have been proposed.

4.3.1 Fe–O dangling bonds

In the spinel and inverse spinel structure, cations have two types of coordination to the anions: tetrahedral and octahedral. Fe_{tetr} atoms have 4 bonds to the surrounding O atoms. Since their valence state is +3, they share 3 e⁻ divided over 4 bonds, *i.e.* 3/4 e⁻ per bond. Fe_{oct} atoms have 6 bonds to the surrounding O atoms. The octahedral iron ions consist of Fe_{oct}²⁺ and Fe_{oct}³⁺: since these two bonding configurations must be present in equal proportions

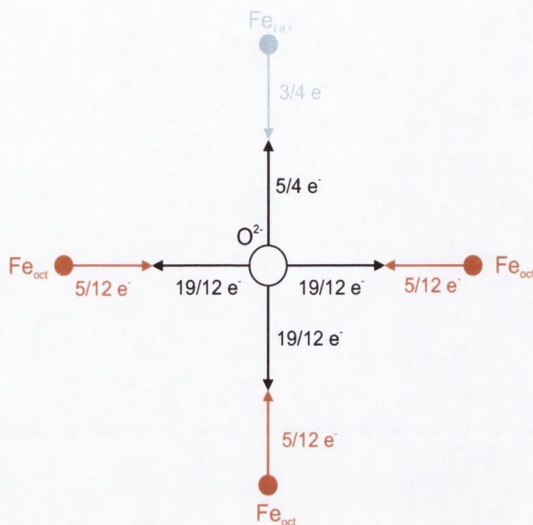


Figure 4.2: Each O atom bonds with 1 Fe_{tetra} and 3 Fe_{oct} atoms. Assuming a covalent nature of the bonds, each bond must be filled with 2 electrons. The number of e^- shared by O and Fe atoms are shown in the schematic.

in order to achieve charge neutrality, an average charge of +2.5 is assumed for the Fe_{oct} ions. Therefore, the Fe_{oct} ions share $2.5 e^-$ divided over 6 bonds, *i.e.* $5/12 e^-$ per bond. Each O atom bonds with 1 Fe_{tetra} and 3 Fe_{oct} . To fill the bond with the Fe_{tetra} , an O shares $(2 - 3/4) = 5/4 e^-$. To fill its three bonds with Fe_{oct} , an O shares $(2 - 5/12) = 19/12 e^-$. A schematic of the bonds between O and Fe atoms and the number of electrons shared in these bonds is shown in figures 4.2 and 4.3.

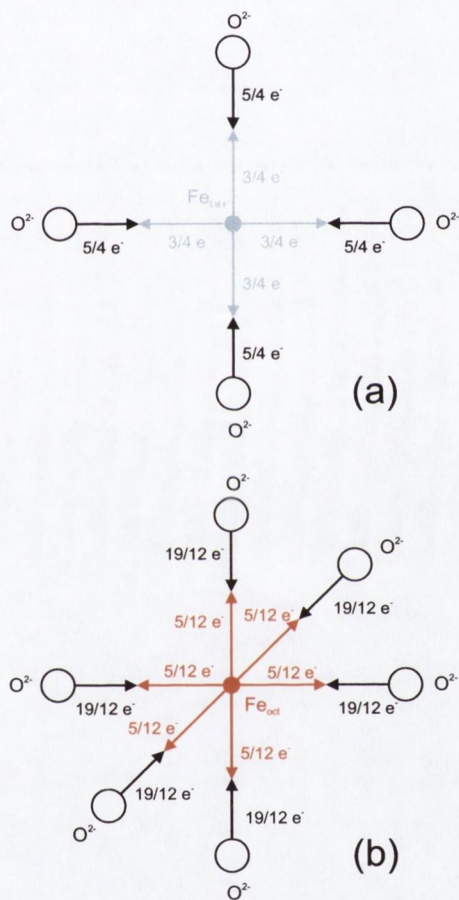


Figure 4.3: (a): $\text{Fe}_{tetr}-\text{O}$ bonds. (b): $\text{Fe}_{oct}-\text{O}$ bonds. The number of e^- shared by O and Fe atoms are shown in the schematic.

4.3.2 Tetrahedrally bulk-terminated surface:

full *A* layer

There are 2 Fe_{tetr} atoms, 4 Fe_{oct} atoms and 4 O atoms per unit cell with dangling bonds, as shown in Fig. 4.4. Each of the 2 Fe_{tetr} has 2 dangling bonds: these 4 dangling bonds contain a total of $(4 \times 3/4) = 3 e^-$. The 4 Fe_{oct} atoms have one dangling bond each; these 4 dangling bonds contain a total of $(4 \times 5/12) = 1.67 e^-$. The total number of e^- contained in the dangling bonds of the electropositive elements is $(3 + 1.67) = 4.67 e^-$. Each of the 4 O atoms has one broken bond to a Fe_{oct}. This means that the total number of e^- contained in the dangling bonds of the electronegative elements is $(4 \times 19/12) = 6.33 e^-$ instead of the $8 e^-$ required to completely fill the 4 bonds. According to the autocompensation model, the most stable surface is created when the anions dangling bonds are full and the cations dangling bonds are empty. To completely fill the anions dangling bonds a total of $(8 - 6.33) = 1.67 e^-$ can be transferred from the cations dangling bonds, but this transfer will not lead to a state where all the cations dangling bonds are empty: an excess of $3 e^-$ is present on the surface that, therefore, is not stable.

4.3.3 Octahedrally bulk-terminated surface:

full *B* layer

A bulk-terminated surface at a *B* layer does not contain any Fe_{tetr}: therefore their bonds are not broken. If we consider a unit cell, it contains 4 Fe_{oct} atoms and 8 O atoms (see Fig. 4.5). The 4 Fe_{oct} atoms have one dangling bond each. These bonds contain a total of $(4 \times 5/12) = 1.67 e^-$. Of the 8 O atoms, 4 have one dangling octahedral bond, and the other four have one

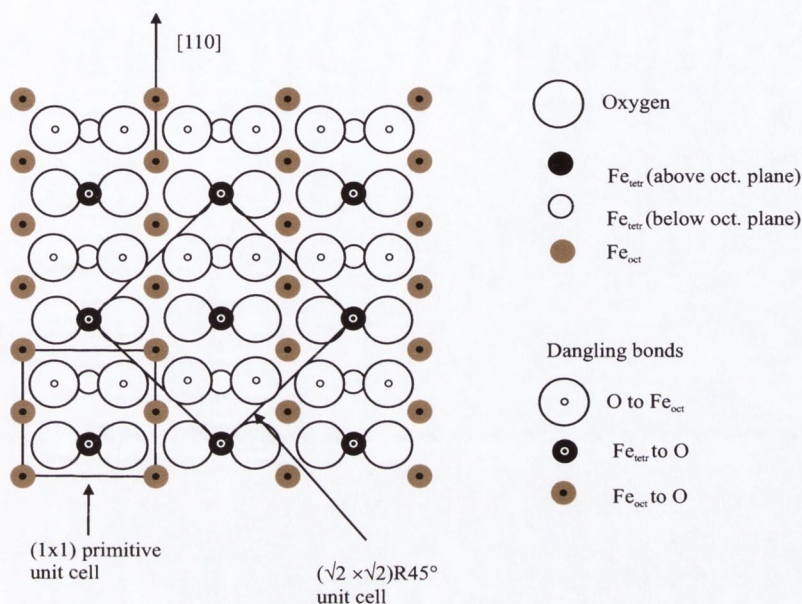


Figure 4.4: Tetrahedrally bulk-terminated surface of $\text{Fe}_3\text{O}_4(001)$: full A layer. The dangling bonds of Fe_{tetr} , Fe_{oct} and O atoms are shown.

dangling tetrahedral bond. Therefore, the O dangling bonds contain a total of $(4 \times 19/12) + (4 \times 5/4) = 11.33 e^-$. Transferring all the electrons from the Fe to the O dangling bonds leads to a total of $(1.67 + 11.33) = 13 e^-$ in the O dangling bonds. This leaves the surface with a charge deficiency of $3 e^-$, since the 8 O atoms at the surface require a total of $16 e^-$ to fill their dangling bonds and satisfy the electron counting model. Therefore this type of surface is also not stable.

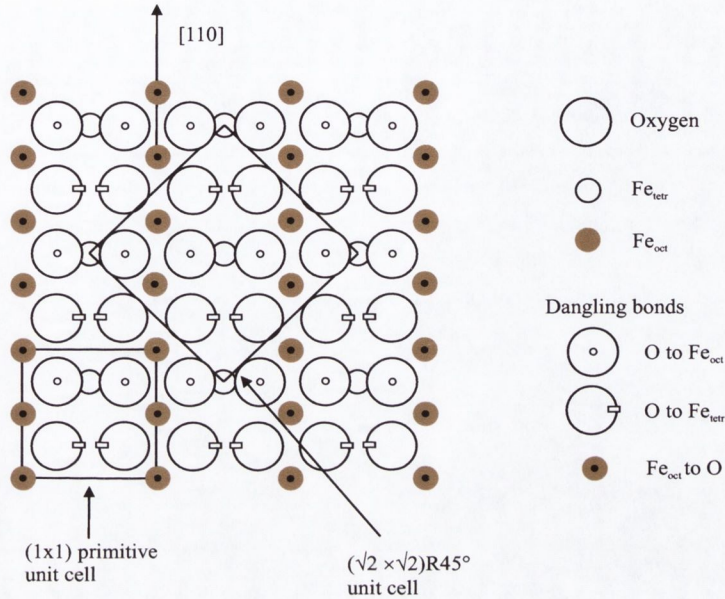


Figure 4.5: Octahedrally bulk-terminated surface of $\text{Fe}_3\text{O}_4(001)$: full B layer. The dangling bonds of Fe_{oct} and O atoms are shown.

4.3.4 Tetrahedrally terminated surface: half-filled A layer

There are 1 Fe_{tet} atom, 4 Fe_{oct} atoms and 6 O atoms per unit cell with dangling bonds, as shown in Fig. 4.6. The Fe_{tet} has 2 dangling bonds that contain a total of $(2 \times 3/4) = 1.5 e^-$. The 4 Fe_{oct} atoms have one dangling bond each; therefore they contain a total of $(4 \times 5/12) = 1.67 e^-$. Of the 6 O atoms, 4 have one broken bond to a Fe_{oct} and contain a total of $(4 \times 19/12) = 6.33 e^-$. The remaining 2 O have one broken bond to a Fe_{tet} and contain a total of $(2 \times 5/4) = 2.5 e^-$. The total number of electrons available from the Fe and O dangling bonds is $(1.5 + 1.67 + 6.33 + 2.5) = 12 e^-$. This is exactly the number of e^- required to fill the dangling bonds of the 6 O atoms. Therefore, a termination with a half-filled layer of tetrahedral Fe atoms is a stable surface.

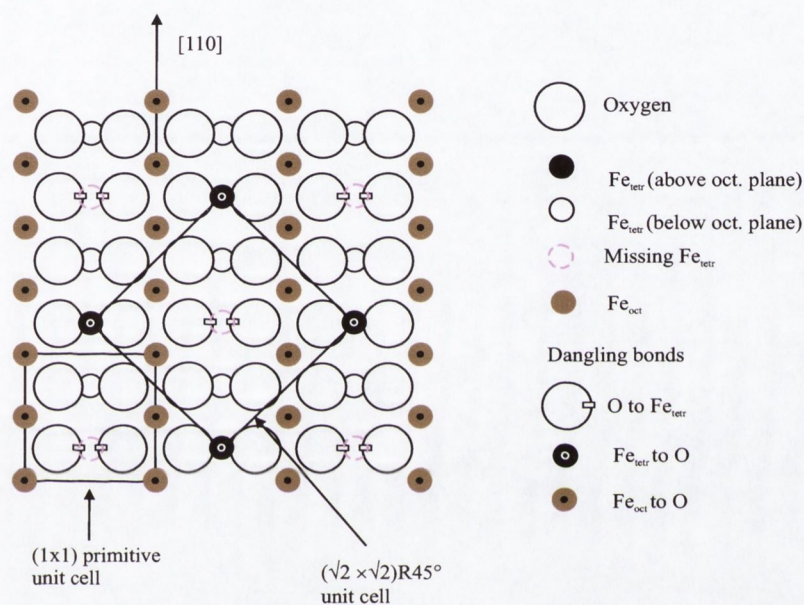


Figure 4.6: Tetrahedrally terminated surface of $\text{Fe}_3\text{O}_4(001)$: half-filled A layer. The $p(1 \times 1)$ unit cell of the unreconstructed surface and the $(\sqrt{2} \times \sqrt{2})R45^\circ$ unit cell of the reconstructed surface are shown, together with the dangling bonds. One missing tetrahedral Fe ion per unit cell, (shown as a dashed circle) produces an autocompensated $(\sqrt{2} \times \sqrt{2})R45^\circ$ reconstructed surface.

4.3.5 Octahedrally terminated surface: oxygen vacancies in the *B* layer

A surface terminated at the *B* layer with 1 O atom missing per unit cell and an appropriate increase or reduction of the Fe_{oct} valencies is auto-compensated. An O vacancy creates 3 dangling bonds on neighbouring Fe atoms. We need to distinguish between two coordination geometries: in one case the O atom is bound to 2 Fe_{oct} in the first layer (*i.e.* the surface layer) and to 1 Fe_{tetr} in the second layer. In the other case the O atom is bound to 3 Fe_{oct} – 2 in the first layer and 1 in the third layer. At the same time, an O dangling bond is removed, *i.e.* either an octahedral or a tetrahedral one, respectively. Fig. 4.7 shows the model proposed by Stanka [69]. In this model, an O atom bound to 3 Fe_{oct} was removed: this choice was guided by atomically resolved STM images. In the unit cell there are 4 Fe_{oct} atoms with 7 dangling bonds to O atoms. They contain $(7 \times 5/12) e^-$. Of the 7 O atoms, 4 have dangling bonds to Fe_{oct} atoms and contain $(4 \times 19/12) e^-$. The remaining 3 O atoms have a dangling bond with Fe_{tetr} and contain a total of $(3 \times 5/4) e^-$. To fill all the 7 O atoms dangling bonds, a total of 14 e⁻ is required. Summing up all the charges from the Fe and O dangling bonds gives $(7 \times 5/12) + (4 \times 19/12) + (3 \times 5/4) = 13 e^-$. The surface is deficient by 1 e⁻. To satisfy the principle of auto-compensation, an extra e⁻ must be supplied. This can be achieved by increasing the valence of the five exposed Fe_{oct} atoms from 2.5⁺ to 2.7⁺.

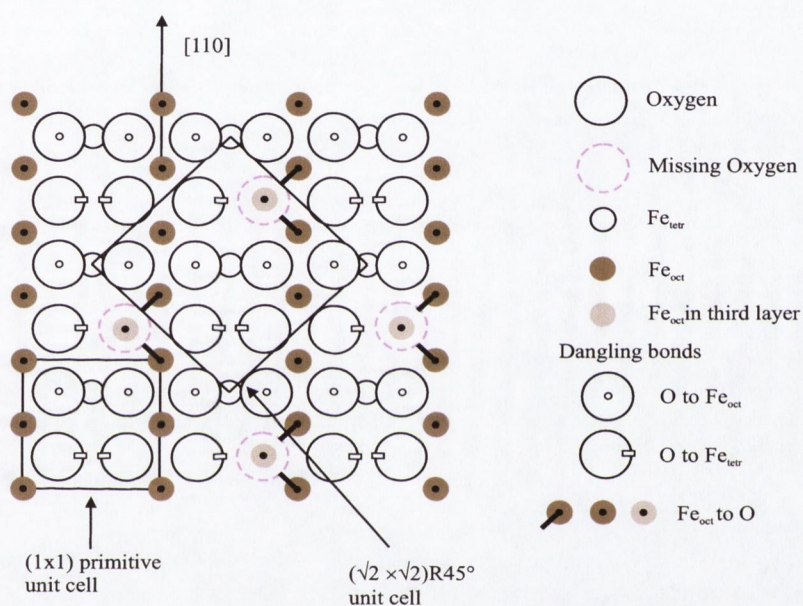


Figure 4.7: Octahedrally terminated surface of $\text{Fe}_3\text{O}_4(001)$: oxygen vacancies in the B layer. The $p(1 \times 1)$ unit cell of the unreconstructed surface and the $(\sqrt{2} \times \sqrt{2})R45^\circ$ unit cell of the reconstructed surface are shown, together with the dangling bonds. The missing O ions are shown as dashed circles.

4.4 Literature review

As shown in the previous two paragraphs, the (001) surface of Fe₃O₄ is not stable unless it reconstructs. Two different models have been presented to explain what the forces driving the reconstruction are. Although the two approaches are different, they lead to the same conclusion and are therefore equivalent.

A $(\sqrt{2} \times \sqrt{2})R45^\circ$ reconstruction is observed both on natural and artificial single crystals [70,71] and on MBE grown thin films [59,72–75]. Different models have been proposed to explain this reconstruction. Tarrach *et al.* [70] have suggested that the surface topmost layer consists of a full ML of tetrahedral Fe ions. Such a surface is non-autocompensated since it would have an excess of $3 e^-$. To achieve a non-polar surface they speculated that half of the Fe³⁺ are reduced to Fe^{0±}. Kim *et al.* [72] have proposed an *A*-terminated surface that is autocompensated due to an ordered array of tetrahedral Fe vacancies (Fig. 4.6). More recently, a study by Chambers *et al.* [74] using XPS, XPD and STM, supports the conclusion that the Fe₃O₄(001) surface is constituted by 1/2 ML of tetrahedral Fe. The same model was used by Mijiritskii *et al.* [76] to explain the experimental results obtained using LEED and LEIS on a thin epitaxial Fe₃O₄(001) film grown by O₂ assisted MBE of Fe on a MgO(001) substrate.

In contrast, Voogt *et al.* proposed a *B*-terminated surface [77]. Autocompensation is achieved by an array of oxygen vacancies accompanied by a variation in the Fe³⁺ to Fe²⁺ ratio per surface unit cell. They speculate that the missing oxygen might act as a 2⁺ impurity and could trap conducting electrons from neighboring sites. This would induce a charge ordering at the surface similar to the one observed by Wiesendanger *et al.* [4,78] with SPSTM on a magnetite natural crystal. The effect of the charge ordering would be

to change the oxidation state of two octahedral iron ions per unit cell from 2.5^+ to 3^+ , providing the missing extra electron, necessary to compensate the surface, to the oxygen dangling bonds.

A *B*-terminated surface was recently proposed by Stanka *et al.* [69] in a study of epitaxial films of $\text{Fe}_3\text{O}_4(001)$ grown on $\text{MgO}(001)$ substrates. This is a variation of the model by Voogt *et al.* The $(\sqrt{2} \times \sqrt{2})R45^\circ$ symmetry and the charge balance are achieved by the removal of one oxygen ion per unit cell and by increasing the charge of the octahedral iron ions from 2.5^+ to 2.7^+ .

Voogt *et al.* have also proposed a *B*-terminated surface where all the Fe ions are oxidized to Fe^{3+} and where one O^{2-} ion per unit cell is replaced by a OH^{1-} group [77]. Gaines *et al.* [71] proposed a surface formed by a FeO-like structure. Recently Rustad [79] suggested a new surface structure based on molecular dynamics investigation. In this model, the tetrahedral Fe ions in the first (third) layer swing down (up) and occupy empty cation sites in the second octahedral Fe plus tetrahedral O layer.

Chapter 5

Characterization and preparation

5.1 Introduction

One set of artificial single crystals of $\text{Fe}_3\text{O}_4(100)$ has been used for this work. The crystals have been grown employing the skull melting technique [80] in the chemistry department of Purdue University, Indiana, by Prof. J.M. Honig [81]. One batch of crystals was sent to RTI GmbH [82] where the crystals were aligned with a precision ranging from $\pm 0.1^\circ$ to $\pm 1^\circ$, cut along the [010] direction and polished by a chemo-mechanical method. A second batch of crystals was sent to Surface Preparation Laboratory (SPL) [83] where the crystals were aligned to 0.5° and mechanically polished using diamond paste with a grain size down to $0.1 \mu\text{m}$. The thickness of these crystals is approximately 0.5 mm instead of 1.2 mm as for the first batch.

X-ray measurements were taken using a powder diffractometer. A $\text{CuK}\alpha_1$ wavelength, corresponding to $\lambda = 1.541 \text{ \AA}$ was used. The diffractogram obtained, shown in figure 5.1, is in very good agreement with the expected crys-

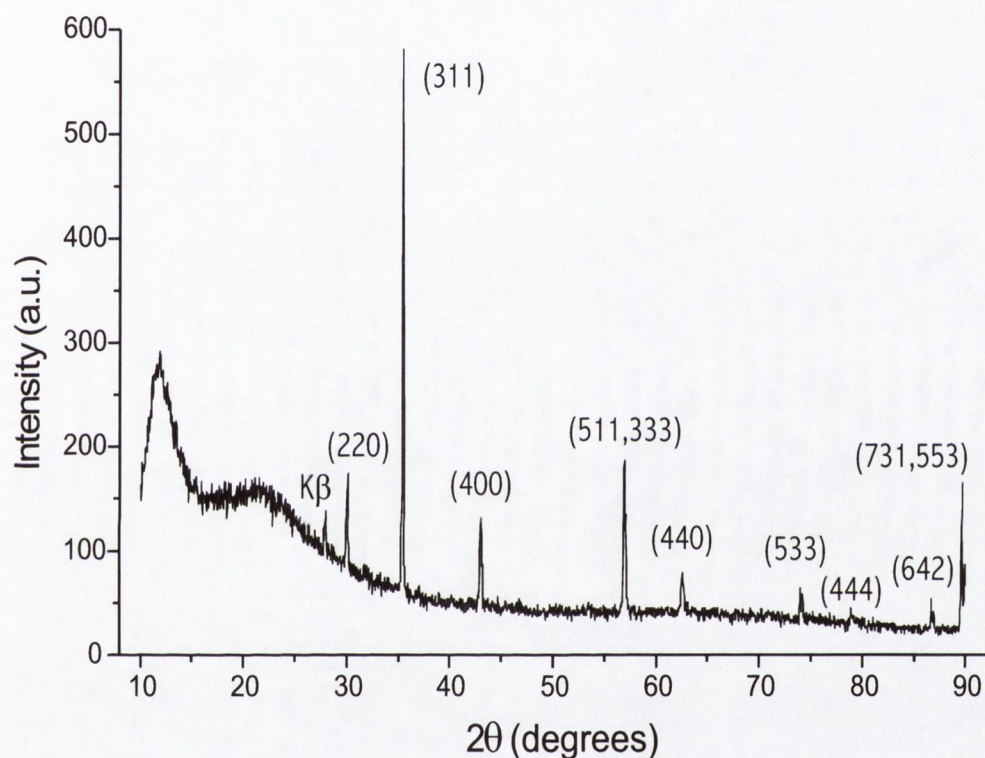


Figure 5.1: X-ray powder diffractogram of Fe_3O_4 . The peaks are indexed with the respective Miller indices. The extraneous peak at $2\theta \approx 14^\circ$ was attributed to the background of the glass slide used as support for the magnetite powder. The spurious peak at $2\theta \approx 28^\circ$ was identified as the $K\beta$ line corresponding to the (311) $K\alpha$ line.

tallographic structure of magnetite. A unit cell length $a = 8.398 \pm 0.010 \text{ \AA}$ was measured.

A four-wire resistance vs. temperature measurement was made between 55 K and 300 K at ~ 1 K intervals. The Verwey transition temperature for a stoichiometric crystal is characterized by a sharp discontinuity in the electrical resistance at about 125 K and by a small first order thermal hysteresis [84]. The transition temperature decreases as the parameter δ in $\text{Fe}_{3(1-\delta)}\text{O}_4$ increases, that is the same as saying that the crystal becomes cation deficient. At the same time the magnitude of the discontinuity decreases and thermal hysteresis becomes sizable. The curve in fig. 5.2 shows a change in the electrical resistivity much smaller than the two orders of magnitude expected for a stoichiometric crystal; a Verwey transition temperature of 108 K was determined, indicating that our crystal is sub-stoichiometric. The value of the resistivity ($\rho = R \cdot S/l$) was calculated estimating the area of the crystal surface ($S \approx 11.25 \text{ mm}^2$) and the distance between the electrical contacts ($l \approx 3 \text{ mm}$). The electrical conductivity at room temperature was found to be $\sigma \approx 116 \text{ \Omega}^{-1} \text{ cm}^{-1}$, comparable with literature data [9].

Creating a well structured, clean surface of a magnetite artificial single crystal is not an easy task. Surface contaminants like carbon, sulphur, calcium and potassium are normally detected. Diverse methods of cleaning a magnetite surface have been proposed. In situ cleavage of magnetite crystals has been attempted [4]. This method ensures a contaminant-free surface since the crystal is cleaved in UHV. Although in situ cleavage does not require further treatment such as annealing or ion bombardment, it produces a very rough surface. A combination of argon ion sputtering and annealing is a common procedure but it can produce changes in the surface magnetism of Fe_3O_4 [85]. Annealing in UHV [70] produces a very well structured surface

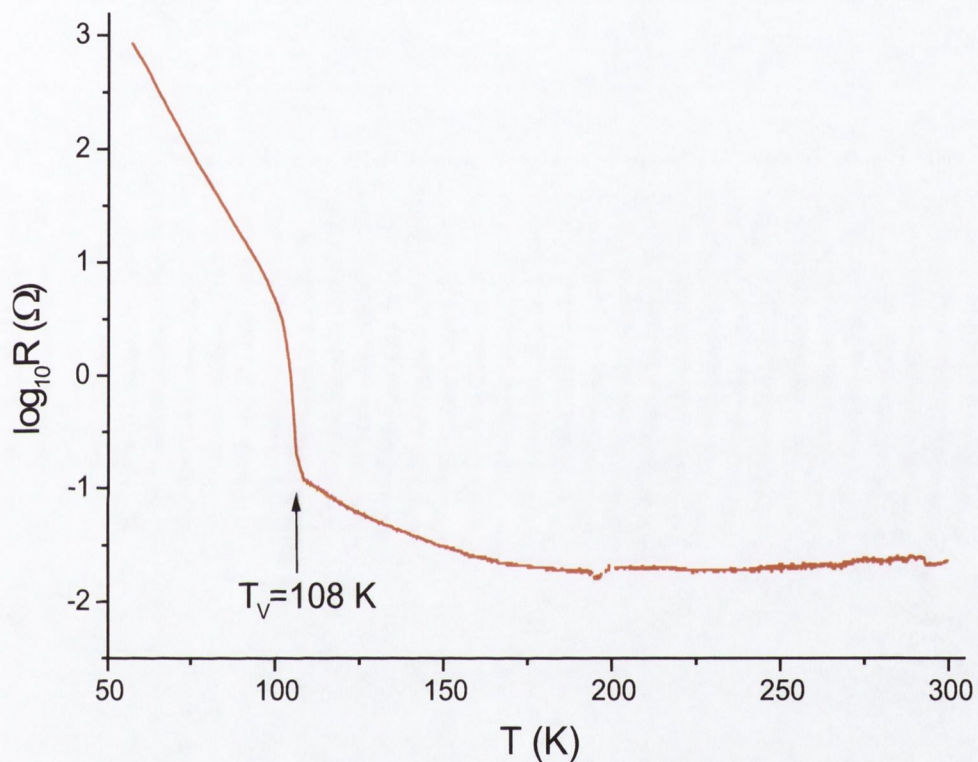


Figure 5.2: Resistance vs. temperature curve for an artificial Fe_3O_4 crystal. A four-wire measurement was made between 55 K and 300 K at ~ 1 K intervals. A Verwey transition temperature of 108 K was determined, indicating that the crystal is sub-stoichiometric

but it is likely to induce segregation of impurities from the bulk or, in the case of thin films, from the substrate, as reported by Anderson *et al.* [86] and Voogt [59]. Annealing in an oxygen partial pressure is another common technique used [87]. The methods used to clean the surface in this study are the following:

- annealing in UHV at various temperatures
- argon ion sputtering and annealing in UHV
- annealing in an O₂ partial pressure followed by argon sputtering and by further annealing in UHV

Occasionally the crystals were mechanically polished. A detailed description of these procedures will be given in the next sections.

5.2 Mechanical polishing

As found by Seoighe [24], the surface of the Fe₃O₄(001) crystals polished with a chemo-mechanical method by RTI GmbH [82] did not exhibit a regular structure even after long annealing sessions at various temperatures. These crystals were then taken out of the UHV chamber and were mechanically polished. The batch of crystals prepared by SPL [83] did not present this problem since they were polished by a merely mechanical method. However, these crystals were also mechanically polished by the author after long annealing sessions in UHV at high temperatures (~ 1000 K). This treatment, which usually resulted in a highly contaminated surface, was also thought to induce a reduction of the surface from Fe₃O₄ to FeO. The crystals were removed to atmosphere and mechanically polished to remove this surface layer. A brief description of the mechanical polishing method is given below.

The crystal is mounted onto a home-built polishing device [24] using bees wax. Diamond paste is put on a polishing cloth, which is glued to a flat stainless steel disc. The mechanical polishing is done by hand using isopropanol as a lubricant. The crystal is mechanically polished using diamond paste with decreasing grain sizes of 3, 1 and 0.25 μm for approximately one hour for each diamond paste grade. After polishing the crystal is removed from the polishing device and cleaned in an ultrasonic bath using ethanol. It is then screwed onto a Mo sample holder and inserted in the UHV system.

5.3 Annealing in UHV

The preparation method used by Seoighe [24] consisted of mechanically polishing the surface of a $\text{Fe}_3\text{O}_4(001)$ crystal followed by annealing in UHV. Seoighe found that annealing the crystals in UHV to a temperature of $990 \text{ K} \pm 50 \text{ K}$ produced a regularly structured surface. He distinguished between two regimens which give rise to two different types of surface structure. Annealing the crystal to $970 \text{ K} \pm 50 \text{ K}$ for periods ranging from 4 to 8 hours produced a surface characterized by the presence of flat square terraces up to several hundred Ångstrom wide. The edges of these terraces are aligned along the $\langle 110 \rangle$ directions and the step heights between the terraces are multiples of 2.1 Å. This type of structure was imaged by Seoighe on both an artificial crystal (taken from the same ingot as those as the ones used by the author) and a natural crystal. A $p(1 \times 1)$ LEED pattern was obtained from this structure. A further ~ 20 hours annealing at the same temperature induced the formation of a different surface structure. The square terraces seem to split into rows running along the $\langle 110 \rangle$ directions. The splitting appears to start from the edges of the square terraces to proceed inward.

The separation between the rows varies between 40 and 24 Å and it becomes narrower with increasing overall anneal time. The corrugation perpendicular to the rows was measured to be 2.0 ± 0.4 Å, corresponding to the step height between two adjacent terraces. For this reason Seoighe refers to these rows as "nanoterraces". This structure was associated with a LEED pattern in which the primary spots were streaked along the $\langle 110 \rangle$ directions. Occasionally satellite spots were discerned around the primary spots in the $\langle 110 \rangle$ directions. The satellite spots were approximately 1/4 of the primary spot distance, suggesting a repeat structure of ~ 24 Å. This type of structure was also imaged on both an artificial and a natural crystal. However, the images acquired on the natural crystal show a sharper and more regular structure than for the artificial one. The rows were very persistent and were only removed by mechanically polishing the crystal surface. A four grid LEED-optics was used as a retarding field analyser for AES. This system was found to be unsatisfactory since the electronics unit which comprises the preamplifier and oscillator was poorly designed [12]. However, a qualitative Auger analysis was performed by Seoighe to establish if the crystal surface contained contaminants. The presence of sulphur was detected on the natural crystal after annealing in UHV. However this was not found in the case of the artificial crystal. The possibility that the splitting of square terraces into rows was a contaminant-driven effect was ruled out. The conclusion drawn by Seoighe was that the preparation procedure described above produced a clean magnetite surface. It was concluded that the surface of magnetite has a stability transition point at a temperature (in UHV) close to 970 ± 50 K. The structure of the surface after this transition would be a combination of tetrahedral and octahedral planes. In other words, the structure formed by square terraces would be a semi-stable structure. Only after longer annealing

the terraces split into rows to form a more thermodynamically stable state.

One of the first aims of this study was to reproduce the results obtained by Seoighe and to perform a comprehensive AES analysis using a cylindrical mirror analyzer. A set of $\text{Fe}_3\text{O}_4(001)$ crystals, obtained from the same nugget as the crystals used by Seoighe, were prepared by SPL [83]. Experiments were also carried out using one of the crystals originally studied by Seoighe – labelled crystal "number 1". The first experiments carried out by the author using AES, LEED and STM, showed significant deviation from the results obtained by Seoighe. The surface did not seem to structure following the pattern indicated by Seoighe. A few times rounded terraces were observed. Square terraces were seen but they seemed to be much more persistent than expected. Long annealing in UHV failed to produce the splitting of square terraces into rows. On the contrary, long annealing sessions in UHV gave rise to a very poorly structured surface.

These topographic results were accompanied by the chemical analysis of the surface. AES spectra indicated the presence of contaminants like sulphur, carbon, calcium and potassium on the surface. Figure 5.3 shows a typical Auger spectrum obtained after the crystal was annealed to 990 ± 50 K for a total of 36 hours. Only on two occasions were rows similar to the ones seen by Seoighe observed.

Such a large difference in the surface structure and the heavy presence of contaminants could be ascribed to a different annealing temperature. At the beginning of this work, the tungsten filament of the resistive heater used to anneal the magnetite samples broke. It was then plausible to hypothesize that the temperature at the crystal surface was higher than before. To check this possibility a crystal was mechanically polished and inserted in the UHV system. The annealing temperature was increased in steps. After annealing the

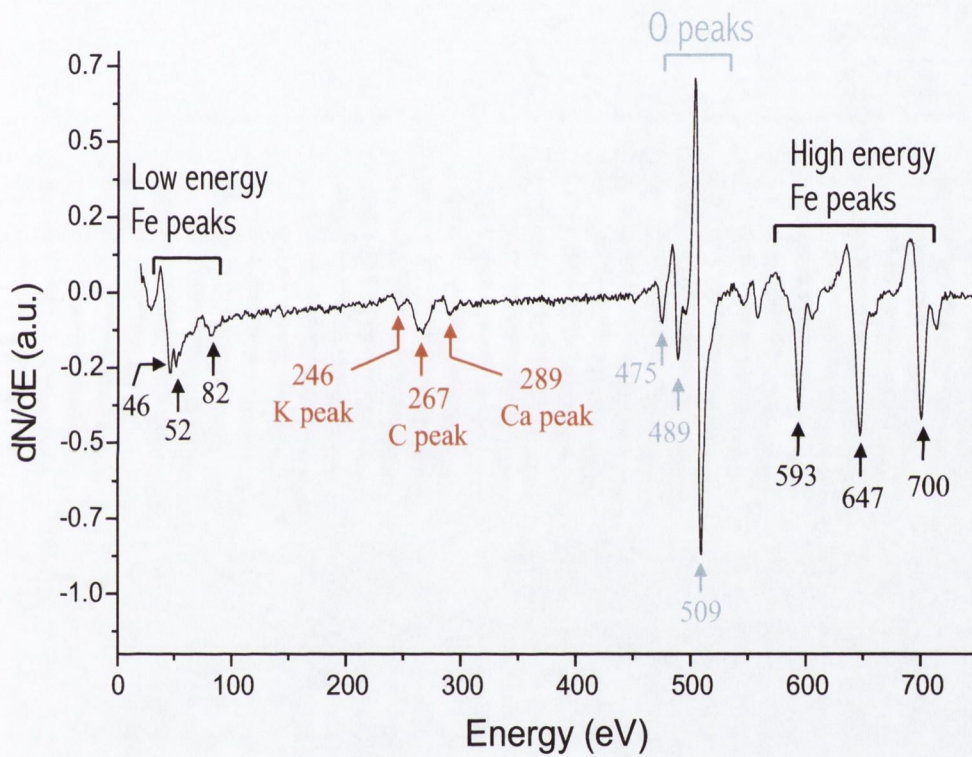


Figure 5.3: Auger spectrum after UHV annealing at 990 ± 50 K for a total of 36 hours. The presence of potassium, carbon and calcium is indicated by the red arrows.

crystal at 940 ± 50 K for ten hours the first LEED pattern was observed; the surface did not show any regular topographic feature. After a further annealing at 990 ± 50 K for ten hours a surface characterized by flat terraces with very irregular edges was imaged by STM. The step height between adjacent terraces is ~ 2 Å. The temperature at which these images were acquired is, within the experimental error, the same as used by Seoighe. Further annealing at higher temperatures induced a heavier contamination of the surface. In this experiment we covered a range of annealing temperatures broader than the one in Seoighe's studies. The hypothesis of a different annealing temperature between the author's experiments and Seoighe's experiments was then rejected.

In conclusion, annealing a magnetite crystal in UHV to temperatures in the surrounding of 1000 K induces a significant contamination of the surface; the contaminants are principally K and Ca that most likely segregate from the bulk of the crystals. Long annealing sessions in UHV at high temperatures are also prone to cause a reduction of the magnetite surface. To produce a clean surface of magnetite a different preparation method is required.

5.4 Ar⁺ ion sputtering and annealing

After repeated attempts to clean the crystal surface by mechanical polishing and annealing in UHV at various temperatures, it was clear that this method was inadequate. AES measurements showed the presence of carbon and occasionally sulphur after the crystal was polished and inserted into UHV (see fig. 5.4). While the carbon peak disappeared after repeated annealing cycles, the sulphur peak was harder to remove. Additionally, the presence of calcium and potassium was detected. These elements are thought to segregate from the bulk as a consequence of the high annealing temperature. Calcium and potassium were detected even after short annealing cycles (~ 4 hours) at 990 ± 50 K. Annealing the crystal for longer periods caused an increase in the concentration of calcium and potassium.

It was then decided to sputter the surface using Ar⁺ ions (see table 5.1 for the details of sputtering conditions). The crystal was sputtered at room temperature and then annealed in UHV at 990 ± 50 K for a short time (of the order of one-two hours). This method was found to produce a clean surface. LEED examination of the surface showed very sharp and defined diffraction spots as well as very blurry patterns, according to different preparation sessions. We attribute this result to the destructive nature of ion sputtering. Although the sputtering and annealing parameters were the same, conditions such as the crystal position and the angle between the ion beam and

Ion energy (keV)	Target current (μ A)	Etching time (min.)
1 – 2	5 – 30	10 – 120

Table 5.1: Typical parameters for Ar⁺ ion etching of a Fe₃O₄(001) surface. A 1×10^{-6} Torr partial pressure of argon gas was used to sputter the surface.

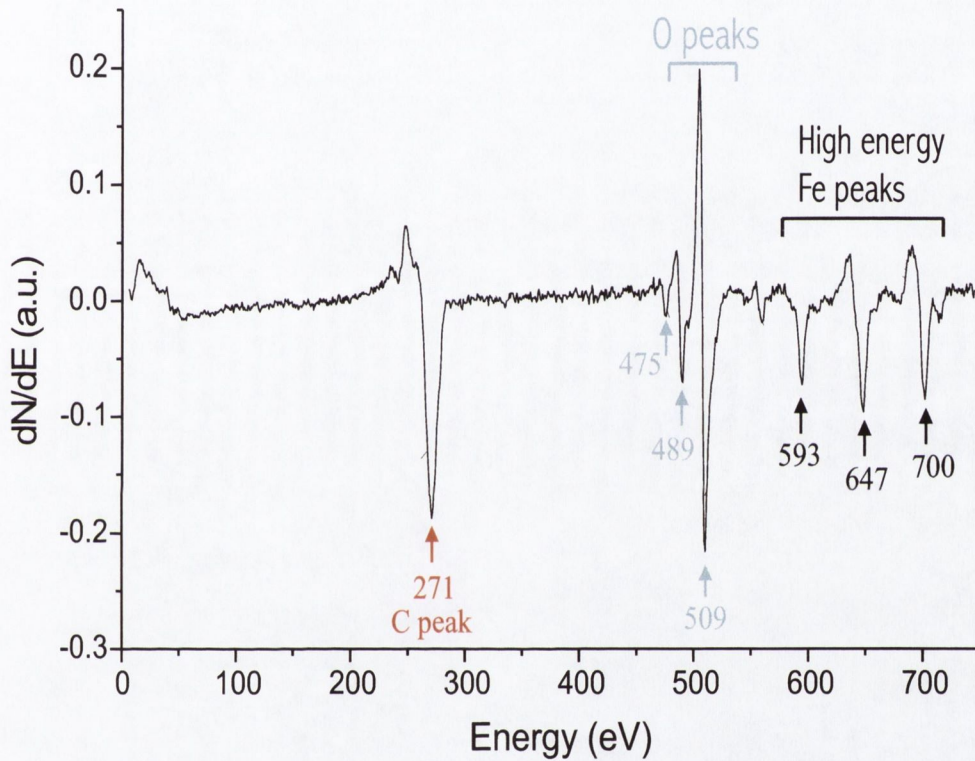


Figure 5.4: Auger spectrum after mechanical polishing. The crystal was not annealed. The presence of a large carbon peak is indicated by the red arrow. Sulphur, occasionally detected after mechanical polishing of the surface, is not present in this spectrum.

the crystal surface were very awkward to control. This is likely to change the amount of material removed from the surface and as a consequence the annealing time required to structure the surface. STM data associated with this preparation procedure showed a surface characterized by square terraces. A variation of the method described above gave rise to a very reproducible method to prepare a contaminant-free surface. The diffraction patterns observed in this case always showed a very sharp $(\sqrt{2} \times \sqrt{2})R45^\circ$ reconstruction as predicted for a clean surface of $\text{Fe}_3\text{O}_4(001)$ [59, 70–75]. The crystal was at first annealed in UHV at high temperature (~ 1030 K) for periods of time ranging between 20 and 120 hours. In this way bulk impurities diffuse to the surface. Fig. 5.5 shows an Auger spectrum taken after annealing a crystal in UHV at 1030 ± 50 K for ~ 20 hours; a calcium peak is present at 290 eV. The crystal was then annealed at 990 ± 50 K in oxygen atmosphere (the exposure ranged between 3600 L and 7200 L). After the pressure recovered the crystal was sputtered with Ar^+ ions (a 1×10^{-6} Torr partial pressure was used). The parameters used for Ar^+ ion etching the surface are shown in table 5.1. As shown by the Auger spectrum in fig. 5.6, calcium has been removed from the surface. Traces of argon and nitrogen are now visible. To remove these impurities, and to let the surface re-structure after the sputtering, the crystal was annealed in UHV for periods of time ranging from two to ten hours. Subsequent AES analysis indicated a clean surface (see fig. 5.7). The

Pre-UHV annealing time (hours)	O_2 exposure (L)	Ar^+ target current (μA)	UHV annealing time (hours)
20 – 120	3600 – 7200	~ 5	2 – 10

Table 5.2: Typical parameters for the preparation of a $\text{Fe}_3\text{O}_4(001)$ surface.

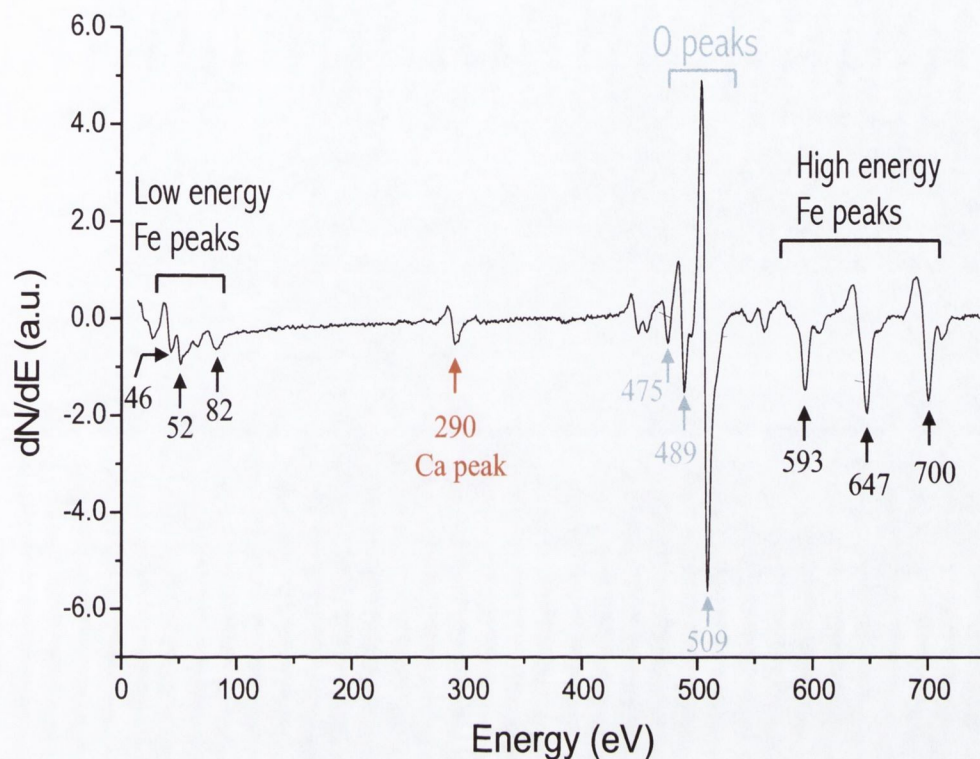


Figure 5.5: Auger spectrum after annealing in UHV at 1030 ± 50 K for ~ 20 hours. The presence of a calcium peak is indicated by the red arrow.

parameters used for this preparation procedure are shown in table 5.2.

To summarize, this preparation method produced a contaminant-free (as shown by AES), $(\sqrt{2} \times \sqrt{2})R45^\circ$ reconstructed (as shown by LEED and STM) surface. This procedure is believed to give rise to a clean magnetite surface.

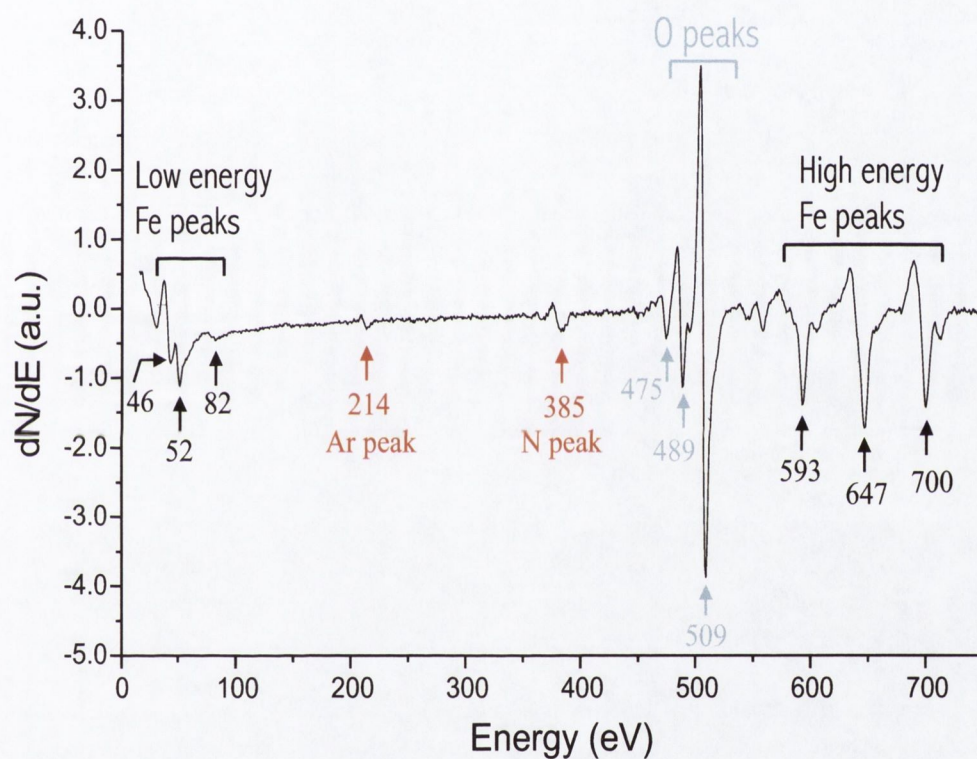


Figure 5.6: Auger spectrum after Ar^+ ion sputtering. Traces of argon and nitrogen are present on the surface.

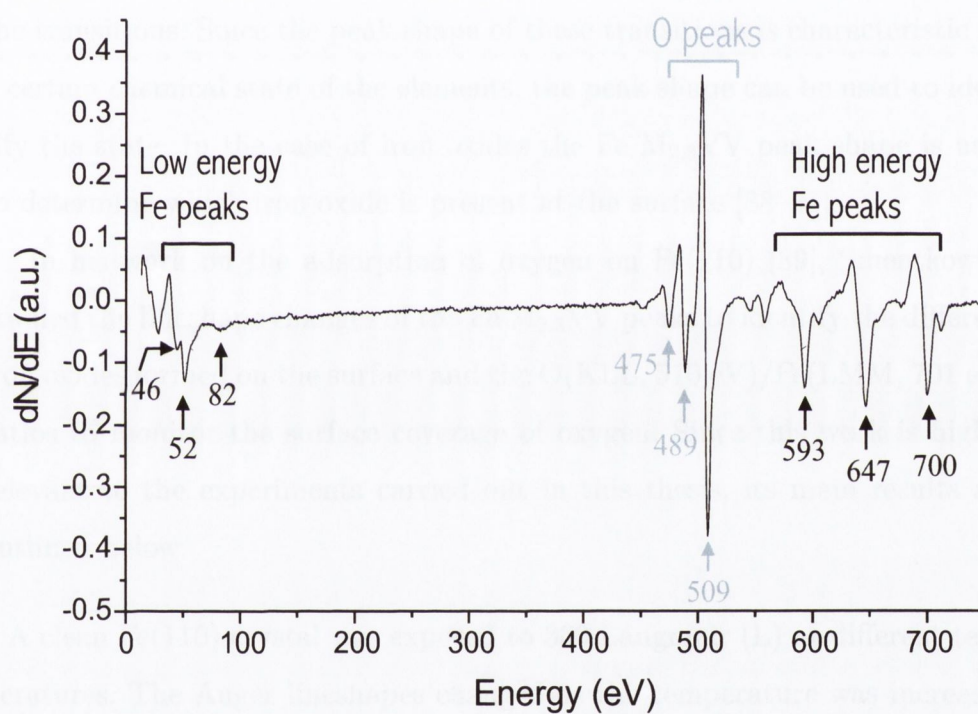


Figure 5.7: Auger spectrum after annealing in UHV at 990 ± 50 K for ~ 2 hours following the Ar^+ ion sputtering.

5.5 AES analysis

A model 10–155A Physical Electronics cylindrical mirror analyser was used for AES analysis of $\text{Fe}_3\text{O}_4(001)$ samples. AES was used during this work to obtain qualitative information about the cleanliness of the crystal surface.

Peak shape changes of Auger transitions are due to changes in the chemical composition and are usually due to valence band electrons involved in the transitions. Since the peak shape of these transitions is characteristic for a certain chemical state of the elements, the peak shape can be used to identify the state. In the case of iron oxides the Fe $M_{2,3}VV$ peak shape is used to determine which iron oxide is present at the surface [88–91].

In his work on the adsorption of oxygen on Fe(110) [89], Smentkowski studied the lineshape changes of the Fe $M_{2,3}VV$ peaks to identify the different iron oxides formed on the surface and the O(KLL, 510 eV)/Fe(LMM, 701 eV) ratios to monitor the surface coverage of oxygen. Since this work is highly relevant to the experiments carried out in this thesis, its main results are outlined below.

- A clean Fe(110) crystal was exposed to 360 Langmuir (L) at different temperatures. The Auger lineshapes changed as the temperature was increased from 90 K to 850 K. By comparing the AES spectra taken at different temperatures with the reference Auger spectra (shown in Fig. 5.8) of FeO, Fe_3O_4 and Fe_2O_3 , it's possible to identify the different phases. The spectrum obtained at 161 K can be assigned to Fe_3O_4 . For oxygen adsorption between 300 K and 575 K the spectrum is associated with Fe_2O_3 . At 600 K the stable oxide is Fe_3O_4 again. For temperatures greater than 840 K FeO is the stable iron oxide (see Fig. 3.2).
- AES was used to monitor the surface concentration of oxygen as a function

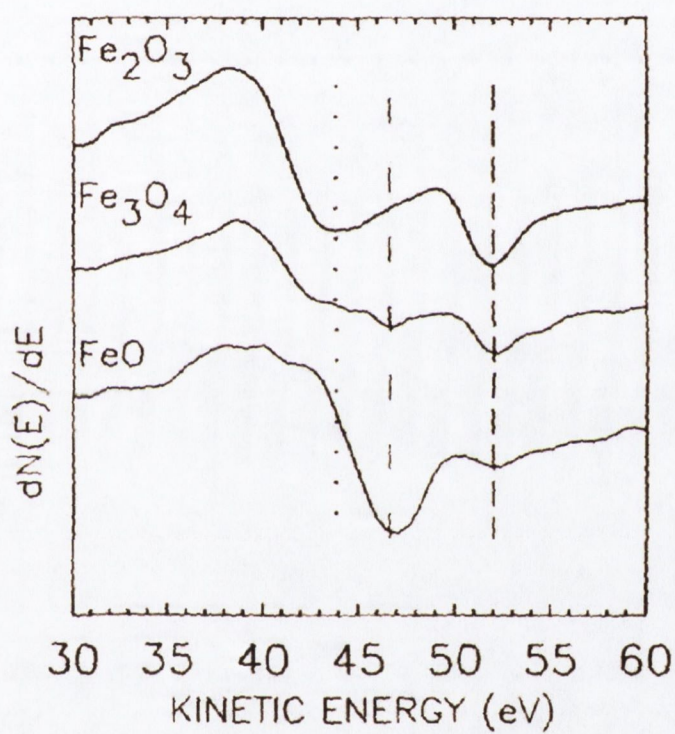


Figure 5.8: Reference Auger spectra of FeO, Fe₃O₄ and Fe₂O₃. Reproduced from [89].

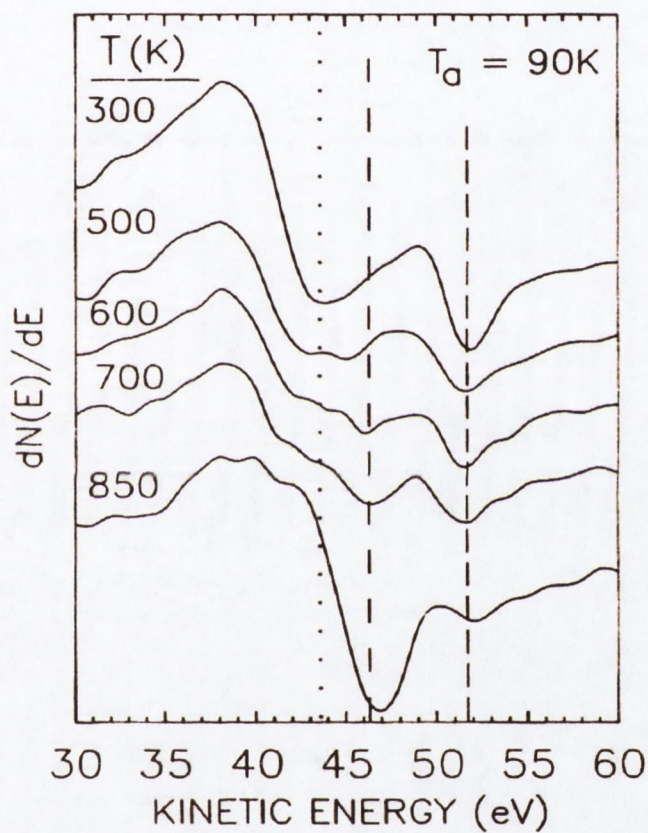


Figure 5.9: Fe(MVV) Auger lineshape changes following the adsorption of 360 L of O_2 at various temperatures. Reproduced from [89].

of surface temperature. A Fe_3O_4 layer was produced and then the crystal was heated to the desired temperature while an Auger spectrum was acquired. From the lineshape changes and the O/Fe Auger ratio it can be shown that between 50 K and 650 K Fe_3O_4 is the stable oxide. In the temperature range of ~ 650 – 950 K, the O/Fe Auger ratio decreases as a result of the Fe_3O_4 to FeO transition. Above 950 K, the O/Fe Auger ratio remains constant since FeO is the only stable surface oxide.

- A Fe_3O_4 layer was produced on the crystal which was then heated and maintained at the desired temperature while Auger spectra were periodically acquired. At a temperature of 575 K no thermal effect is observed and the Fe_3O_4 layer is stable. At 600 K, the O/Fe Auger ratio remained constant at 1.41 for ~ 30 min. It then started to decrease as iron diffusion through the Fe_3O_4 layer occurred. At 700 K, which corresponds to a temperature slightly higher than than the starting temperature of the Fe_3O_4 to FeO phase transition (~ 670 K), the Auger O/Fe ratio started to decrease immediately and saturated to 0.54 after ~ 80 min. At 800 K, the experiment was performed at a temperature near the completion of the Fe_3O_4 to FeO phase transition; as a result, the initial value of the O/Fe Auger ratio is low and rapidly reaches its limiting value of 0.54.

Since the electron beam of the Auger spectrometer is potentially capable of modifying the oxygen covered surface, controlled electron bombardment experiments were performed by Smentkowsky at both 90 K and 300 K. The crystal, containing ~ 1 ML of oxygen, was exposed to the Auger electron beam (*current density* = $12.5 \mu\text{A}/\text{cm}^2$, $V_e = 3$ kV) for two hours. The Auger spectra, obtained at ~ 30 min. time intervals, did not change in intensity or shape, indicating that electron beams effects were not occurring under such preparation conditions. Since the high en-

ergy O(KLL, 510 eV)/Fe(LMM, 701 eV) ratios are used to monitor the surface coverage of oxygen, it was also necessary to demonstrate that lineshape changes do not occur, for the different iron oxides, in the high energy region of the Auger spectra. Once again this was found to be true and so the O(KLL, 510 eV)/Fe(LMM, 701 eV) ratios could be correlated with the surface coverage of oxygen.

Figure 3.2 shows the phase diagram of the Fe-O system. This is a complex system where the stable phases depend on parameters such as temperature and oxygen content. The preparation of a Fe_3O_4 single crystal is therefore of critical importance to obtain a surface layer that is truly magnetite and not a different phase such as hematite or wüstite. A series of experiments was carried out to establish whether or not it was possible to obtain quantitative information from our Auger spectra. An artificial $\text{Fe}_3\text{O}_4(001)$ crystal was exposed to 2160 L of oxygen and at the same time it was annealed at a temperature of 990 ± 50 K. About two hours were allowed for the crystal to cool down and the pressure to recover. The crystal was then transferred into the sample stage and five Auger spectra were acquired at ~ 40 minute time intervals. The acquisition time of one spectrum was ~ 12 minutes. The crystal was continuously exposed to the electron beam of the Auger spectrometer for all the duration of the experiment. The emission current and the beam voltage were respectively $I_{\text{emission}} = 1.4$ mA (corresponding to a target current of $I_{\text{target}} \sim 14 \mu\text{A}$) and $V_e = 3$ keV.

The Fe(MVV) transitions are shown in Fig. 5.10. It is obvious from this picture that the shape of the low energy iron peaks changes dramatically as a function of time. The first spectrum, acquired at $t = 0$ min., shows two minima at 44.5 eV and 51.5 eV. In the second spectrum, recorded 40 minutes later, the second peak is still at an energy of 51.5 eV while the first

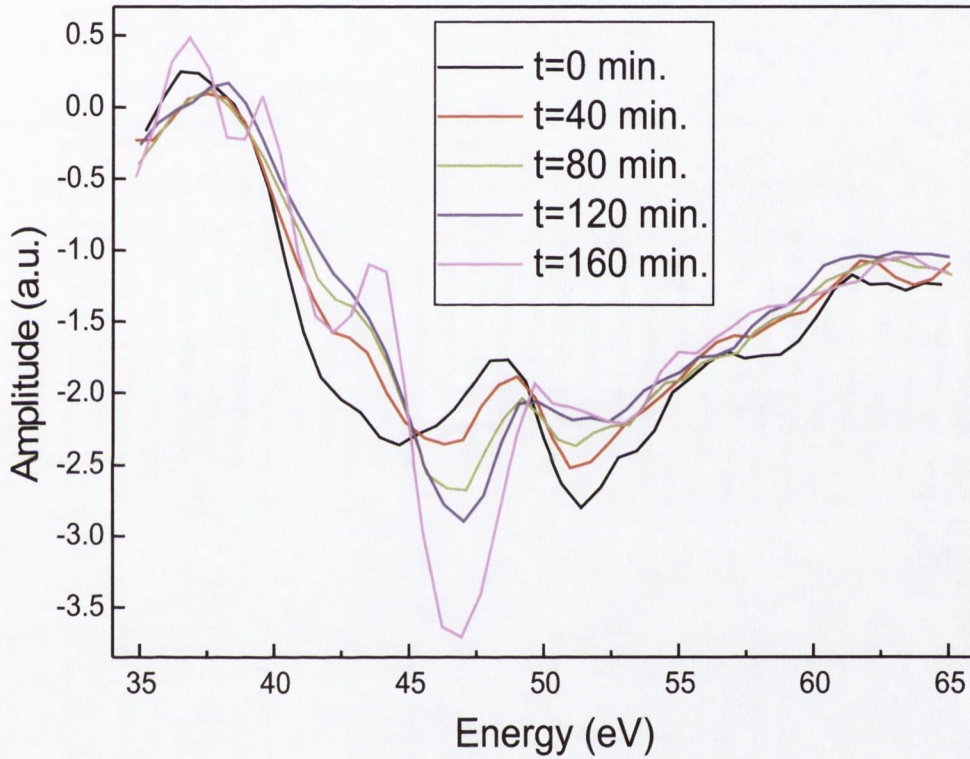


Figure 5.10: Auger spectra of a Fe_3O_4 single crystal taken at 40 min. intervals. The shape and the relative amplitude of the peaks change as a function of time.

peak shifts to 46 eV. At the same time, the amplitude of the second peak starts to decrease. In the third spectrum, acquired at $t = 80$ min., the first peak corresponds to 46.5 eV and the second one is still stable at 51.5 eV. At this time the low energy peak becomes bigger than the high energy one. This trend is confirmed by the last two spectra acquired at $t = 120$ min. and $t = 160$ min. respectively.

The lineshape change in the Fe(MVV) transitions is accompanied by a change in the oxygen concentration as shown by the decrease of the O(509 eV) peak amplitudes (see Fig. 5.11). There is a direct correlation between the oxygen content detected on the surface and the time the crystal was exposed to the electron beam. The high energy Fe(649 eV, 701 eV) peaks were also analysed. They do not show any significant change, neither in their shape nor in their amplitude. The O/Fe ratio, measured using the O(509 eV) peak and the Fe(701 eV) peak, decreases as the exposure time of the crystal increases.

Although the experimental parameters (target current and beam voltage) are similar to the ones used by Smentkowski, our results indicate that the electron beam of the Auger spectrometer has a significant and deleterious effect on the measurements.

The lineshape change of the Fe(MVV) peaks and the amplitude decrease of the O(509 eV) peak can be caused by the electron beam heating up the crystal surface causing an electron stimulated desorption (ESD) of oxygen. As stated above, since the amplitude of the Fe(701 eV) does not change with time, the O(509 eV)/Fe(701 eV) ratio decreases with time; this implies that the surface of the crystal is depleted of oxygen during the exposure to the electron beam. This indicates a reduction of the surface from a higher oxygen content (like hematite) to a lower oxygen content (like wüstite). This

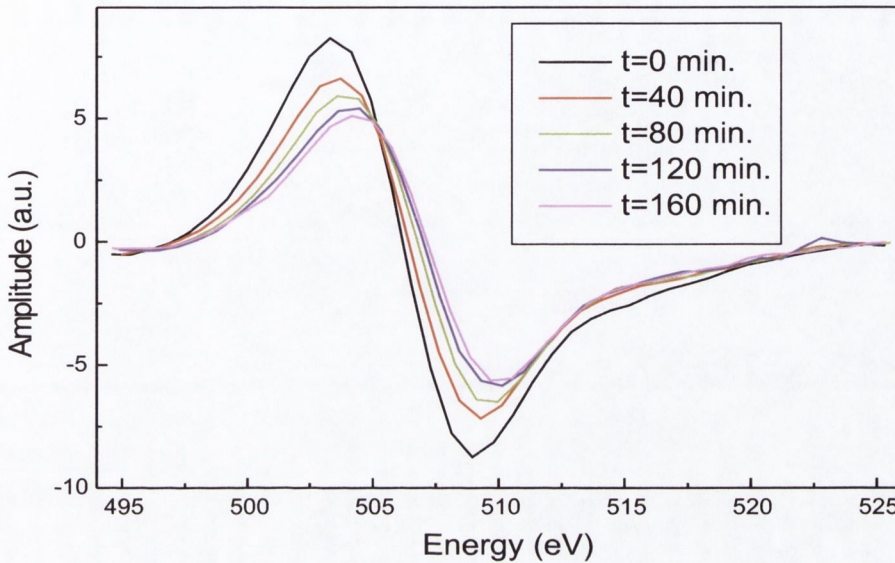


Figure 5.11: Auger spectra of a Fe_3O_4 single crystal taken at 40 min. intervals. The amplitude of the O(509 eV) peaks decreases as a function of time.

explanation is in agreement with the changes observed in the Fe(MVV) peaks. Comparing these peaks with the reference Auger spectra reproduced from [89] and shown in Fig. 5.8, it's possible to identify the spectrum taken at $t = 0$ min. with Fe_2O_3 , the spectrum taken at $t = 40$ min. with Fe_3O_4 and the one taken at $t = 160$ min. with FeO. The other spectra correspond to a transition between Fe_3O_4 and FeO. The shift of the low energy iron peak from 44.5 eV to 47 eV corresponds to a shift to a more metallic state, 47 eV being the transition energy corresponding to metallic iron. Such an effect would be localised in the area of the crystal hit by the electron beam. This was found to be the case. The diameter of the e^- -beam is $\sim 100 \mu\text{m}$. Right after the set of measurements shown in Fig. 5.10, the crystal was moved by ~ 2 mm and an Auger spectrum was acquired. The shape of the Fe(MVV) peaks corresponds to the one shown in Fig. 5.10 taken at $t = 0$ min.

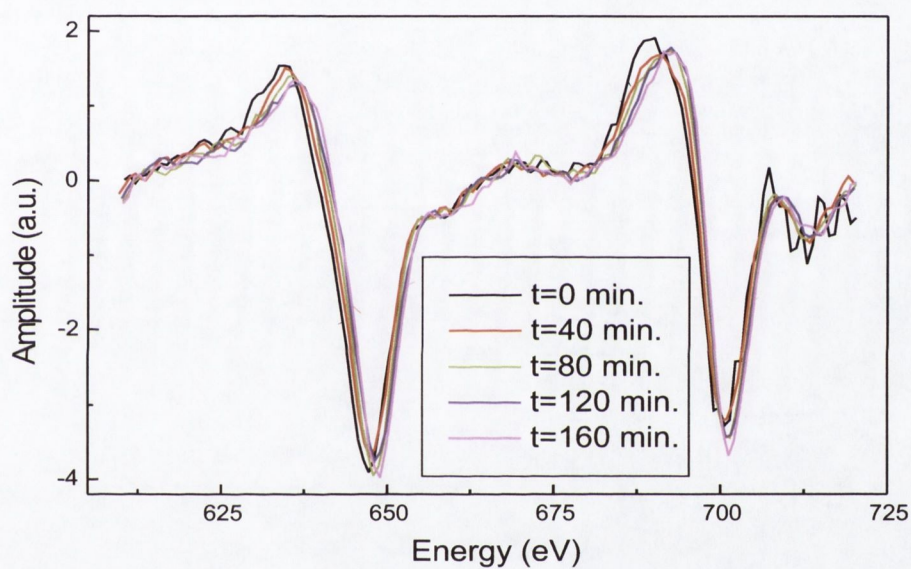


Figure 5.12: Auger spectra of a Fe_3O_4 single crystal taken at 40 min. intervals. The shape and the relative amplitude of the Fe(649 eV, 701 eV) peaks do not change as a function of time.

In a different set of experiments, the crystal was annealed in UHV for ~ 100 hours to a temperature of $950 \text{ K} \pm 50 \text{ K}$. Such a long annealing in UHV is likely to cause a reduction of the magnetite surface to FeO and to cause segregation of impurities from the bulk. Also in this case the primary beam spot was fixed at one position on the surface, while Auger spectra were taken repeatedly. Figure 5.13 shows four spectra taken at $t = 0$, $t = 16$, $t = 19$ and $t = 28$ minutes respectively. All the four spectra exhibit a large peak at 46 eV, while the peak at 51 eV is only visible in the spectrum taken at $t = 0$ min. (Note that the amplitude of this spectrum is bigger than the others since it was acquired using a $20 \mu\text{V}$ sensitivity instead of $50 \mu\text{V}$). The shape of these spectra corresponds to FeO, as shown in the reference Auger spectra (Fig. 5.8). The spectra taken at $t = 16$, 19 and 28 min. are practically identical so that it is almost impossible to distinguish one from the other. This can be understood assuming that a stable FeO layer is present on the surface and that ESD is not significant any more.

From the two sets of experiments described above we can conclude that the electron beam of the Auger spectrometer plays a crucial role during the acquisition of the Auger spectra when the surface of the crystal is not reduced to FeO. The e^- -beam induces an electron stimulated desorption of oxygen from the surface until an FeO-like state is reached. When this happens, an equilibrium is reached and the lineshape of the Fe(MVV) does not change any more. Obviously this fact does not allow us to use the Auger data for a quantitative analysis. An attempt to solve this problem was made by decreasing the target current I_{target} from $14 \mu\text{A}$ to $2 \mu\text{A}$. Although the situation improved, an electron beam effect was still observed. This fact makes it very questionable to compare Auger spectra obtained during different sessions, since the time of exposure to the electron beam can vary significantly

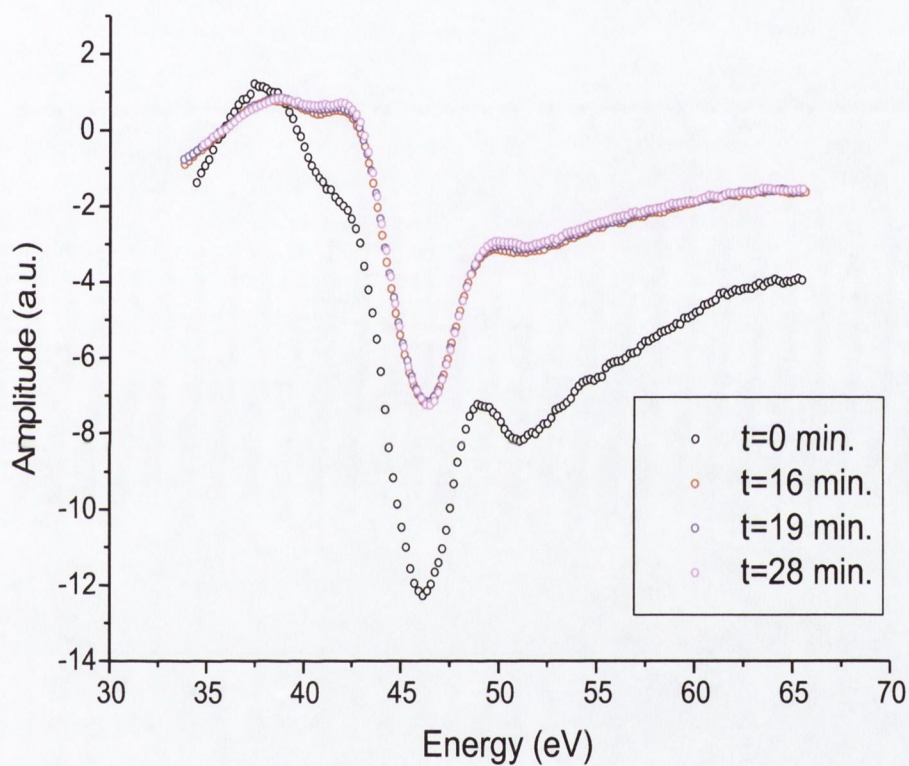


Figure 5.13: Auger spectra of a Fe_3O_4 single crystal annealed in UHV to a $950 \text{ K} \pm 50 \text{ K}$ temperature for ~ 100 hours.

from session to session. In addition to these problems, a strong critique to the possibility of identifying the different iron oxide species from the low energy Auger peaks was published by den Daas [92]. In this work the use of derivative spectra for quantitative analysis is judged inadequate and dangerous. According to his work, a change of shape of the original peak also changes the peak-to-peak height in the derivative mode and the correct peak-to-peak heights are difficult to determine. Another problem is that the background in the low energy region (< 100 eV) often changes strongly upon chemical or structural changes of the surface and then it can influence the shape of the complete spectrum. The collection of the integral (N versus E) spectra followed by the removal of the background is suggested as the correct way to proceed.

Since in the literature there is poor agreement concerning the possibility to identify the different iron oxides from the Auger Fe(MVV) peaks lineshape and amplitude, and since the results obtained during this thesis are not of straightforward interpretation, the Auger experiments were limited to a qualitative analysis of the cleanliness of the crystal surface. Given this caution, an indication of the oxidation state of the surface may still be deduced from the very first Auger scan.

Chapter 6

p(1×4) reconstruction on Fe₃O₄(001)

6.1 Introduction

As explained in section 4.2, the (001) surface of magnetite is a *polar* surface. That means its two possible bulk-truncated terminations cannot exist: the Fe₃O₄(001) surface can only occur if the surface reconstructs or if it undergoes a charge redistribution. In this chapter we will discuss a series of results indicating a p(1×4) surface reconstruction driven by segregation of contaminants from the bulk of the crystal.

6.2 Experimental results

A new set of Fe₃O₄(001) single crystals was used for the experiments described in this chapter. These crystals were prepared by Surface Preparation Laboratory [83]. The preparation details are described in section 5.1. After cleaning one of the crystals in an ultrasonic bath using ethanol, it was at-

tached onto a Molybdenum holder by means of a Tantalum screwed-on cap and inserted in the UHV preparation chamber.

6.2.1 First annealing cycle

The crystal was then inserted face down inside the resistive heater and annealed in UHV at 990 ± 50 K for four hours. After an initial rise up to $\sim 5 \times 10^{-9}$ Torr, the pressure stabilised around a value of 5×10^{-10} Torr. Figure 6.1 shows an Auger spectrum taken after the crystal was cooled down. A 3 keV electron beam energy and a 1.4 mA emission current were used. Two peaks at 249 eV and 292 eV show the presence of potassium and calcium, respectively. Other impurities, if present on the surface, were below the detection limit of our AES setup. A LEED image taken right after the AES measurements is shown in fig. 6.2 (a). The distance between the primary spots along the $\langle 110 \rangle$ directions was calculated to be 6.0 ± 1.2 Å, in agreement with the expected value of the magnetite unit cell (see section 2.1.2). Satellite spots are visible along the $[110]$ and $[1\bar{1}0]$ directions around the primary spots. They are $\sim 1/4$ of the primary spots distance, which corresponds to ~ 24 Å in real space. This pattern indicates the onset of a $p(1\times 4)$ reconstruction with domains oriented by 90° with respect to each other. A schematic of such a reconstruction is shown in fig. 6.2 (b). Another point of interest in this image is the presence of very faint spots indicated by red arrows in fig. 6.2 (a). These spots correspond to a $(\sqrt{2} \times \sqrt{2})R45^\circ$ reconstruction.

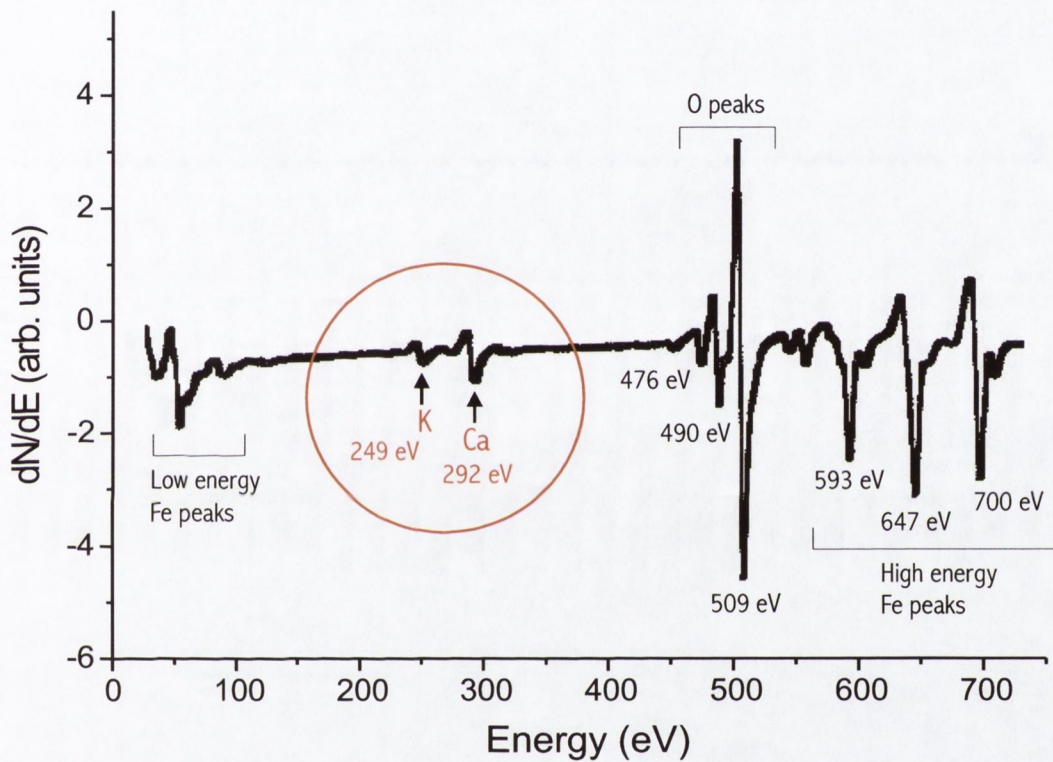


Figure 6.1: First annealing cycle. Auger spectrum of an artificial $\text{Fe}_3\text{O}_4(001)$ single crystal after a 4 hours UHV annealing at 990 ± 50 K. Two peaks at 249 eV and 292 eV show the presence of potassium and calcium on the surface. Ca concentration = 5.4 %, K concentration = 1.9 %.

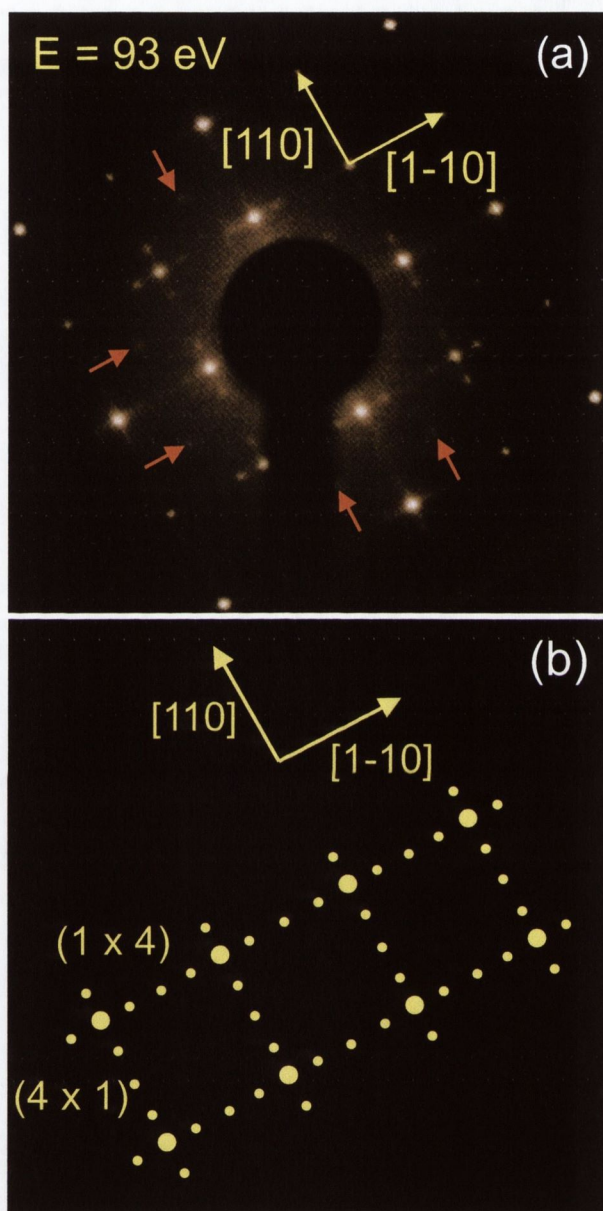


Figure 6.2: (a) First annealing cycle. LEED pattern observed with a primary electron energy of 93 eV. Satellite spots are visible around the primary spots along the $[110]$ and $[1\bar{1}0]$ directions. They are $\sim 1/4$ of the primary spots distance, which corresponds to $\sim 24 \text{ \AA}$ in real space. Faint spots corresponding to a $(\sqrt{2} \times \sqrt{2})R45^\circ$ reconstruction are indicated by red arrows. (b) Schematic of a $p(1 \times 4)$ reconstruction LEED pattern.

STM images were recorded operating in constant-current mode at room temperature. A tungsten tip, prepared as described in section 2.2, was used. Sample bias of 1 V and tunneling current of 0.1 nA were the typical measurement parameters. The surface is characterized by the presence of terraces, as shown in fig. 6.3 (a). The edges of the terraces are mostly well defined and are aligned along the $[110]$ and $[1\bar{1}0]$ directions, although in different areas they are characterized by a more irregular shape (see fig. 6.3 (b)). The terraces are separated by $2.1 \pm 0.2 \text{ \AA}$ or by an integer multiple of this value along the z - direction. This value corresponds to one quarter of the (001) unit cell lattice constant and can be associated either with the distance between two tetrahedrally coordinated planes (A - A planes) or with the distance between two octahedrally coordinated planes (B - B planes). The terraces are covered by rows running along the $[110]$ and $[1\bar{1}0]$ directions and the orientation of the rows changes by 90° on terraces separated by $[2.1 \times (2n + 1)] \text{ \AA}$, where $n = 0, 1, 2, \dots$. An example of the 90° rotation can be seen in fig. 6.4 (b), where the two terraces are separated by $2.1 \pm 0.2 \text{ \AA}$ along the z - direction. The separation between rows varies between 22 and 30 \AA , and the corrugation of the rows measured along the $\langle 110 \rangle$ directions ranges between 1 and 2 \AA .

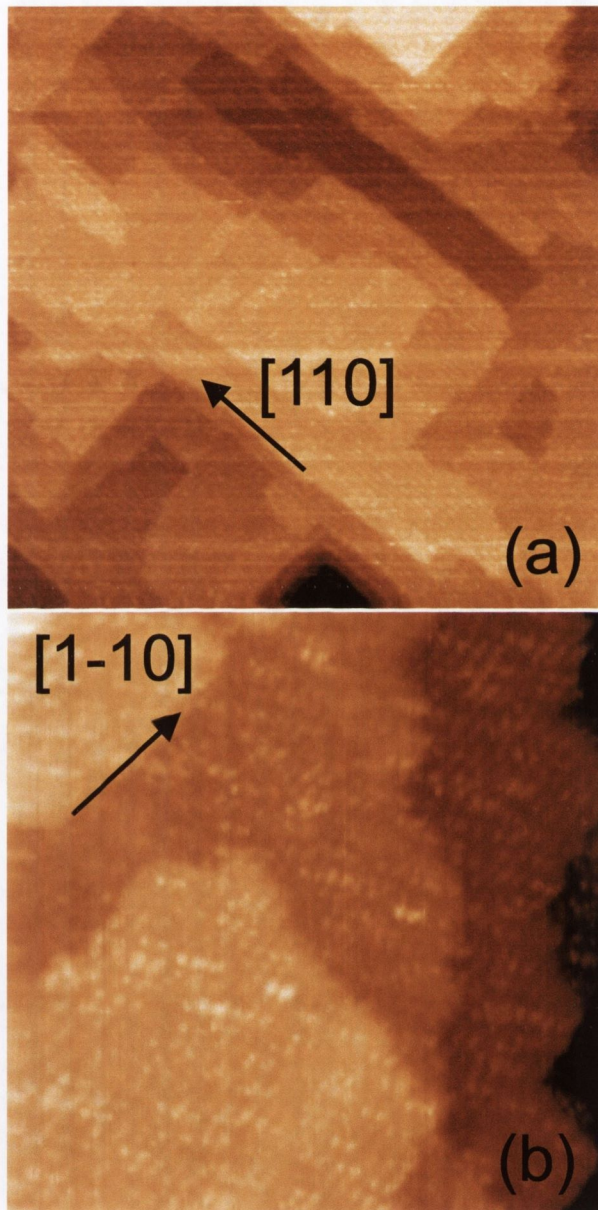


Figure 6.3: (2000×2000) \AA^2 (a) and (800×800) \AA^2 (b) STM image of a $p(1\times 4)$ reconstructed surface of $\text{Fe}_3\text{O}_4(001)$. The irregular shape of the terrace edges can be seen. Both images were acquired at a sample bias of 1.0 V and a tunneling current of 0.1 nA using a W tip.

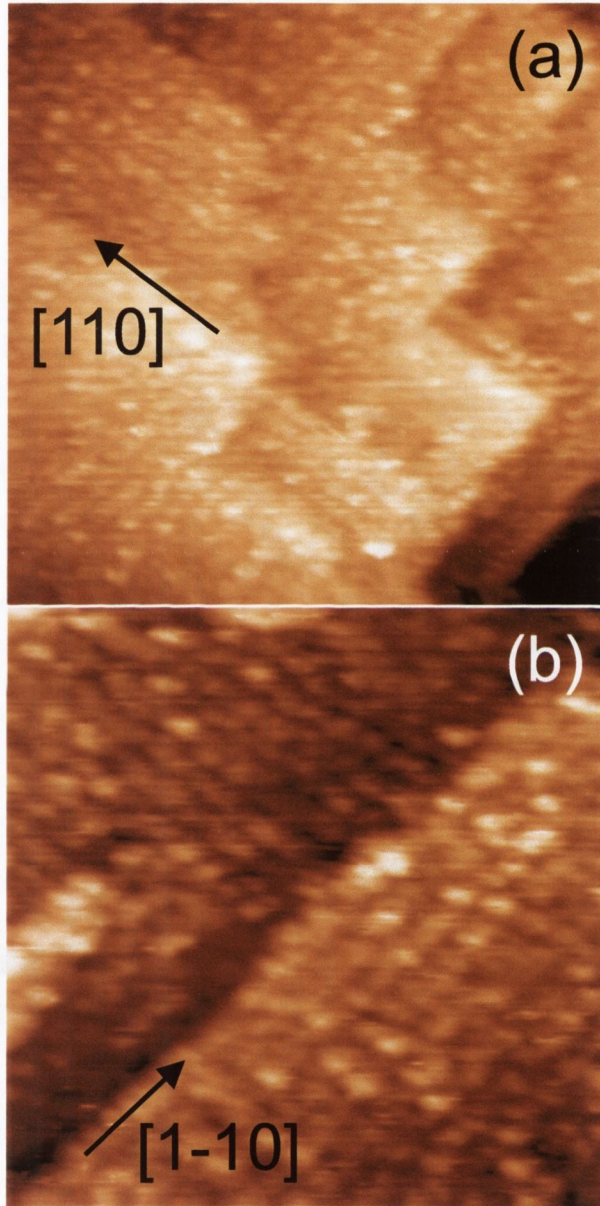


Figure 6.4: $(600 \times 600) \text{ \AA}^2$ (a) and $(400 \times 400) \text{ \AA}^2$ (b) STM image of a $p(1 \times 4)$ reconstructed surface of $\text{Fe}_3\text{O}_4(001)$. Both images were acquired at a sample bias of 1.0 V and a tunneling current of 0.1 nA using a W tip.

Anneal time (hours)	Anneal temp. (K)	K level (%)	Ca level (%)	S level (%)	Fe level (%)	O level (%)
4	990 ± 50	1.9	5.4	–	44	48.7
18	990 ± 50	0.9	6.7	–	48.7	43.7
20	990 ± 50	0.6	7.8	1.0	55.7	34.9
14	1030 ± 50	–	9.5	–	50.1	40.4

Table 6.1: Contamination levels of potassium and calcium after four annealing cycles in UHV at various temperatures.

6.2.2 Second annealing cycle

The crystal was further annealed in UHV for eighteen hours at 990 ± 50 K. Figure 6.5 shows an Auger spectrum taken after the crystal was cooled down. A 3 keV electron beam energy and a 1.4 mA emission current were used. Comparing this spectrum with the previous one (see fig. 6.1) it's clear that the peak at 249 eV, corresponding to potassium, has almost disappeared. On the contrary, the calcium peak at 292 eV has increased. Atomic concentrations calculated as described in section 2.1.3 are shown in table 6.1.

A LEED image taken right after the AES measurements is shown in fig. 6.6. The distance between the primary spots along the $\langle 110 \rangle$ directions was calculated to be $6.0 \pm 1.2 \text{ \AA}$, in agreement with the expected value of the magnetite unit cell. A $(\sqrt{2} \times \sqrt{2})R45^\circ$ mesh is now clearly visible. Satellite spots are still visible along the $[110]$ and $[1\bar{1}0]$ directions around some of the primary spots, but some of them are practically indiscernible from streaked lines running along the $[110]$ and $[1\bar{1}0]$ directions.

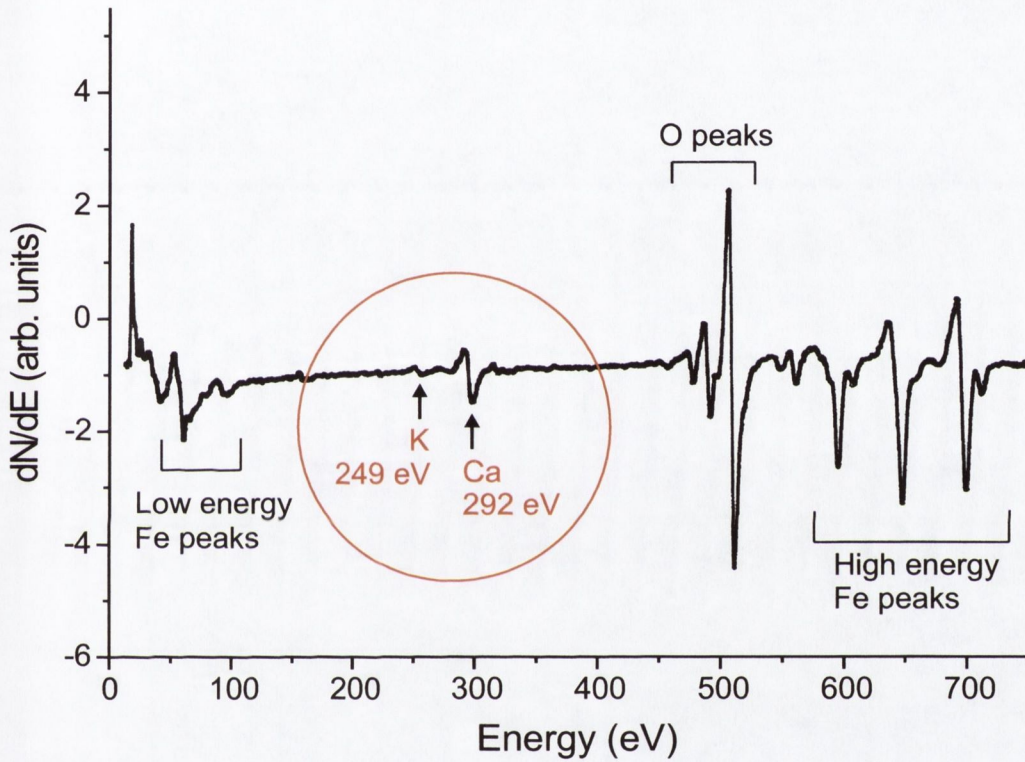


Figure 6.5: Second annealing cycle. Auger spectrum of an artificial $\text{Fe}_3\text{O}_4(001)$ single crystal after a further 18 hours UHV annealing at 990 ± 50 K. The peak at 249 eV, corresponding to potassium, has almost disappeared while the calcium peak at 292 eV has increased. Ca concentration = 6.7 %, K concentration = 0.9 %.

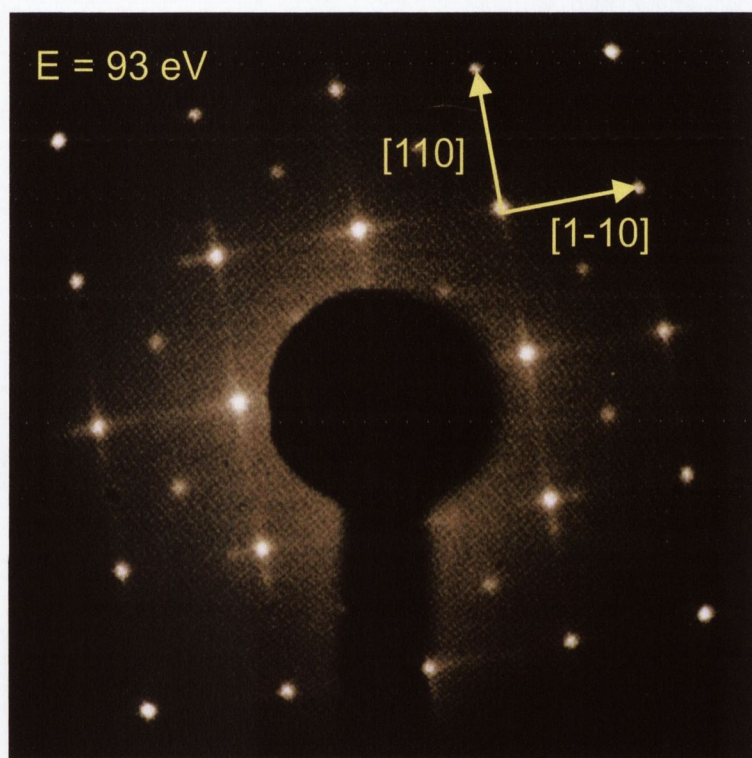


Figure 6.6: LEED pattern observed with a primary electron energy of 93 eV. The artificial $\text{Fe}_3\text{O}_4(001)$ single crystal was annealed in UHV for further 18 hours at $990 \pm 50 \text{ K}$. A $(\sqrt{2} \times \sqrt{2})R45^\circ$ mesh is now clearly visible. Satellite spots are still visible along the $[110]$ and $[1\bar{1}0]$ directions around some of the primary spots, but some of them are practically indiscernible from streaked lines running along the $[110]$ and $[1\bar{1}0]$ directions.

A PtIr tip was used for STM measurements. Figure 6.7 (a) shows a $(2000 \times 2000) \text{ \AA}^2$ image obtained using a +1 V bias voltage and a 0.1 nA tunneling current. This image shows that multiple terraces are present on the surface, with the edges aligned along the $[110]$ and $[1\bar{1}0]$ directions. The terraces can be divided into three different sets, according to the structure observed on top of them. The first set comprises flat terraces, the second set is characterized by terraces with rows aligned along the $[110]$ or $[1\bar{1}0]$ crystallographic axes, and the third set contains terraces with rows aligned at $\approx \pm 60^\circ$ with respect to the $[110]$ direction. A zoom on the area marked by the white dashed square is displayed in fig. 6.7 (b); it shows a $(1000 \times 750) \text{ \AA}^2$ image that helps to better distinguish the three different structures. Terraces labelled as B_1 , B_2 and B_3 are characterized by rows oriented along the $[110]$ direction, while terraces labelled as A_1 and A_2 are flat. The line profile taken along the line labelled $t-t$ and shown in Fig. 6.7 (c), shows a very interesting feature. The step height between terraces B_1 and A_1 is $\sim 1 \text{ \AA}$, and the same distance separates terrace B_2 from terrace A_2 . A 1 \AA separation along the $[001]$ direction corresponds to the distance between two consecutive octahedral and tetrahedral atomic planes in bulk magnetite, and it has never been observed before. Terraces B_1 , B_2 and B_3 are separated by $4.2 \pm 0.4 \text{ \AA}$ and the rows on top of these terraces are oriented along the $[110]$ direction. Terraces A_1 and A_2 are also separated by $4.2 \pm 0.4 \text{ \AA}$, but no rows are visible on top of them. A neighbouring area of the crystal is shown in Fig. 6.8 (a), and the line profile labelled $v-v$ – see Fig. 6.8 (b) – also shows that the step height between terraces B_1 and A_1 is $\sim 1 \text{ \AA}$, while terraces B_1 and B_2 are separated by $4.2 \pm 0.4 \text{ \AA}$. The rows on terraces B_1 and B_2 are regularly spaced and their average periodicity was measured to be $26 \pm 3.0 \text{ \AA}$, while the corrugation of the rows along the $[110]$ direction varies between 1 \AA and 2 \AA . The

area marked by a white oval in Fig. 6.8 (a) shows a $2.1 \pm 0.2 \text{ \AA}$ step height between two terraces with rows rotated by 90° with respect to each other. An other area of interest is the one marked as A_0 . This terrace, separated by $\sim 1 \text{ \AA}$ from terrace B_1 , is characterized by rows forming a $\delta \approx 60^\circ$ angle with the $[110]$ crystallographic axis. The area delimited by the dotted-dashed line in Fig. 6.8 (c) shows a large terrace where domains with rows oriented at a $\pm 60^\circ$ angle with the $[110]$ direction are visible. The periodicity of these rows is $\sim 13 \text{ \AA}$, about half the value of the average periodicity of the rows aligned with the $[110]$ direction on terraces B_1 , B_2 and B_3 . A zoom of the area marked by the dashed rectangle is shown in Fig. 6.8 (d). It can be seen that the domains are separated by rows running along the $[\bar{1}\bar{1}0]$ direction; the angles formed by the rows with the $[110]$ direction are shown.

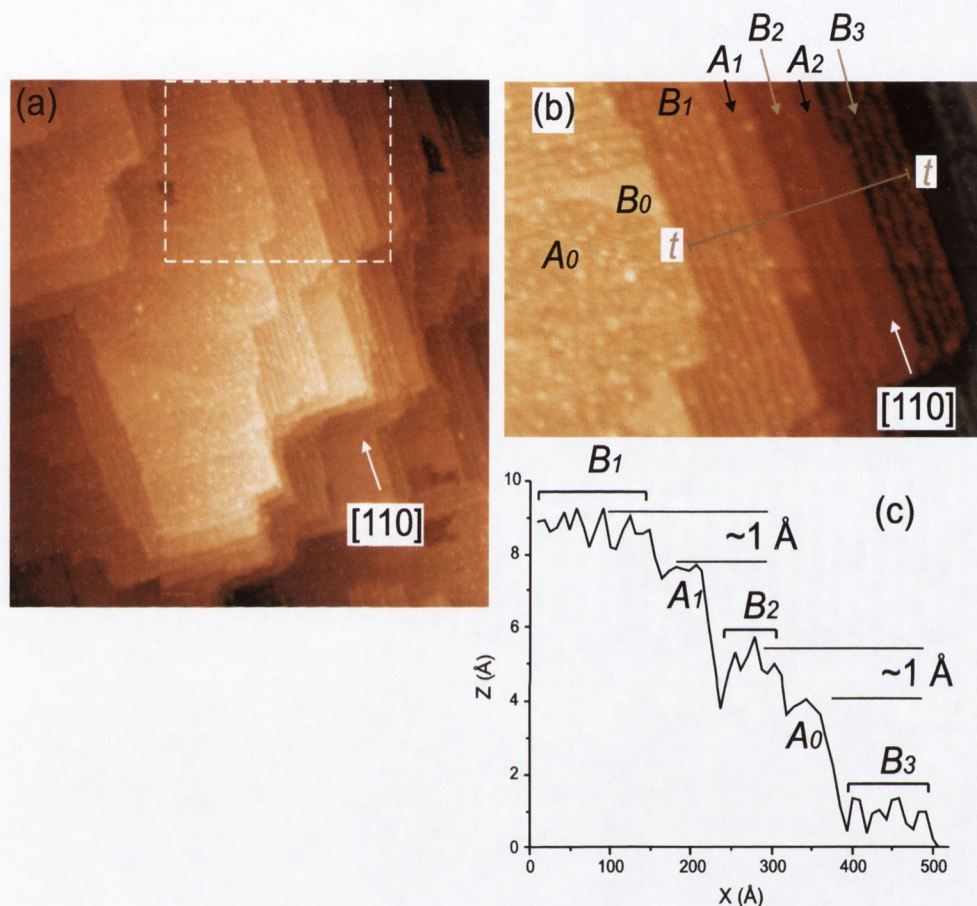


Figure 6.7: (a) $(2000 \times 2000) \text{ \AA}^2$ STM image. The area marked by the white dashed square is displayed in fig. 6.7 (b). Multiple terraces are present on the surface, with the edges aligned along the $[110]$ and $[1\bar{1}0]$ directions. (b) $(1000 \times 750) \text{ \AA}^2$ STM image. Terraces labelled B_1 , B_2 and B_3 are characterized by rows running along the $[110]$ direction, while terraces labelled A_1 and A_2 are flat. (c) Line profile taken along the scan line labelled $t-t$ in fig. 6.7 (b). The step height between terraces B_1 and A_1 and terraces B_2 and A_2 is $\sim 1 \text{ \AA}$. Terraces B_1 , B_2 and B_3 are separated by $4.2 \pm 0.4 \text{ \AA}$.

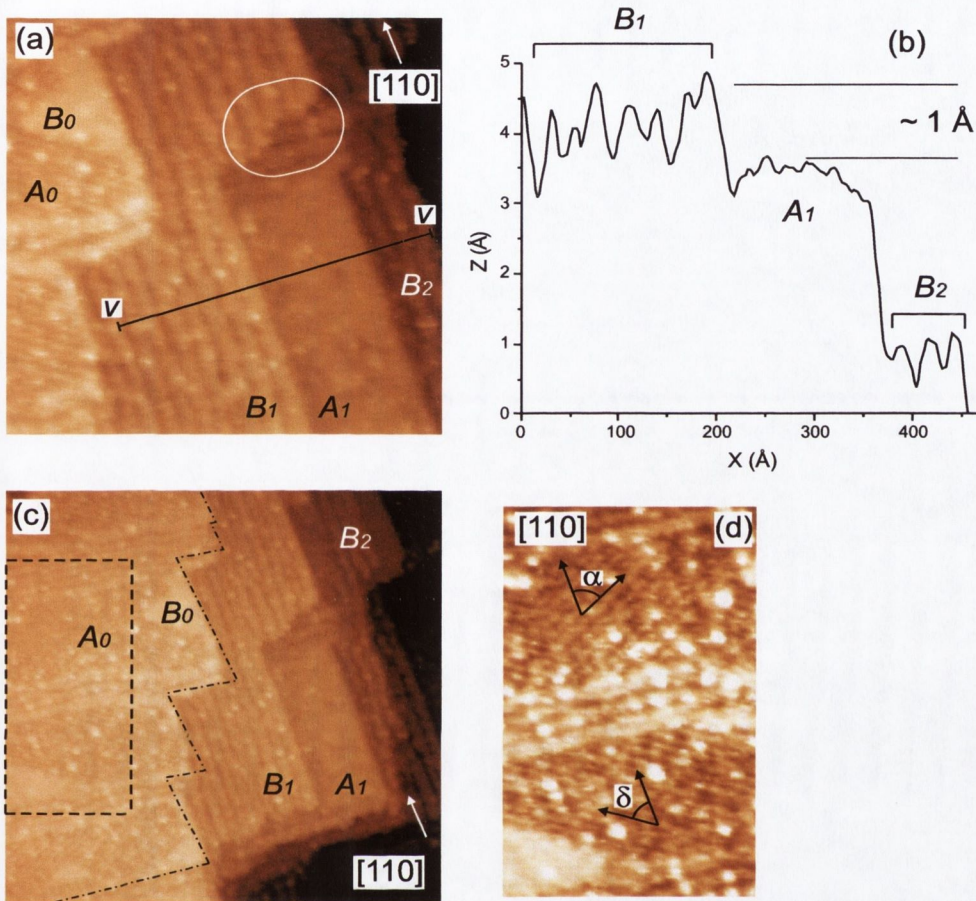


Figure 6.8: (a) $(600 \times 600) \text{ \AA}^2$ STM image. The area marked by a white oval shows a $2.1 \pm 0.2 \text{ \AA}$ step height between two terraces: the rows are rotated by 90° with respect to each other. (b) Line profile taken along the scan line labelled $v-v$ in fig. 6.8 (a). The step height between terraces B_1 and A_1 is $\sim 1 \text{ \AA}$, while terraces B_1 and B_2 are separated by $\sim 4 \text{ \AA}$. (c) $(1000 \times 1000) \text{ \AA}^2$ image. The area delimited by the dotted-dashed line shows a large terrace where domains with rows oriented at a $\pm 60^\circ$ angle with the $[110]$ direction are visible. (d) $(330 \times 530) \text{ \AA}^2$ image. The domains are separated by rows running along the $[1\bar{1}0]$ direction, and the angles formed by the rows with the $[110]$ direction are shown.

6.2.3 Third annealing cycle

The crystal was further annealed in UHV for twenty hours at 990 ± 50 K. The Auger spectrum shows a further increase of the calcium concentration (see table 6.1). Traces of potassium are still visible and a small sulphur peak appears. No LEED information are available for this annealing cycle. A ($2000\times 2000 \text{ \AA}^2$) STM image is shown in figure 6.9. A mechanically cut platinum-iridium tip was used with a sample bias of 1 V and a tunneling current of 0.1 nA. Terrace edges have become very rough. No rows are visible on the terraces on this occasion. The step height between adjacent terraces is now $\sim 2 \text{ \AA}$ or a multiple of this figure.

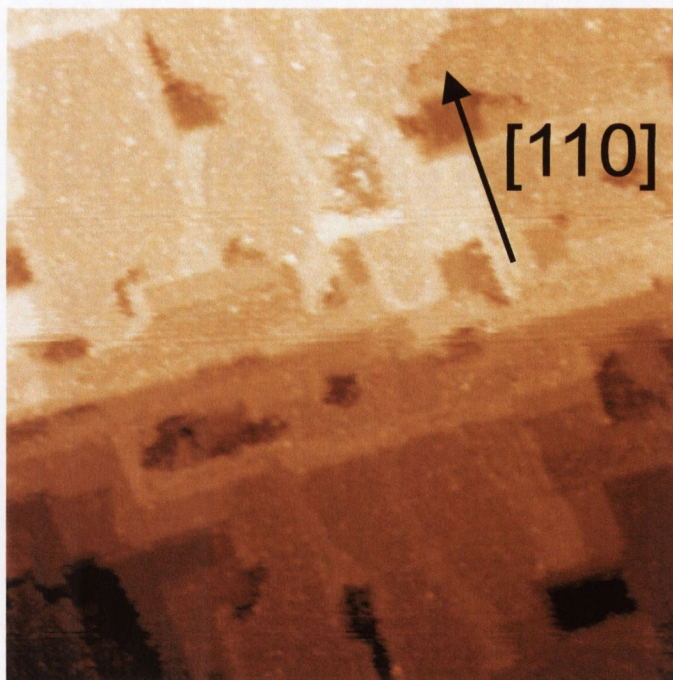


Figure 6.9: (2000×2000) \AA^2 STM image after the third annealing cycle. The image was acquired at a sample bias of 1.0 V and a tunneling current of 0.1 nA using a PtIr tip.

6.2.4 Fourth annealing cycle

Further annealing in UHV for 14 hours at 1030 ± 50 K produced a surface of poorer quality. The concentration of calcium increased further reaching a value of 9.5 at %. No potassium or sulphur were detected on the surface, as shown in fig. 6.10 by the corresponding Auger spectrum. The LEED pattern in fig. 6.11 (a) was observed. The streaked lines around the primary spots along the $[110]$ and $[1\bar{1}0]$ directions are not visible anymore and the additional diffraction spots of the $(\sqrt{2} \times \sqrt{2})R45^\circ$ reconstruction are lost too. The terrace definition and squareness is almost completely lost, as shown in figure 6.11 (b).

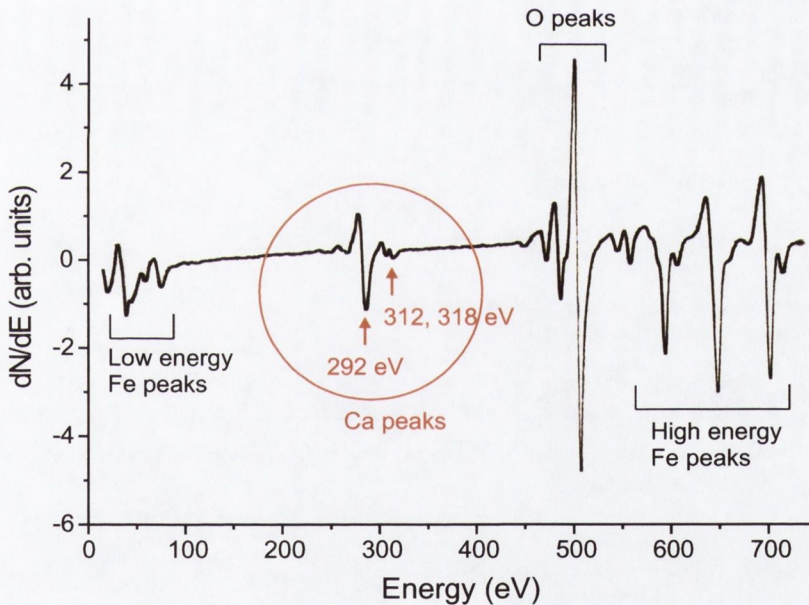


Figure 6.10: Fourth annealing cycle. Auger spectrum of an artificial $\text{Fe}_3\text{O}_4(001)$ single crystal after a 14 hours UHV annealing at 1030 ± 50 K. Ca concentration = 9.5 %, K concentration was below the detection limit of the analyzer.

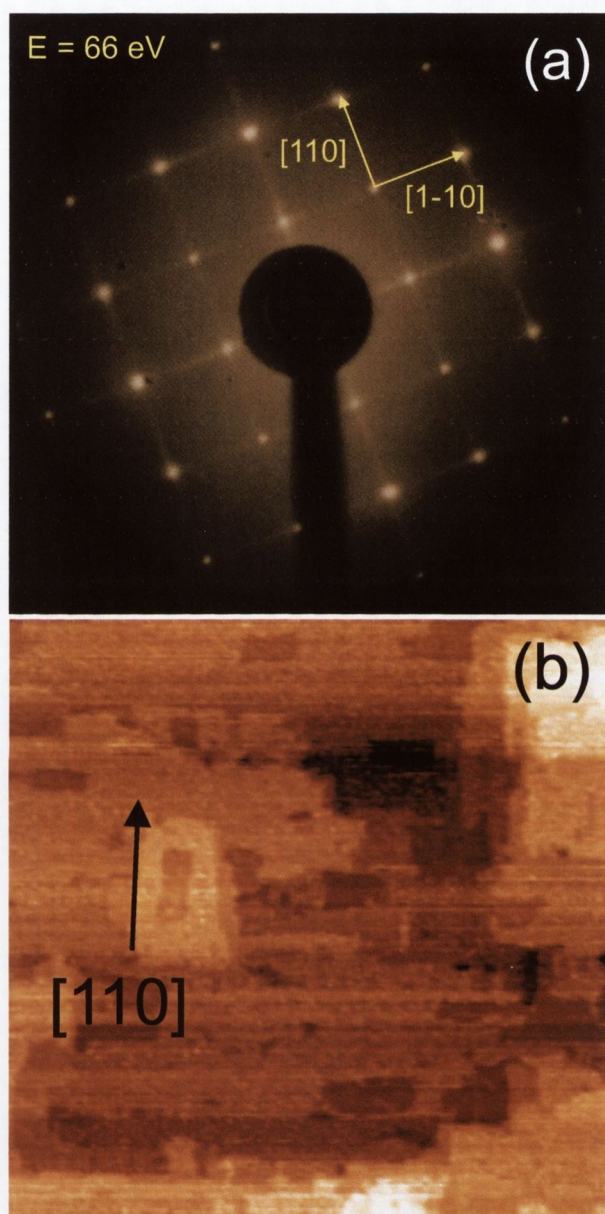


Figure 6.11: (a) LEED pattern observed with a primary electron energy of 93 eV. An artificial $\text{Fe}_3\text{O}_4(001)$ single crystal was annealed for 14 hours in UHV at $1030 \pm 50 \text{ K}$. (b) $(2000 \times 2000) \text{ \AA}^2$ STM image after the fourth annealing cycle. The image was acquired at a sample bias of 1.0 V and a tunneling current of 0.1 nA using a W tip.

6.2.5 $p(1\times 4)$ reconstruction on a natural $\text{Fe}_3\text{O}_4(001)$ single crystal

Surface structures very similar to the ones described above were observed by Seoighe [24] both on artificial and natural crystals of $\text{Fe}_3\text{O}_4(001)$. The artificial crystals came from the same nugget as the ones used during this thesis. The natural crystal came from Zillertal, Austria, and it showed a worse degree of stoichiometry as established by resistance versus temperature measurements (a Verwey transition temperature of 98 K was observed). The presence of rows, whose separation varied between 40 Å and 24 Å was observed on both types of crystals, although the natural one exhibited a better defined and sharper surface (Fig. 6.12 shows a (200×200) Å² STM image obtained by Seoighe on a natural crystal). LEED patterns identical to the ones described in sections 6.2.1 and 6.2.2 showed the presence of satellite spots at $\sim 1/4$ of the primary spot distance along the $[110]$ and $[1\bar{1}0]$ directions. These structures were attributed to the reconstruction of a clean $\text{Fe}_3\text{O}_4(001)$ surface, due to the lack of reliable AES data. We believe this interpretation is erroneous and the features observed, both with LEED and STM, are due to segregation of impurities from the bulk of the crystals. In the case of the artificial crystals this interpretation is strongly backed up by the fact that they came from the same source and they were prepared in the very same way. This suggests that the surface reconstruction is due to segregation of calcium to the surface. Concerning the natural crystal, although it was prepared using the same procedure, no data are available about its chemical composition. Since calcium is one of the most common impurities in metal oxides, it is likely to be the cause of the reconstruction observed. However, the possibility that the $p(1\times 4)$ reconstruction may be caused by the diffusion of a different element cannot be completely ruled out: a $p(1\times 4)$

6. $p(1 \times 4)$ reconstruction on $\text{Fe}_3\text{O}_4(001)$

and a $p(1 \times 3)$ reconstructions can be induced by diffusion of magnesium to the $\text{Fe}_3\text{O}_4(001)$ surface in thin magnetite films grown on MgO substrates ([86], [59]).

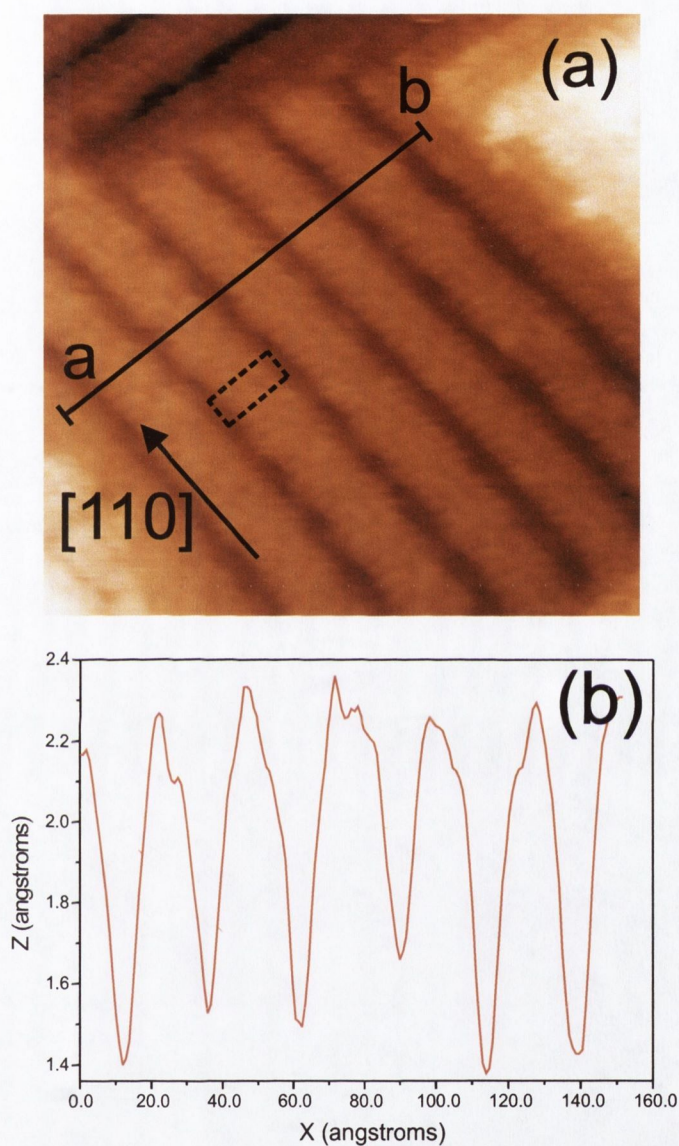


Figure 6.12: (a) $(200 \times 200) \text{ \AA}^2$ STM image of a natural $\text{Fe}_3\text{O}_4(001)$ single crystal. The image was acquired at a sample bias of 1.0 V and a tunneling current of 0.1 nA using a MnNi tip. The surface unit cell corresponding to the $p(1 \times 4)$ reconstruction is marked by the dashed rectangle. Reproduced from [24]. (b) Line profile along the a–b line.

6.3 Conclusion

As explained in the previous paragraphs, a crystal of $\text{Fe}_3\text{O}_4(001)$ was mechanically polished and then annealed in UHV at temperatures ranging between 990 and 1030 K for different periods of time (see table 6.1). Four cycles of annealing in UHV were performed, each of them resulting in a different chemical composition and structure of the surface. The key role in the interpretation of these results is played by the presence of calcium on the surface and in the topmost layers of the crystal.

Calcium is a common impurity in metal oxides, with typical concentrations in single crystals of the order of a few tens to a few hundred parts per million [93]. Calcium contamination may occur during the production¹ as well as during the preparation and transportation of the crystals. Calcium segregation has been studied on the $\text{MgO}(100)$ [94,95] and TiO_2 [96] surfaces. In the latter case the formation of a CaTiO_3 -like compound was suggested. We can identify four different stages corresponding to the four annealing cycles and to the Ca concentration on the crystal surface (see table 6.1):

1. Ca segregates from the bulk to the surface of the crystal as a consequence of the annealing. The LEED pattern shows the onset of a $p(1 \times 4)$ reconstruction. Topographic images show the presence of rows on top of the terraces whose separation varies between 21 and 30 Å. Although a 24 Å periodicity is expected for a $p(1 \times 4)$ reconstruction, the fact that the rows are poorly defined suggests that the surface is not fully reconstructed. We suggest that this reconstruction is due to the formation of a $\text{Ca}_x\text{Fe}_{3-x}\text{O}_4$ -like compound. A very faint $(\sqrt{2} \times \sqrt{2})R45^\circ$ mesh begins to appear. This is the reconstruction expected for a clean $\text{Fe}_3\text{O}_4(001)$

¹Prof. Y.M. Mukovskii, Moscow Steel and Alloy Laboratory. Private communication.

surface (see section 4.4). We attribute this reconstruction to the crystal planes right beneath the surface and topmost layers contaminated with calcium.

2. The Ca concentration increases after further annealing. The rows are now more regular and better defined, with an average periodicity of $26 \pm 0.5 \text{ \AA}$, very close to the expected value of 24 \AA . Satellite spots around the primary spots are still visible, consistently with the presence of rows on the terraces. The $(\sqrt{2} \times \sqrt{2})R45^\circ$ mesh is now much sharper indicating that extra annealing induced a better structuring of the surface. The fact that the $(\sqrt{2} \times \sqrt{2})R45^\circ$ reconstruction is now much sharper and seems to take over the $p(1 \times 4)$ reconstruction can be explained by the diffusion of calcium to the very surface of the crystal. In this way, the rows observed with STM are still expected but, since calcium is now present only at the very surface, the $(\sqrt{2} \times \sqrt{2})R45^\circ$ reconstruction appears stronger. The $1.0 \pm 0.1 \text{ \AA}$ step height observed between adjacent terraces indicates some degree of intermixing between tetrahedral and octahedral planes.
3. The third stage is believed to be a transition between a surface characterized by the competitive presence of a $p(1 \times 4)$ and a $(\sqrt{2} \times \sqrt{2})R45^\circ$ reconstructions and a surface showing a $p(1 \times 1)$ pattern.
4. This stage of the preparation corresponds to a surface of very poor quality. The terraces are poorly defined and their squareness is almost completely gone. No sign of reconstruction is shown by LEED. This stage corresponds to a massive diffusion of calcium to the surface (see fig. 6.10). Such a big segregation of calcium to the surface has the effect of removing both the $p(1 \times 4)$ and the $(\sqrt{2} \times \sqrt{2})R45^\circ$ recon-

structions, as shown by LEED. The LEED pattern is now $p(1 \times 1)$. As explained in section 4.2, a bulk-terminated, clean $\text{Fe}_3\text{O}_4(001)$ surface would be unstable. We suggest that the presence of calcium on the surface may remove the dangling bonds and give rise to a surface state more stable than the $p(1 \times 4)$ or $(\sqrt{2} \times \sqrt{2})R45^\circ$ reconstructions. A similar behaviour was observed on epitaxial $\text{Fe}_3\text{O}_4(001)$ thin films grown on $\text{MgO}(001)$ [86]. In this case, the lifting of a $(\sqrt{2} \times \sqrt{2})R45^\circ$ reconstruction was due to the segregation of magnesium from the substrate to the film surface, leading to the formation of a Mg overlayer.

Chapter 7

Atomic-scale contrast on a $\text{Fe}_3\text{O}_4(001)$ surface observed with an antiferromagnetic tip

7.1 Introduction

As discussed in section 5.3, annealing a magnetite crystal in UHV to temperatures in the surrounding of 1000 K causes a significant segregation of contaminants from the bulk to the surface. In chapter 6 we discussed a $p(1\times 4)$ reconstruction, which was attributed to the diffusion of calcium to the surface of the magnetite crystal. Another consequence of a long UHV annealing at high temperatures is the creation of oxygen vacancies and the transformation of the top surface layers to FeO [71].

A different preparation method (described in section 5.4) was developed by the author in the course of this study. This method produced a very clean surface (see fig. 5.7) on which atomic scale contrast was observed using an antiferromagnetic MnNi tip. In the following sections we will present the

7. Atomic-scale contrast on $\text{Fe}_3\text{O}_4(001)$

results obtained and we will discuss the possibility of a magnetic contrast effect.

7.2 LEED data

Fig. 7.1 shows a typical LEED pattern observed with a primary electron energy of 52 eV. Crystals prepared according to the procedure described in section 5.3 gave always rise to a very sharp $(\sqrt{2} \times \sqrt{2})R45^\circ$ reconstruction. The $(\sqrt{2} \times \sqrt{2})R45^\circ$ mesh is indicated by a red solid square: the reconstructed unit cell length is $a_{[100]} = 8.3 \pm 1.7 \text{ \AA}$. The $p(1 \times 1)$ unit cell is marked by a yellow dashed square and its unit cell length is $a_{[110]} = 5.9 \pm 1.2 \text{ \AA}$, in very good agreement with the expected value.

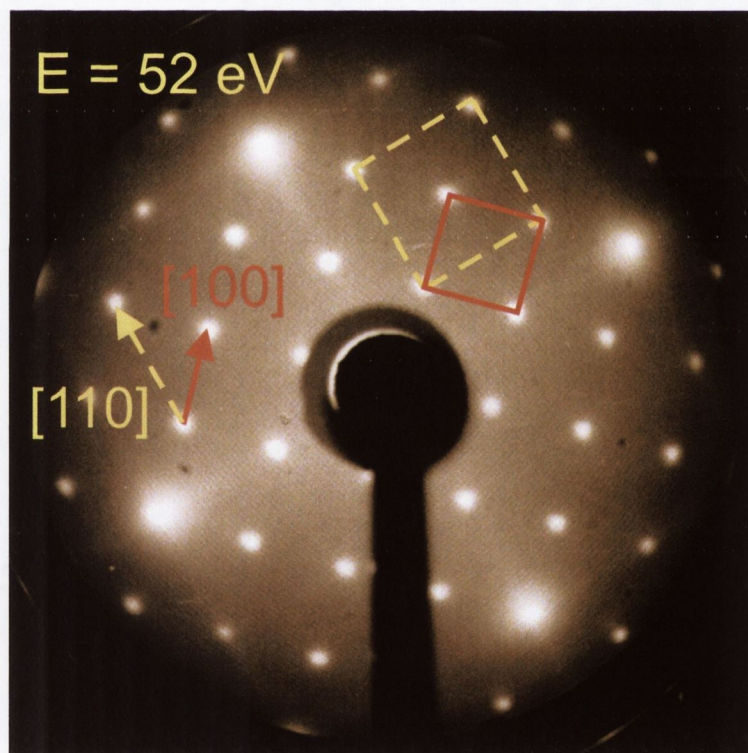


Figure 7.1: LEED pattern of a clean $\text{Fe}_3\text{O}_4(001)$ surface observed with a primary electron energy of 52 eV. A very sharp $(\sqrt{2} \times \sqrt{2})R45^\circ$ mesh is visible. The $p(1 \times 1)$ unit cell and the $(\sqrt{2} \times \sqrt{2})R45^\circ$ superlattice are indicated by a yellow dashed square and a red solid square, respectively.

7.3 STM data

Large-scale STM measurements showed a surface characterized by the presence of large and flat terraces. All the STM images shown in this chapter were obtained using an antiferromagnetic MnNi tip. Figure 7.2 shows a $(1000 \times 1000) \text{ \AA}^2$ image on which four terraces, onto which atomic resolution was obtained, are numbered. The step heights between the four terraces are shown by the line profiles in fig. 7.3; they are integer multiple of 2.1 \AA , which corresponds to the separation between A - A or B - B planes. The step height between terrace "1" and terrace "2" is $12.6 \pm 1.3 \text{ \AA}$, terrace "3" and "4" belong to the same atomic plane and are separated by $2 \pm 0.2 \text{ \AA}$ from terrace "2". Terraces "1", "2" and "3" are quite large, measuring about $(350 \times 480) \text{ \AA}^2$, $(280 \times 280) \text{ \AA}^2$ and $(480 \times 280) \text{ \AA}^2$, respectively; their edges are well defined and aligned along the $\langle 110 \rangle$ directions. Terrace "4" is significantly smaller, measuring some $(300 \times 100) \text{ \AA}^2$, and its uneven edges are not aligned along the $\langle 110 \rangle$ directions.

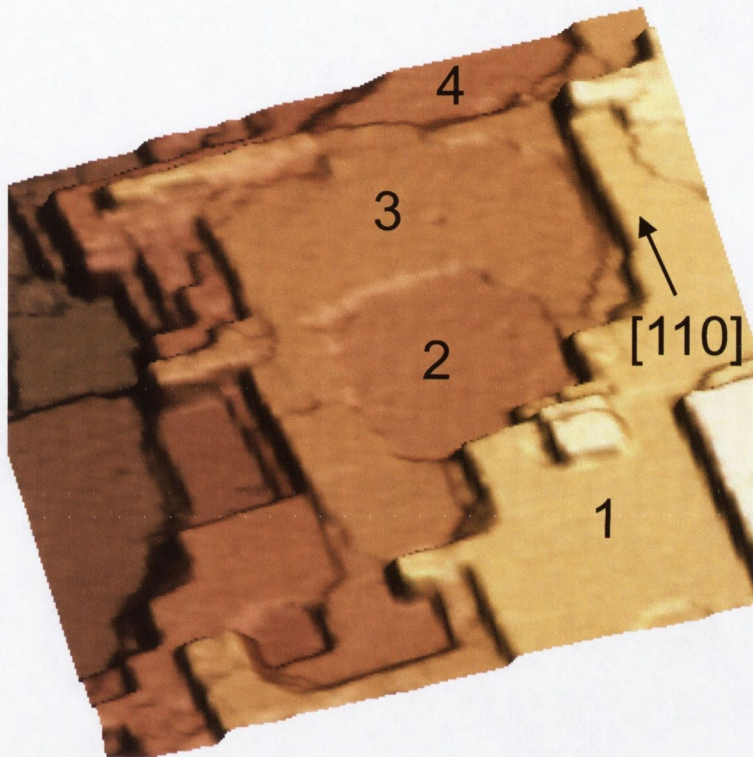


Figure 7.2: 3D view of a $(1000 \times 1000) \text{ \AA}^2$ image. Four terraces, onto which atomic resolution was obtained, are numbered. The step height between terrace "1" and terrace "2" is $12.6 \pm 1.3 \text{ \AA}$, terrace "3" and 4 belong to the same atomic plane and are separated by $2 \pm 0.2 \text{ \AA}$ from terrace "2". $V_{bias} = 1.0 \text{ V}$, $I_{tunnel} = 0.1 \text{ nA}$, MnNi tip.

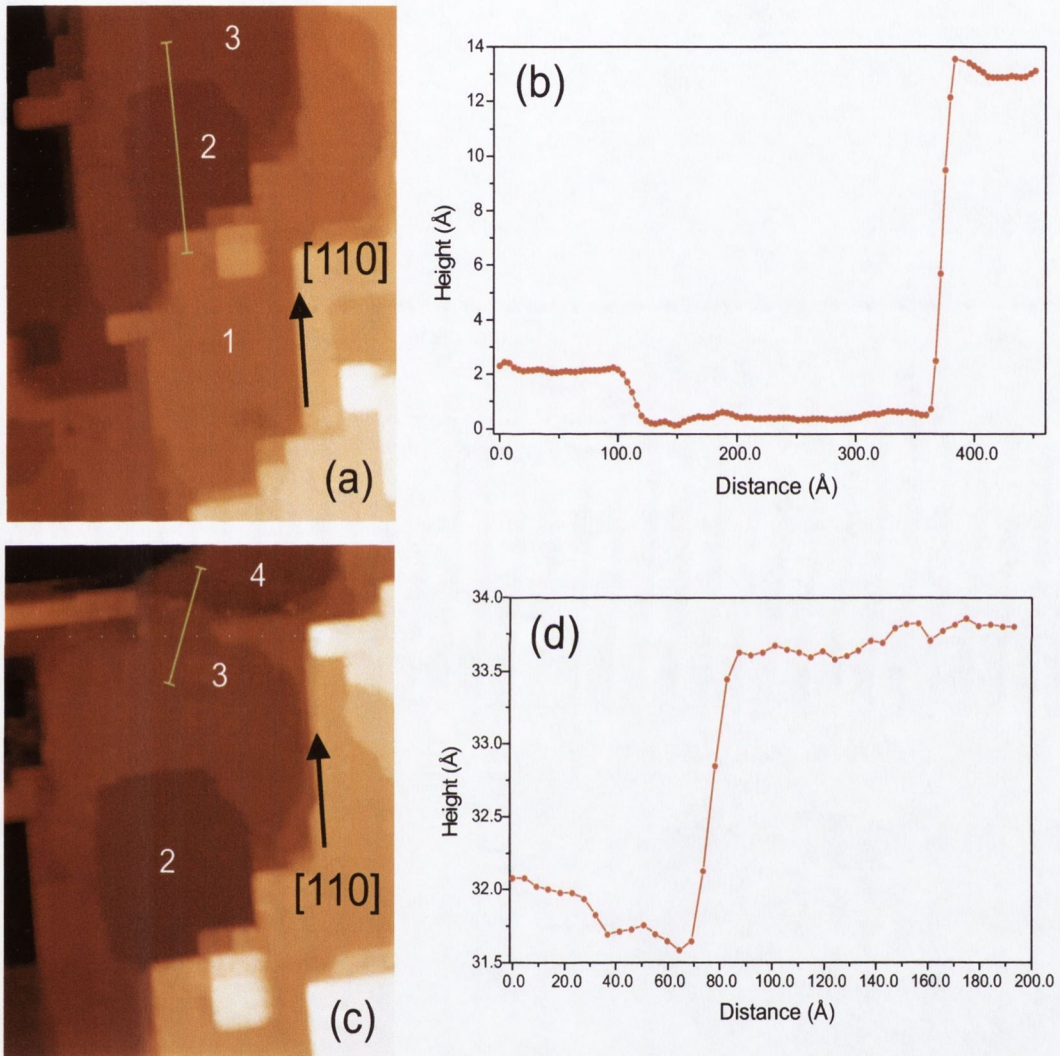


Figure 7.3: (a) $(770 \times 1000) \text{ \AA}^2$ image. $V_{bias} = 1.0 \text{ V}$, $I_{tunnel} = 0.1 \text{ nA}$, MnNi tip. (b) Line profile taken along the green line across terraces 1, 2 and 3. (c) $(620 \times 800) \text{ \AA}^2$ image. $V_{bias} = 1.0 \text{ V}$, $I_{tunnel} = 0.1 \text{ nA}$, MnNi tip. (d) Line profile taken along the green line across terraces 3 and 4.

Fig. 7.4 (a) shows terrace "1" in greater detail. The edges of this terrace are very sharp and aligned along the $\langle 110 \rangle$ directions. Three different step height values were measured in different areas of this image. Fig. 7.4 (b) shows a $(2.1 \pm 0.2 \text{ \AA})$ and a $(8.4 \pm 0.8 \text{ \AA})$ separation between neighbouring terraces; fig. 7.4 (d) shows three terraces separated by $6.3 \pm 0.6 \text{ \AA}$. Adjacent terraces are separated by twice the atomic step of the magnetite unit cell; a monoatomic step equal to $1.0 \pm 0.1 \text{ \AA}$ was never observed on a surface prepared in this fashion. On the basis of this observation we can rule out the presence of both tetrahedral and octahedral atomic planes on the surface. The very good agreement between the measured and expected values of the step heights also suggests a negligible effect of interlayer relaxation. Although the AES spectrum acquired right before the STM session showed a clean surface (see fig. 5.7), fig. 7.4 (a) gives indication of the presence of contaminants. These are best seen in the 3D representation showed in fig. 7.4 (c) in the shape of bright clusters whose concentration appears to be higher in the proximity of terraces edges. No information about the chemical nature of these adsorbates is available since their concentration was below the detection limit of our AES setup; however, on the basis of previous experiments we can speculate that either Ca diffusing from the bulk, or residual C in the UHV chamber, may be the cause of the surface contamination. A final consideration about this image concerns the presence of rows running along the $[100]$ direction. These rows can be barely seen in fig. 7.4 (c) but a zoom onto terrace "1" reveals a very sharp and defined atomic structure.

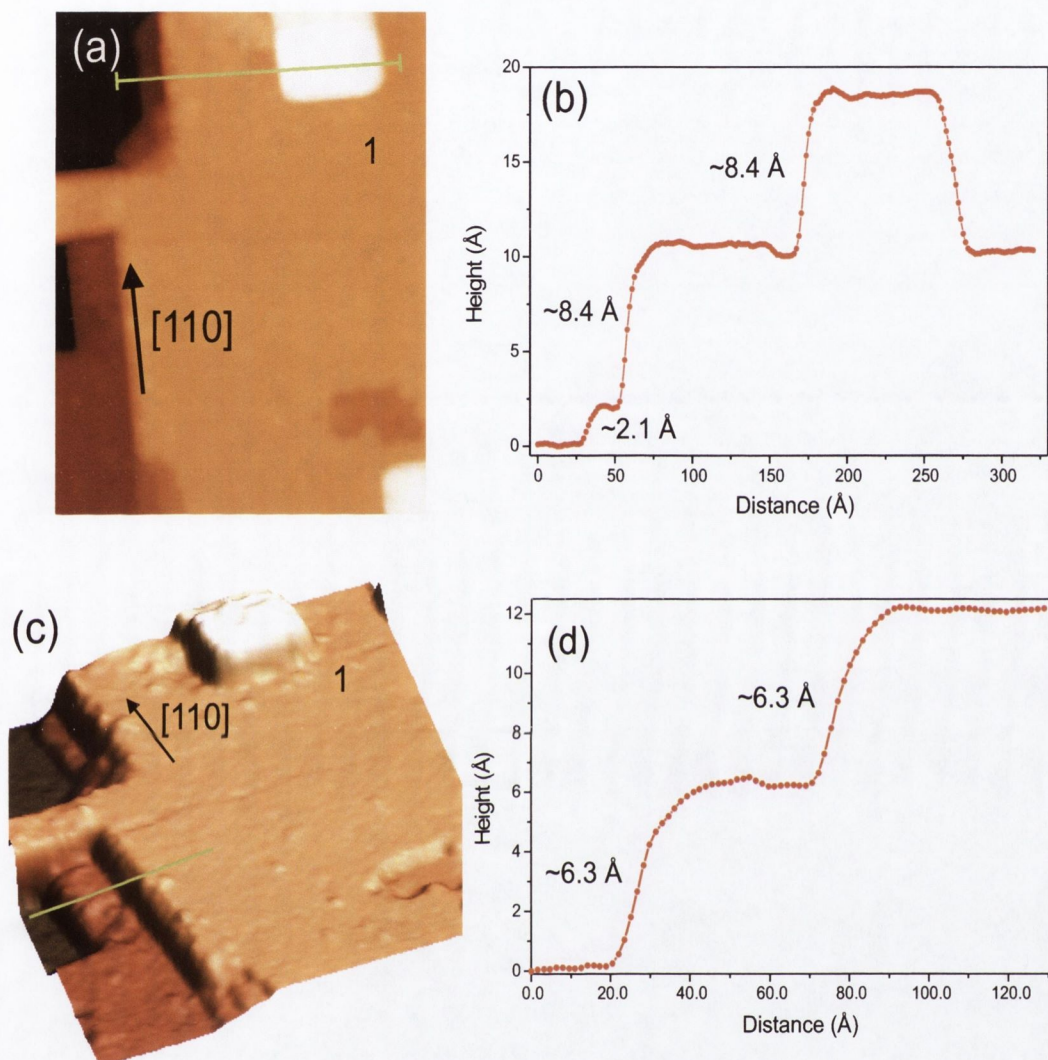


Figure 7.4: (a) 2D view of a $(300 \times 400) \text{ \AA}^2$ image. (b) Line profile taken along the green line across four terraces. (c) 3D view of the same image. A more detailed view of terrace "1" is shown. Clusters indicating the presence of adsorbates on the surface are visible, especially in the vicinity of terrace edges. Rows running along the $[100]$ direction are visible onto terrace "1". (d) Line profile along the green line taken across three terraces. $V_{bias} = 1.0 \text{ V}$, $I_{tunnel} = 0.1 \text{ nA}$, MnNi tip.

Figure 7.5 shows a $(140 \times 210) \text{ \AA}^2$ image that was obtained scanning over terrace "1" using a sample bias of 1.0 V and a tunneling current of 0.1 nA. Atomic rows running along the $[110]$ direction and separated by $\sim 5.5 \text{ \AA}$ are visible. The periodicity along the rows is $\sim 10 \text{ \AA}$. Despite the presence of adsorbates – the bright spots indicated in fig. 7.5 – and vacancies, the atomic rows are quite regular. A higher resolution image is shown in fig. 7.6 (a) where a $(70 \times 70) \text{ \AA}^2$ area was scanned few minutes later using the same parameters. The separation between adjacent rows confirms the value of $\sim 5.5 \text{ \AA}$ measured in the previous image. The periodicity along the $[110]$ direction was also found to be $\sim 10 \text{ \AA}$ and the periodicity along the $[100]$ direction $\sim 7.3 \text{ \AA}$. The comparison of these values with the ones calculated from the LEED pattern of fig. 7.1 shows a misfit of about 10–17 %. In other words, the lengths calculated from the STM pictures are 10–17 % smaller than expected. We attribute this to the fact that the calibration of the tube scanner was carried out using a tungsten tip, while these images were obtained with MnNi tips that are usually 1–2 mm longer than the W ones, leading to an under estimate of the measured distances. Taking this into account, and using the LEED results as a confirmation of this hypothesis, the rows' periodicity on terrace "1" along the $[110]$ direction is $\sim 12 \text{ \AA}$. The distance along the $[100]$ direction is now $\sim 8.4 \text{ \AA}$. A cubic symmetry is clearly seen on the surface; a black square marked in fig. 7.6 (a) can be identified with the $(\sqrt{2} \times \sqrt{2})R45^\circ$ reconstructed unit cell, in agreement with the results showed by the LEED analysis (see fig. 7.1). Caution must be used in the interpretation of STM images of metal oxide surfaces, since these are not simply topographical contours of a surface but rather its electronic LDOS [97]. Theoretical calculations [10] and experimental evidence [98] show that the O $2p$ states lie well below E_F and are therefore not accessible for tunneling experiments. This

means that the contrast in the STM images mainly originates from the Fe $3d$ states. We conclude that STM images of Fe_3O_4 are dominated by Fe cations, which we identify as the bright spots on the surface in figures 7.5 and 7.6 (a). We believe that these spots correspond to Fe cations at octahedral B sites. As stated above, the separation between two adjacent bright spots along the $[110]$ direction is $\sim 12 \text{ \AA}$, which corresponds to 4 times the distance between Fe cations in octahedral B sites in the bulk. The bright spots on neighboring rows are shifted by $\sim 6 \text{ \AA}$ and a measurement of their Full Width at Half Maximum (FWHM) gave an average value of 3 \AA . A closer analysis reveals the presence of extra spots between the bright ones; the line profile taken along the green line shows that the extra spots are at an equal distance of $\sim 6 \text{ \AA}$ between the bright spots (see fig. 7.6 (b)). The corrugation of the bright spots is $\sim 0.2 \text{ \AA}$ and the one of the extra spots is $\sim 0.1 \text{ \AA}$.

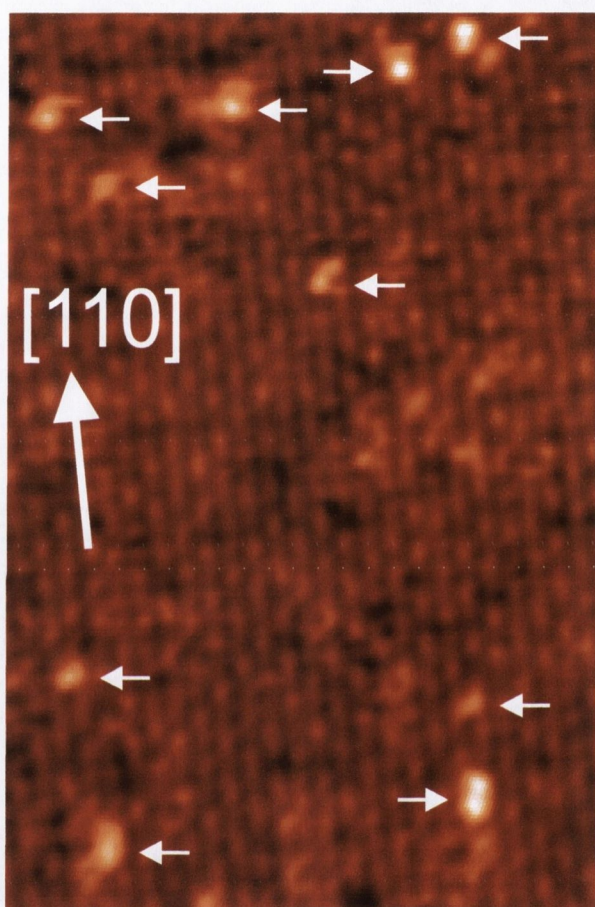


Figure 7.5: $(140 \times 210) \text{ \AA}^2$ STM image. Rows of atoms running along the $[110]$ direction are visible. The presence of adsorbates, possibly Ca or C, is indicated by small white arrows. The image was acquired at a positive sample bias of 1.0 V and a tunneling current of 0.1 nA using a MnNi tip.

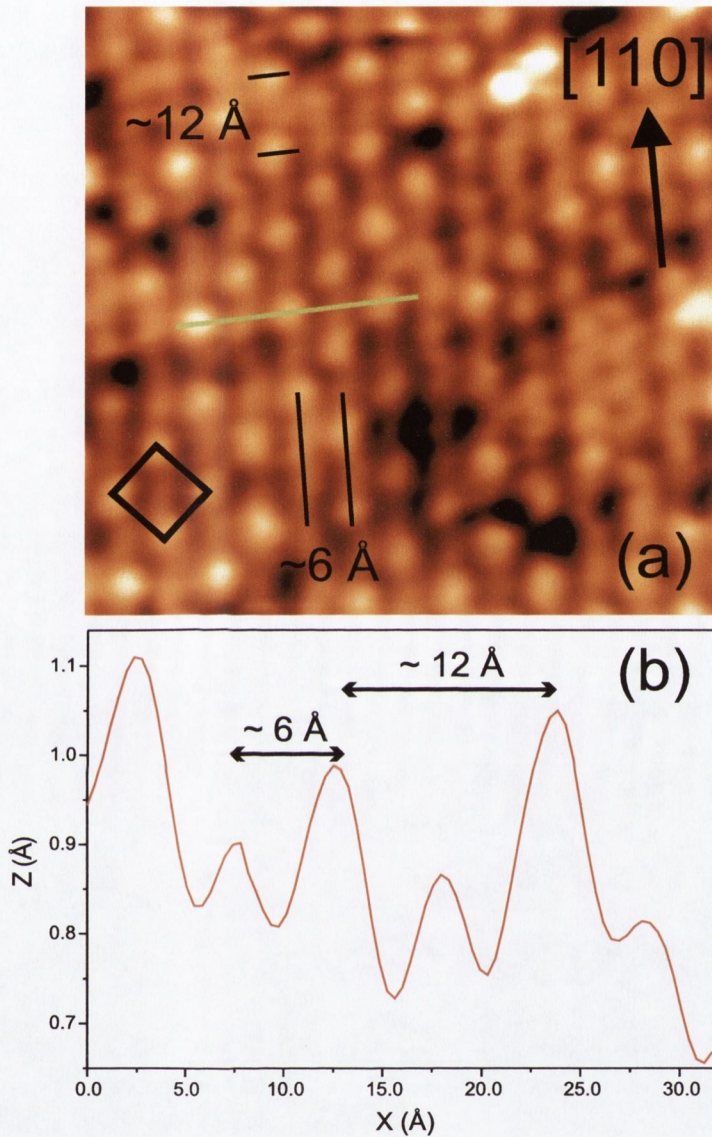


Figure 7.6: (a) $(70 \times 70) \text{ \AA}^2$ STM image. The bright spots correspond to Fe cations at octahedral B sites. A $\sim 6 \text{ \AA}$ shift between neighbouring rows is observed. (b) Line profile taken along the green line shown in fig. 7.6. The separation between two bright spots along the $\langle 110 \rangle$ directions is $\sim 12 \text{ \AA}$; an extra spot, at an equal distance of $\sim 6 \text{ \AA}$ between the bright spots is revealed by the line profile. The image was acquired at a positive sample bias of 1.0 V and a tunneling current of 0.1 nA using a MnNi tip.

Fig. 7.7 shows a 3D view of terraces "2" and "3". Terrace "2", approximately $(280 \times 280) \text{ \AA}^2$ in size, appears to be a hole in the middle of terrace "3" (see fig. 7.2), from which is separated by $2.1 \pm 0.2 \text{ \AA}$. A zoom on terrace "2", shown by the insert in fig. 7.7, reveals an atomically resolved structure. Although the corrugation measured along the rows is only $\sim 0.1 \text{ \AA}$, due to the fact that the $(300 \times 300) \text{ \AA}^2$ scan area is quite big, the atomic contrast is evident. A careful analysis revealed a surface structure identical to the one observed in figures 7.5 and 7.6. Atomic rows running along the [110] direction and separated by $\sim 6 \text{ \AA}$ are visible, as well as the $\sim 6 \text{ \AA}$ shift between bright spots on adjacent rows. The periodicity measured along the [110] direction was $\sim 10 \text{ \AA}$.

Fig. 7.8 shows a 3D view of terraces "2", "3" and "4". Terraces "2" and "4" belong to the same atomic plane and are separated from terrace "3" by $2.1 \pm 0.2 \text{ \AA}$. The presence of atomic rows running along the [010] direction is evident from the insert shown in fig. 7.8. The periodicity along these rows varies from $\sim 5.9 \text{ \AA}$ to $\sim 7.8 \text{ \AA}$; the average value was measured to be $\sim 7 \text{ \AA}$. The presence of adsorbates and vacancies, noted already on terraces "1" and "2", is more obvious on terraces "3" and "4" and contributed to make the surface highly irregular. This fact, together with a corrugation smaller than 0.1 \AA , does not allow us to draw any definitive conclusion about the surface symmetry on this terrace.

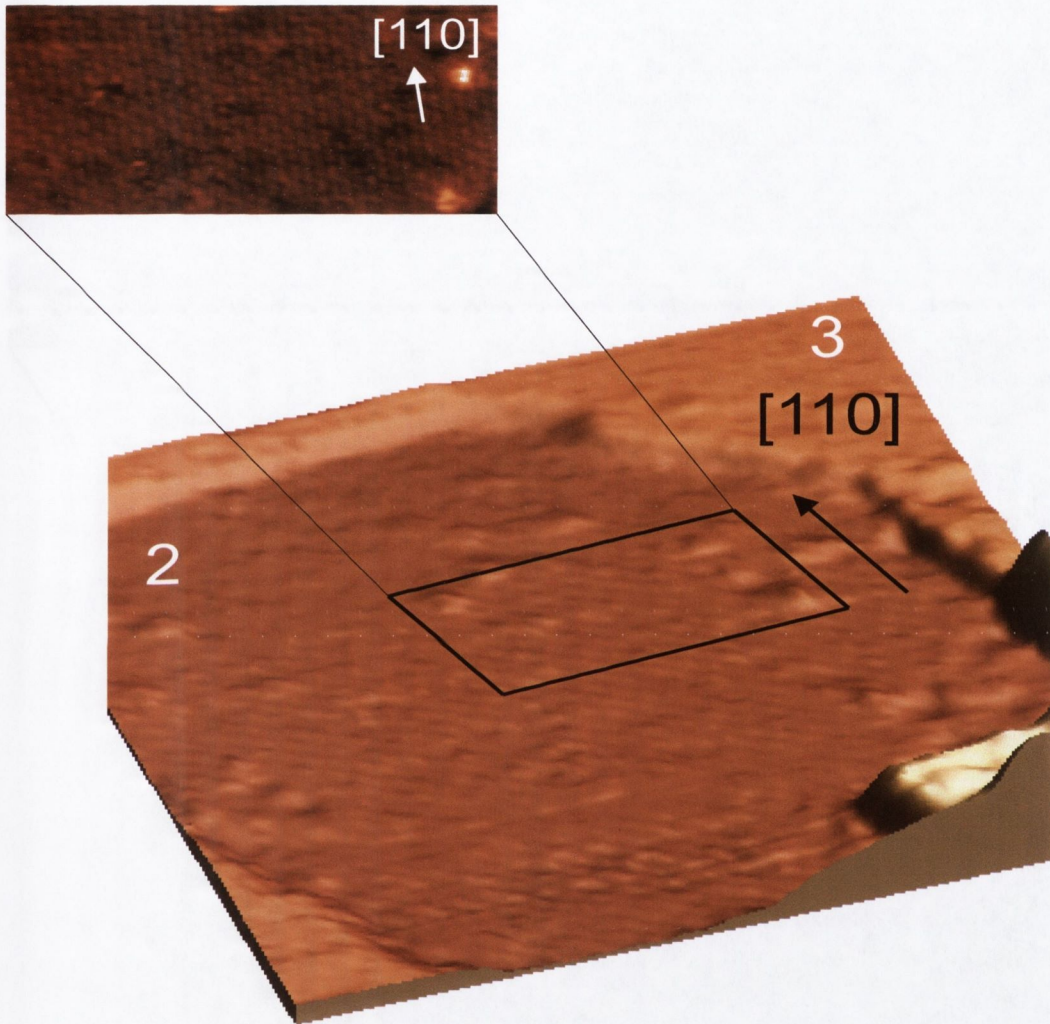


Figure 7.7: 3D view of terraces "2" and "3". The image is $(300 \times 300) \text{ \AA}^2$. The insert reveals an atomically resolved structure imaged on terrace "2" identical to the one observed on terrace "1" (see figures 7.5 and 7.6 for comparison). $V_{bias} = 1.0 \text{ V}$, $I_{tunnel} = 0.1 \text{ nA}$, MnNi tip.

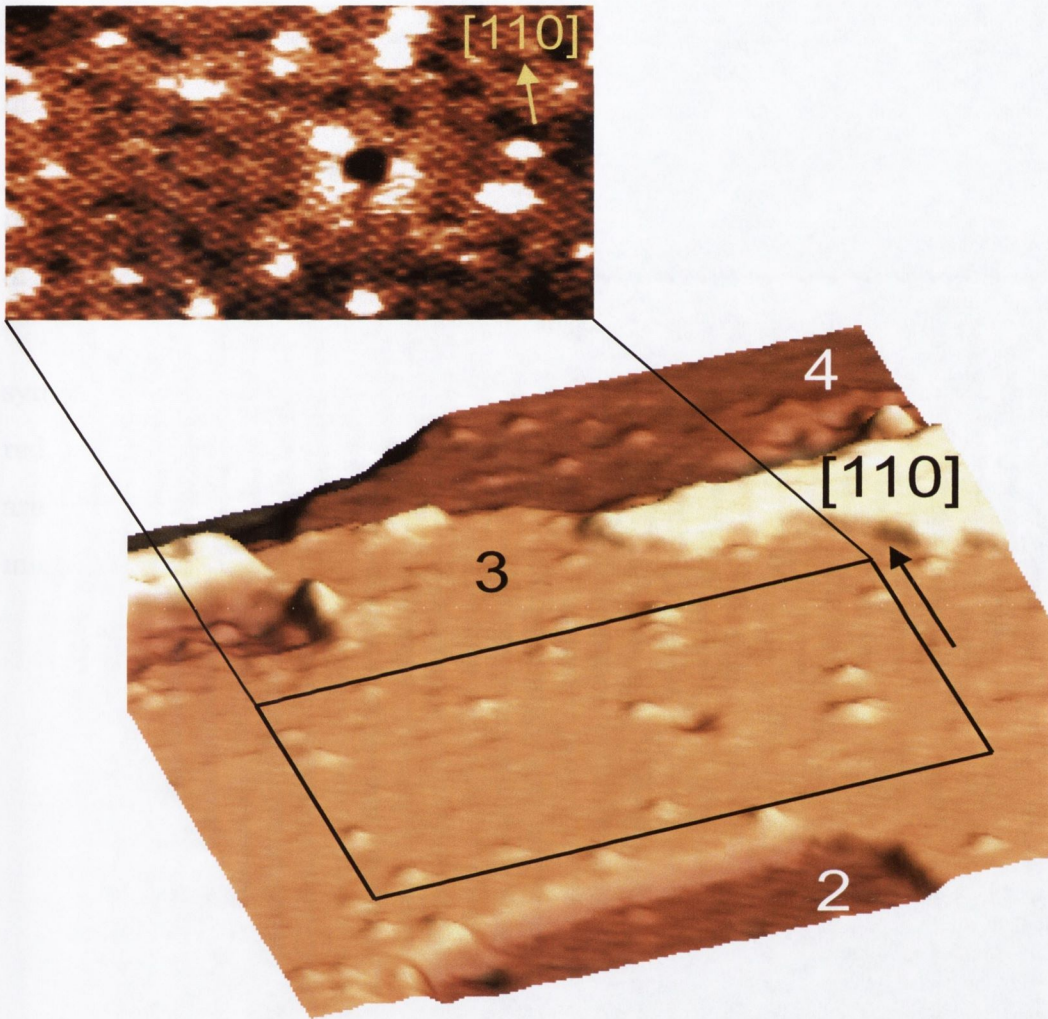


Figure 7.8: 3D view of terraces "2", "3" and "4". The image is $(400 \times 400) \text{ \AA}^2$. The insert reveals an atomically resolved structure imaged on terrace "3". $V_{bias} = 1.0 \text{ V}$, $I_{tunnel} = 0.1 \text{ nA}$, MnNi tip.

Figure 7.9 shows terraces "3" and "4" separated by $2.1 \pm 0.2 \text{ \AA}$. A $(100 \times 140) \text{ \AA}^2$ image (fig. 7.9 (c)) reveals some features worth to be noticed. Atomic rows can be identified, especially in the upper part of the image. The atomic rows change their orientation by 90° from one terrace to the next, in agreement with the surface structure of the *B*-sublattice of magnetite. Although atomic rows were resolved on terrace "3", (see fig. 7.8), atomic resolution on the same terrace in fig. 7.9 (c) was not achieved. An analysis of the rows on terrace "4" revealed a $\sim 5 \text{ \AA}$ periodicity along the $[110]$ direction; these rows are separated by $\sim 5 \text{ \AA}$ suggesting the presence of a $p(1 \times 1)$ symmetry on terrace "4". Fig. 7.9 (d) shows the line profile taken along the red line marked in fig. 7.9 (a); atomic rows oriented along the $[1\bar{1}0]$ direction are visible on this small terrace; a $\sim 5 \text{ \AA}$ periodicity along these rows was measured, in agreement with the values measured on terrace "4".

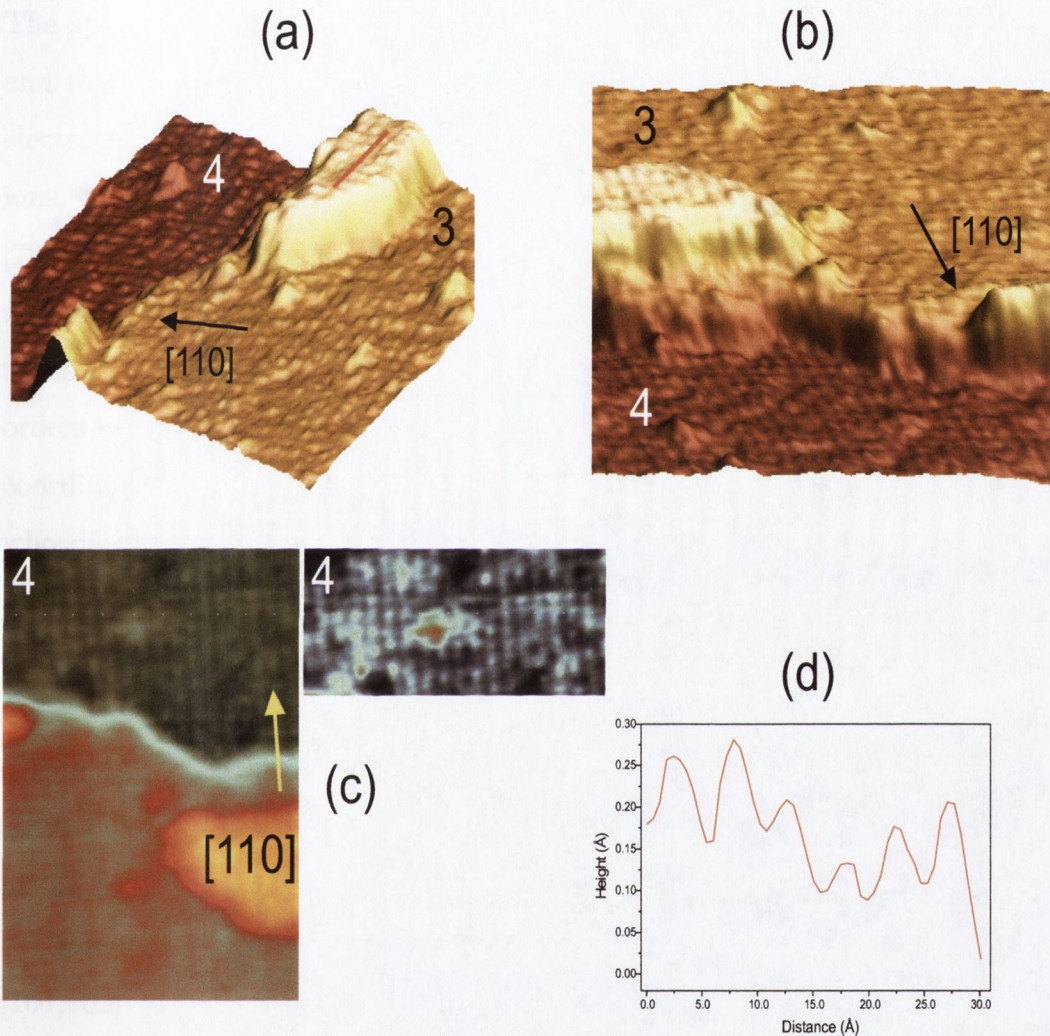


Figure 7.9: (a), (b) 3D views of terraces "3" and "4" from two different perspectives. (c) 2D view of a $(95 \times 140) \text{ \AA}^2$ image. A zoom on terrace "4" is shown. (d) Line profile taken along the red line shown in fig. 7.9 (a). $V_{bias} = 1.0 \text{ V}$, $I_{tunnel} = 0.1 \text{ nA}$, MnNi tip.

7.4 Discussion

Magnetite owes its electrical conductivity to a charge hopping mechanism. The spin configuration of the Fe²⁺ and Fe³⁺ ions is $3d^5\uparrow 3d\downarrow$ and $3d^5\uparrow$, and their magnetic moments are $4\mu_B$ and $5\mu_B$, respectively. The sixth d -electron of Fe²⁺ with spin \downarrow hops among the octahedrally coordinated Fe ions, causing a bulk conductivity of $\sim 100\Omega^{-1}\text{cm}^{-1}$ at room temperature [78]. Below the Verwey transition temperature T_V , magnetite undergoes a structural and electronic transition; the crystal structure changes from cubic to monoclinic and the electrical conductivity drops by approximately two orders of magnitude [84]. Below T_V a "charge freezing" on the octahedrally coordinated B sites takes place. Charge ordering was studied by Wigner [99] who determined that the critical parameter for a "Wigner localization" to set in is the ratio V_0/B , where V_0 is the Coulomb interaction energy between charge carriers on nearest-neighbour sites and B is the electronic bandwidth. Coey *et al.* [100] proposed that surface anisotropy near the surface may cause a splitting of the $3d\downarrow$ electron levels and a consequent reduction of the electronic bandwidth. This may increase the Verwey transition temperature at the surface and cause a "Wigner localization" at room temperature.

Spin-polarized tunneling was theoretically investigated by Slonczewski [101,102] in the case of a tunnel junction of two ferromagnets (f, f') separated by a non-magnetic barrier b . In a one-dimensional model, in the limit of a free-electron metal at zero temperature, small bias voltage and small barrier transmission, Slonczewski calculated the conductance of the tunnel junction to be:

$$G = G_{fbf'}(1 + P_{fb}P_{f'b}\cos\theta) \quad (7.1)$$

where $G_{fbf'}$ is the mean surface conductance, P_{fb} ($P_{f'b}$) is an effective spin

polarization of the ferromagnet-barrier junction, and θ is the angle between the spin quantization axes of the two ferromagnetic electrodes. Applying this model to an STM tunnel junction, taking into account that the magnetization of the tip and the angle θ between the magnetization of tip and sample are constant, the magnetization-dependent component of the tunneling current becomes:

$$I_m \propto | \mathbf{m}_S | \quad (7.2)$$

where \mathbf{m}_S is the magnetic moment of the sample. Since the magnetic moment of a Fe²⁺ ion is $4 \mu_B$ and the one for a Fe³⁺ ion is $5 \mu_B$, those ions should be distinguishable with a spin-polarized tip.

The images shown in figures 7.5, 7.6 and 7.7 show atomic rows separated by $\sim 6 \text{ \AA}$ running along the [110] direction. A line profile of the rows along [110] reveals two different types of features, which we'll refer to as "bright spots" and "extra spots" for simplicity (see fig. 7.6 (b)). The bright spots are separated by $\sim 12 \text{ \AA}$, but the separation between one "bright spot" and one "extra spot" is $\sim 6 \text{ \AA}$. The corrugation of the "bright spots" is $\sim 0.2 \text{ \AA}$, approximately twice that of the "extra spots". Assuming that the different contrast of "bright spots" and "extra spots" originates from a difference in the LDOS, the structure observed could not be explained in terms of a tetrahedrally terminated surface, since only one species of Fe cations is present in the *A*-sublattice. Even the interpretation of these images in terms of mere topographical contours of the surface would not fit the half-filled *A* layer model described in section 4.3.4. In this case the 12 \AA periodicity between "bright spots" would be caused by a missing tetrahedral Fe³⁺ per unit cell. The "extra spots", imaged in the position of the missing tetrahedral ions, would appear less bright because they would sit one atomic plane below the surface layer; but this is not compatible with the structure of magnetite,

since the octahedral ions are not placed exactly under the tetrahedral ones but they are shifted by 1.05 \AA . No shift is observed in our images. Another argument in favour of an octahedral termination can be obtained by the image shown in fig. 7.9 (c); in this image atomic rows are visible on two terraces separated by $2.1 \pm 0.2 \text{ \AA}$, and a change in their orientation by 90° from one terrace to the next is visible, in agreement with the structure of the B -sublattice in magnetite. On the basis of these observations, we conclude that the surface is terminated at the B -sublattice.

The expected separation along the $[110]$ direction between two adjacent Fe cations in octahedral B sites in bulk magnetite is $\sim 3 \text{ \AA}$ and such a periodicity was never observed on any of the images we obtained. Spin polarized tunneling may be the origin of the anomalous periodicity observed. Wiesendanger *et al.* [4, 5, 103] observed a 12 \AA periodicity of the atomic rows on a $\text{Fe}_3\text{O}_4(001)$ surface of a natural single crystal using an Fe tip. This experiment was recently repeated by Koltun *et al.* [104] on an artificial $\text{Fe}_3\text{O}_4(001)$ single crystal. This was explained in terms of magnetic contrast based on the theoretical predictions of Iida *et al.* [105, 106] and Kita *et al.* [107]. They studied the possible configurations of Fe^{2+} and Fe^{3+} in the low temperature phase of Fe_3O_4 , showing that a 12 \AA periodicity along the rows of Fe ions at B sites is expected. These configurations are known as the Mizoguchi's patterns and are shown in fig. 7.10. According to these models, the rows of iron ions in the B -sublattice are separated by 6 \AA , and the Fe^{2+} and Fe^{3+} ions, whose periodicity is 12 \AA , take one of the two configurations shown in fig. 7.10.

Our data indicate a B -terminated surface where an anomalous periodicity is also observed; the atomic rows running along the $[110]$ direction appear to be composed by two different species of octahedrally coordinated Fe ions.

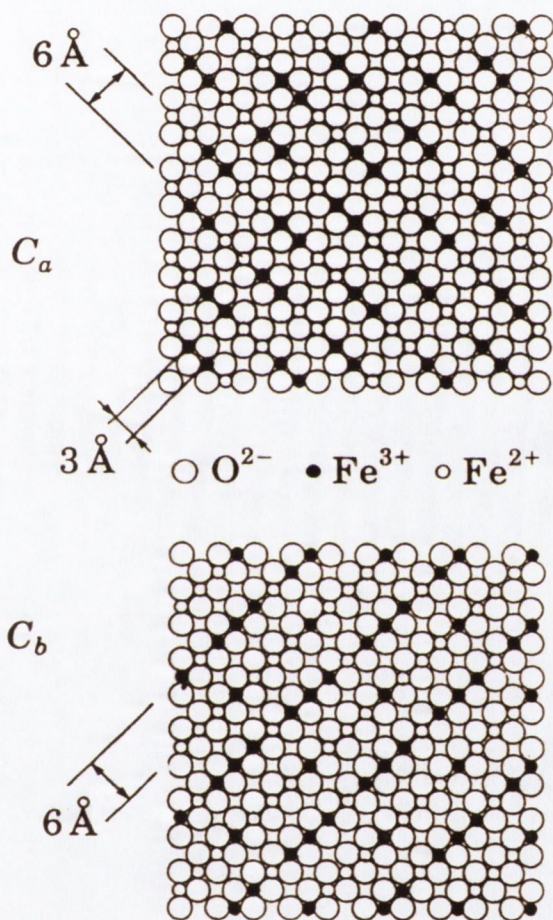


Figure 7.10: Mizoguchi's patterns of Fe_3O_4 on C_a and C_b planes.

This may be explained in terms of spin-dependent electron tunneling, considering that the antiferromagnetic tip we used provided magnetic contrast allowing the resolution of pairs of Fe^{2+} and pairs of Fe^{3+} ions. The origin of the contrast may rise from the different spin polarization of the two Fe species. The Fe^{2+} have a large \downarrow LDOS near the Fermi level, which is absent for the Fe^{3+} ions. The tunnel current will depend on the relative orientation of the sample and tip magnetization. The Fe^{2+} will appear as bright spots with a higher corrugation in the STM images than the Fe^{3+} ions. The 6 Å periodicity measured between "bright spots" and "extra spots" can be explained in terms of a "Wigner localization" leading to a static arrangement of pairs of Fe^{2+} and pairs of Fe^{3+} ions. A ~ 3 Å Full Width at Half Maximum (FWHM) of the "bright spots" confirms this hypothesis, suggesting that a "bright spot" does not correspond to a single Fe^{2+} ion but rather to a pair of Fe^{2+} ions.

The pattern we observed differs from the one predicted by the Mizoguchi's patterns in the relative shift between the maxima of adjacent rows, which is 6 Å instead of 3 Å. Although this may be a cause of concern, we have to remember that the Mizoguchi's patterns refer to the bulk of magnetite and not to its surface.

Voogt proposed a model of an octahedrally terminated surface in which the $(\sqrt{2} \times \sqrt{2})R45^\circ$ reconstruction is due to an ordered array of oxygen vacancies [59]. The missing oxygen atom would act as a 2^+ impurity and could trap conducting electrons from neighboring sites. This would induce a charge ordering at the surface, as shown in fig. 7.11; changing the oxidation state from $2.5+$ to $3+$ of two Fe ions per unit cell would produce a stable surface. A schematic model of the surface structure we have observed by LEED and STM is shown in fig. 7.12. This model shows the (001) surface of magnetite

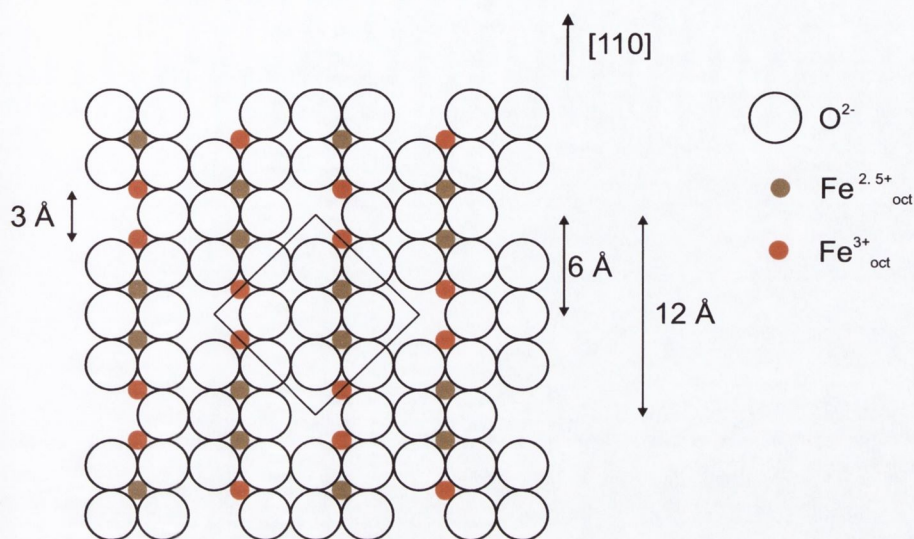


Figure 7.11: Schematic model of the structure proposed by Voogt. An ordered array of oxygen vacancies causes the $(\sqrt{2} \times \sqrt{2})R45^\circ$ reconstruction. To achieve a stable surface, oxygen vacancies must be accompanied by the oxidation of two Fe^{2.5+} ions to Fe³⁺ per unit cell.

terminated at the octahedral plane; the Fe²⁺_{oct} ions and the Fe³⁺_{oct} ions are represented as blue spheres and red spheres, respectively. Charge ordering on the surface results in the pairing of Fe²⁺ and Fe³⁺ along the [110] direction; a pair of Fe²⁺ ions is imaged by the STM as a "bright spot" and a pair of Fe³⁺ ions is imaged as an "extra spot". This model is based on the idea that the driving force inducing the $(\sqrt{2} \times \sqrt{2})R45^\circ$ reconstruction is due to the charge ordering at the surface and not to an array of oxygen vacancies.

Figure 7.9 shows a different type of structure where Fe rows with a lateral separation of 6 Å and a periodicity along the rows of 6 Å were observed. The terraces where the two different types of structures were imaged are separated by 12.6 Å. Assuming that the surface is *B*-terminated, this means that both terraces expose an octahedrally coordinated atomic plane. The fact that a 12 Å periodicity was observed only on certain areas of the crystal suggests

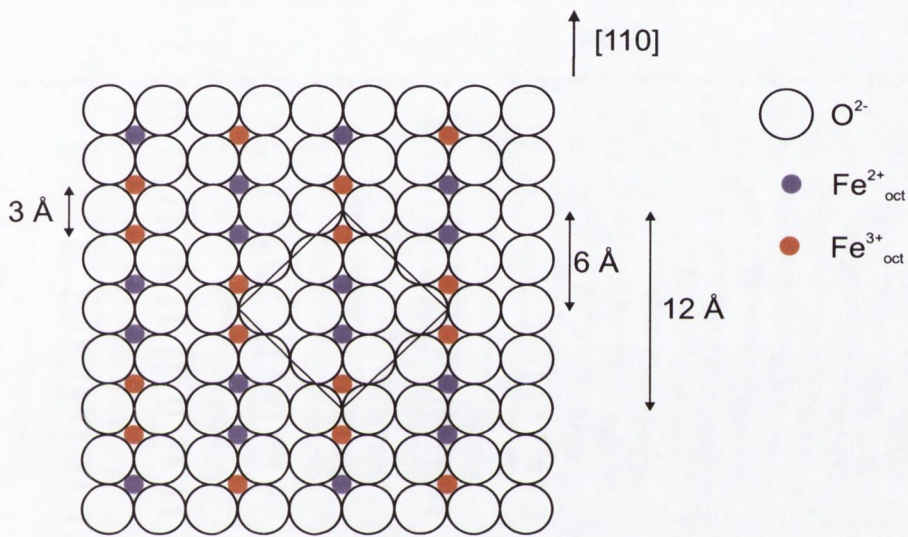


Figure 7.12: The (001) surface of Fe_3O_4 terminated at the octahedral plane. This schematic model reproduces the structure observed in fig. 7.6. Pairs of Fe^{2+} and Fe^{3+} ions run along the $[110]$ direction. The $(\sqrt{2} \times \sqrt{2})R45^\circ$ reconstructed unit cell may be due to the charge ordering. The 6 \AA and 12 \AA periodicities observed by STM measurements are shown.

a short-range order, possibly due to the presence of defects on the crystal surface and to its off-stoichiometry [78].

Non-magnetic tips are expected to show a 3 Å periodicity along the Fe rows. This would provide definite evidence that the 12 Å periodicity observed with ferromagnetic or antiferromagnetic tips is caused by a spin-polarized mechanism. Although the great majority of STM sessions was carried out using chemically etched, non-magnetic W tips, atomic resolution was never obtained. Atomic rows on the *B*-sublattice were imaged by Wiesendanger *et al.* [78] using chemically etched W tips, but the corrugation amplitude was below the noise level and no periodicity was observed. Koltun *et al.* [104] were also unable to achieve atomic resolution on the *B*-sublattice using in situ torn W and PtIr tips.

Chapter 8

Summary

8.1 Conclusion

The (001) surface of Fe_3O_4 has been studied using STM, LEED and AES. The bulk properties of the artificial single crystal have been characterized by means of XRD and resistance vs. temperature measurements. The [001] lattice constant was measured to be $8.398 \pm 0.010 \text{ \AA}$, which is in good agreement with the predicted value. A Verwey transition temperature of 110 K was determined, indicating a slight sub-stoichiometry of the crystal. During this study it was found that the preparation of a crystal by means of annealing in UHV results in the contamination and reduction of the surface. Under the typical preparation conditions – annealing in UHV at $\sim 1000 \text{ K}$ for 4-60 hours – AES indicated the presence of contaminants on the surface, mainly Ca and K. The onset of a $p(1 \times 4)$ reconstruction with domains oriented by 90° with respect to each other was observed by LEED, while the surface topography observed with STM showed terraces with edges aligned along the $\langle 110 \rangle$ directions. The terraces were separated by $\sim 1.0 \text{ \AA}$ and were covered by rows running along the $[110]$ and $[1\bar{1}0]$ directions. It was found

that further annealing led to an increase in the Ca concentration and a simultaneous decrease in the concentration of K on the surface; this change was accompanied by the formation of more regular rows on the terraces, whose average periodicity was measured to be 26 \AA , in good agreement with the $p(1 \times 4)$ reconstruction observed by LEED. The driving force of the $p(1 \times 4)$ reconstruction is thought to be the segregation of Ca from the bulk to the surface of the crystal, leading to the formation of a $\text{Ca}_x\text{Fe}_{3-x}\text{O}_4$ -like compound on the surface.

A novel preparation procedure has been developed in the course of this study. The crystal was at first annealed in UHV at $\sim 1030 \text{ K}$ for periods of time ranging between 20 and 120 hours and subsequently annealed at $\sim 990 \text{ K}$ in oxygen atmosphere (the typical exposures ranged between 3600 L and 7200 L); it was then sputtered with Ar^+ ions and annealed again in UHV at $\sim 990 \text{ K}$ for 2-10 hours. No contaminants could be detected by AES on a surface prepared in this fashion; furthermore, the lineshape of the low energy iron peaks coincides with the one of the reference Auger spectrum for magnetite [89], indicating that no other Fe oxides, *e.g.* FeO or Fe_2O_3 are present on the surface. A surface prepared in this fashion always gave rise to a sharp $(\sqrt{2} \times \sqrt{2})R45^\circ$ reconstruction as shown by LEED, in agreement with the results from other groups for a clean (001) magnetite surface.

The $(\sqrt{2} \times \sqrt{2})R45^\circ$ reconstructed surface has been studied by means of STM using non-magnetic W and PtIr tips and antiferromagnetic MnNi tips. The surface is characterized by the presence of square and rectangular terraces with edges aligned along the $\langle 110 \rangle$ directions; the step height between adjacent terraces is an integer multiple of $2.1 \pm 0.2 \text{ \AA}$, corresponding to the separation between A - A or B - B planes. We addressed the controversy regarding the termination of a $\text{Fe}_3\text{O}_4(001)$ surface, proving that it is terminated

at the B plane, exposing oxygen ions and octahedrally coordinated Fe ions. Atomic resolution on this surface has not been achieved using non-magnetic tips, while we obtained atomic scale contrast using antiferromagnetic MnNi tips. Two different structures have been imaged by STM, showing rows of Fe atoms running along the $[110]$ direction. The 3 \AA periodicity along the $[110]$ direction on the Fe rows, expected for the (001) bulk-terminated surface of magnetite, has not been observed; a 6 \AA and a 12 \AA periodicity has been imaged instead. This anomalous periodicity has been explained in terms of a "Wigner localization" on the surface, leading to a static arrangement of pairs of Fe^{2+} and pairs of Fe^{3+} ions. The two Fe species may be distinguished using a probe sensitive to the different spin polarization of Fe^{2+} and Fe^{3+} ions; the antiferromagnetic MnNi tips used during this study are in principle capable of providing magnetic contrast, and the different corrugation observed along the $[110]$ Fe rows has been attributed to a magnetic rather than a topographic effect. We have proposed a model according to which the driving force inducing the $(\sqrt{2} \times \sqrt{2})R45^\circ$ reconstruction is due to the charge ordering at the surface and not to an array of oxygen vacancies.

8.2 Further work

The characterization of the crystals used in this study has been carried out using an X-ray powder diffractometer and a resistance vs. temperature setup. Although XRD can give useful information about the crystal structure, a powder diffractometer is a bulk-sensitive technique and does not provide any information about the surface. A new set-up to analyze single crystals will soon be available in the group; this system will have the possibility of performing XRD at a grazing incident angle, providing information about the

crystal structure of the surface. Concerning the resistance vs. temperature measurements, the set-up used in this study did not have the possibility of applying an external magnetic field at the crystal. A commercial closed cycle refrigerator system has been recently purchased from Janis Research Company, Inc. [108] to perform resistance vs. temperature measurements; this setup will be modified by A. Cazacu by adding a magnet that will permit one to perform magneto-resistance experiments; this instrument will prove important to determine the Verwey transition temperature of magnetite crystals.

An anomalous periodicity on the Fe rows along the [110] direction has been observed using MnNi tips, and a spin polarized effect has been suggested. Although MnNi is known to be a bulk antiferromagnet at room temperature, making MnNi tips a potential candidate for SPSTM, no characterization of the magnetic properties of the tip apex has been done; this will be essential for a better understanding of the contrast mechanism in STM images. The $(\sqrt{2} \times \sqrt{2})R45^\circ$ reconstruction observed on a clean magnetite surface has been attributed to a Verwey freezing at the surface. The soundness of this hypothesis may be proved by determining the actual Verwey transition temperature at the surface; the disappearance of the $(\sqrt{2} \times \sqrt{2})R45^\circ$ mesh would be induced by heating the crystal above the critical temperature. A magnetic characterization of the crystal surface will also play an important role; a surface magneto-optical Kerr effect set-up, designed by L. Seravalli [109] and implemented by V. Oussov will provide a better understanding of the magnetic properties at the surface of the crystals. The effects of a magnetic field on a magnetite surface can be investigated using the electro-magnet placed in our STM chamber. Although the current set-up is not ideal to carry out experiments in a magnetic field, due to the presence

of magnetic components –(e.g. nickel springs in tip and sample holders)– in the STM head, the ability to achieve atomic resolution in an external field could provide a decisive insight into understanding the mechanism behind the observed surface reconstruction. Scanning Tunneling Spectroscopy (STS) is a powerful tool in the study of a magnetite surface; for example, it would allow us to distinguish between the two different iron species on the surface, the tetrahedrally and octahedrally coordinated Fe ions. The use of STS during this study has been hindered by thermal drift effects, which constitute a major problem at room temperature. A low temperature STM should be in operation in the next year and will allow us to perform spectroscopic measurements.

The exposure of magnetite crystals to oxygen gas has been used in this study, proving to be an essential ingredient in the preparation of a clean surface. A range of experiments, such as the exposure of magnetite crystals to hydrogen and oxygen gas, can be performed to study the effects of the reduction and oxidation of the surface. The growth of Fe films on a magnetite surface is another area of interest, and the new e-beam evaporator recently purchased by Omicron GmbH [34] will allow us to carry out these type of experiments.

Appendix A

Heater calibration curve

Figure A.1 shows the calibration curve for the resistive heater. A *K*-type thermocouple was spot-welded to the face of an upside-down sample-holder. The calibration was carried out by Dr. C. Seoighe and the author.

A. Heater calibration curve

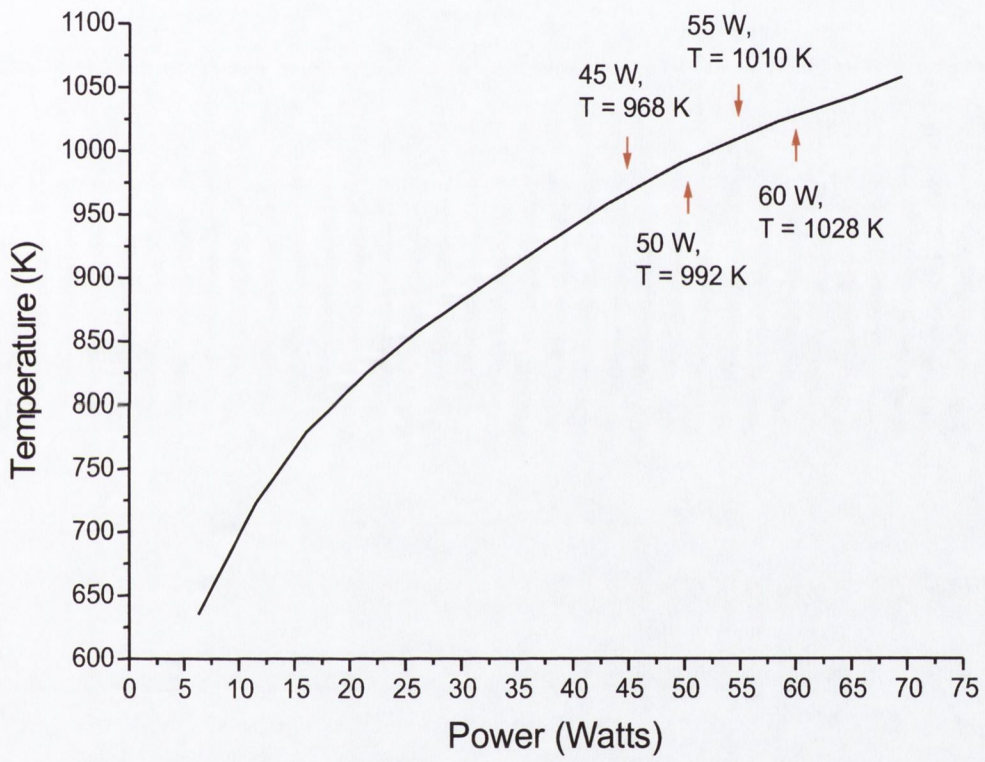


Figure A.1: Resistive heater calibration curve.

Appendix B

STM calibration

The scanner used in our STM is a piezo-ceramic tube sectioned into four outer Ag electrodes which carry the $Z-X$, $Z+X$, $Z-Y$ and $Z+Y$ voltages, while the inner electrode is grounded. It was produced by Staveley Sensors Inc. [110] using *EBL 2 (PZT 5A)* ceramic. The scanner has a 6.35 mm outer diameter, a 0.51 mm wall thickness and a 14 mm length. It has a dynamic range of ± 13000 Å in the z -direction and ± 20600 Å in the x - and y - directions; the z - voltage ranges from -140 V to $+140$ V and the x - and y - voltages range from -60 V to $+60$ V. These ranges were calibrated on Cu(100) monoatomic steps and HOPG atomic resolution images respectively by Dr. A. Quinn [11]. A 10 % error in the x -, y - and z - directions was estimated.

In the course of this thesis the original STM control unit – a TOPS II system by WA Technology [33] – was replaced with a SCALA system by Omicron GmbH [34]. Although the displacements depend only by the geometry and material of the scanner and by the voltage applied to it, a new set of measurements on HOPG was performed in order to verify the calibration in the x - and y - directions; terraces on $\text{Fe}_3\text{O}_4(001)$ and monoatomic steps on Mo(110) were used to verify the z - calibration.

Creep and drift effects are commonly encountered in STM. The unwanted displacement of the tip or sample during scanning results in a distortion that must be taken into account when analyzing topographic images. Piezo creep can be described as a dimensional stabilization that takes place following a change in voltage. A step change in the applied voltage (*e.g.* at the beginning of a scan or when the x -, y - or z - offset is changed) will produce a rapid deformation (typically in a fraction of a millisecond), followed by a smaller change on a much longer time scale. To reduce this effect, a scan following a change in the offset was usually aborted after a few lines. Thermal drift can greatly affect STM measurements if they are not carried out in thermal equilibrium. A long time (usually 1-3 hours) was required by the TOPS II controller to achieve tunneling, allowing the STM to reach thermal equilibrium; when this is the case, most of the distortion effects are due to creep. However, one experiment carried out by Dr. A. Quinn where tunneling was achieved one hour after an iron film had been deposited on Cu(111) at a substrate temperature around 570 K, showed a drift an order of magnitude greater than typical creep values [11]. The approaching time with the SCALA controller is significantly shorter than with the TOPS II system; tunneling was routinely achieved after 10-30 minutes. A combination of creep and thermal drift effects often resulted in distorted images.

Fig. B.1 shows a $(30 \times 30) \text{ \AA}^2$ image of HOPG. This image was scanned in constant current mode using an electro-chemically etched W tip, a sample bias of 100 mV and a tunneling current of 4 nA. This high resolution image shows a significant distortion of the hexagonal symmetry. A black hexagon is drawn on the surface to facilitate the identification of the distorted hexagonal symmetry. Although the time required to achieve tunneling was very short, the scanning session lasted over three hours, and during this period several

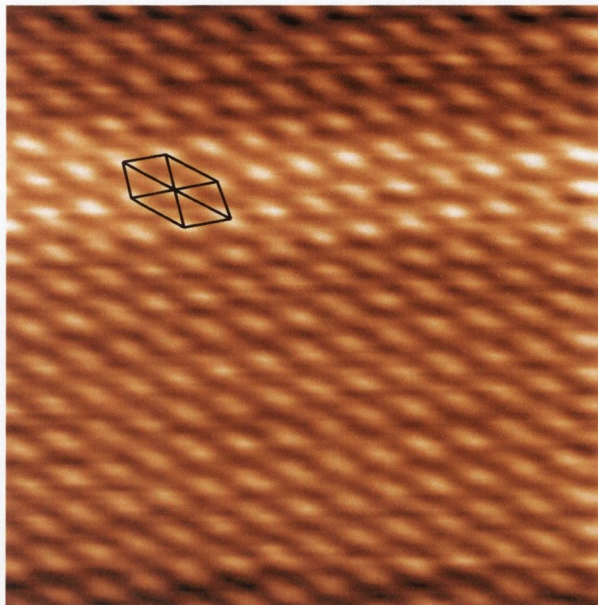


Figure B.1: $(30 \times 30) \text{ \AA}^2$ image of HOPG. The image was acquired at a sample bias of 100 mV and a tunneling current of 4 nA using a W tip.

atomically resolved images were recorded under very different measurement conditions. Positive and negative sample bias of 50 mV and 100 mV were used, as well as tunneling currents of 2, 3 and 4 nA. The scanning speed and the feedback loop gain were varied trying to optimize resolution and stability. Despite all these efforts, all the images showed significant distortion. Given the long duration of the scanning session, we attribute the main responsibility of the distortion to piezo creep.

To verify the calibration of the scanner along the x - and y - directions, image B.1 was warped so that an hexagonal symmetry was obtained; the warped image is shown in fig. B.2. The interatomic spacing measured after the warping was 2.37 \AA , that is $\sim 4 \%$ smaller than the expected value of 2.46 \AA .

The calibration of the scanner along the z - direction was carried out

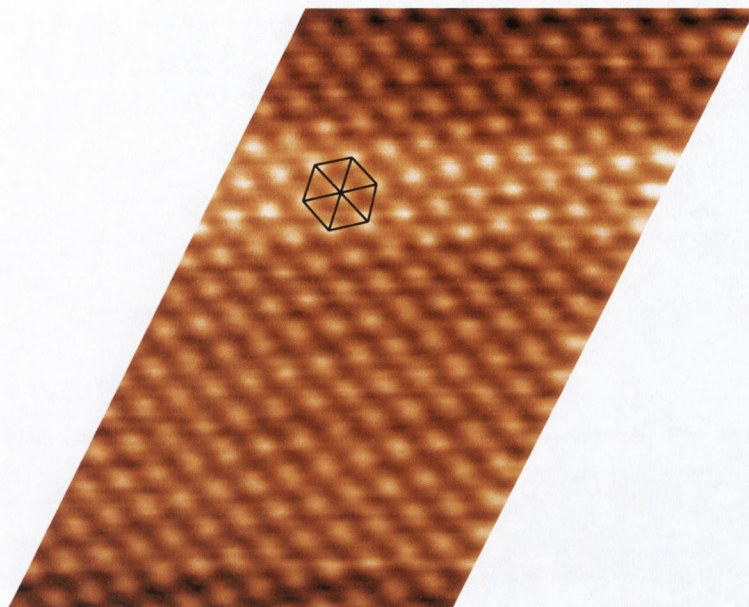


Figure B.2: The original (30×30) \AA^2 image was warped to obtain an hexagonal symmetry.

measuring the step height of terraces on a clean $\text{Fe}_3\text{O}_4(001)$ surface. The step height is expected to be 2.1 \AA or an integer multiple of 2.1 \AA , which corresponds to the separation between A - A or B - B planes. The average measured step height was 2.1 \AA , in excellent agreement with the predicted value. An independent checking was performed by D. Mac Mathúna using the monoatomic steps on a clean $\text{Mo}(110)$ surface as a reference. A value of 2.1 \AA was found instead of the expected 2.2 \AA , indicating an error of $\sim 5 \%$. The results discussed above indicate that the original calibration of the scanner was accurate. An error of approximately 10% is allowed in the x -, y - and z - values.

Bibliography

- [1] M. Johnson and J. Clarke. *J. Appl. Phys.*, 67:6141, 1990.
- [2] A.A. Minakov and I.V. Shvets. *Surf. Sci.*, 236:L377, 1990.
- [3] G. Güntherodt R.J. Gambino R. Wiesendanger, H.J. Güntherodt and R. Ruf. *Phys. Rev. Lett.*, 65:247, 1990.
- [4] R. Wiesendanger, I.V. Shvets, D. Bürgler, G. Tarrach, H.J. Güntherodt, J.M.D. Coey, and S. Gräser. *Science*, 255:583, 1992.
- [5] D. Bürgler G. Tarrach H.J. Güntherodt R. Wiesendanger, I.V. Shvets and J.M.D. Coey. *Europhys. Lett.*, 19(2):141, 1992.
- [6] G. Nunes and N.M. Amer. *Appl. Phys. Lett.*, 63:1851, 1993.
- [7] M.W.J. Prins D.L. Abraham R. Jansen, M.C.M.M. van der Wielen and H. van Kempen. *J. Vac. Sci. Technol. B*, 12(3):2133, 1994.
- [8] R. Jansen M.W.J. Prins and H. van Kempen. *Phys. Rev. B*, 53:8105, 1996.
- [9] E.J.W. Verwey, P.W. Haayman, and R. Romeyn. *J. Chem. Phys.*, 15(4):181, 1947.
- [10] A. Yanase and K. Siratori. *J. Phys. Soc. Jpn.*, 53:312, 1984.

- [11] A. Quinn. *Development of an ultra-high vacuum scanning tunneling microscope*. PhD thesis, Physics Department, Trinity College Dublin, July 1996.
- [12] J. Osing. *Studies towards spin sensitive scanning tunneling microscopy*. PhD thesis, Physics Department, Trinity College Dublin, October 1998.
- [13] S. Murphy. *Surface studies of the Fe/Mo(110) and Fe/W(100) epitaxial systems*. PhD thesis, Physics Department, Trinity College Dublin, October 2000.
- [14] VAT Vacuum Products Ltd., 235 Regents Park Road, Finchley, London, N3 3LG U.K.
- [15] Physical Electronics Inc. (formerly Perkin-Elmer), 6509 Flying Cloud Drive, Eden.
- [16] Vacuum Generators, Maunsell Road, Castleham Industrial Estate, Hastings, East Sussex TN389NN, UK.
- [17] Caburn MDC Ltd. *The Old Dairy, The Street, Glynde, East Sussex BN8 6SJ, UK*.
- [18] Leybold Inficon Inc., Two Technology Place, East Syracuse, NY 13057-9714 U.S.A.
- [19] VG Microtech, The Birches Industrial Estate, Imberhorne Lane, East Grinstead, West Sussex RH19 1UB U.K.
- [20] Pfeiffer Vacuum GmbH, Emmeliusstrasse, D-35614 Asslar.
- [21] D.M. Hoffman, B. Singh, and J.H. Thomas III. *Handbook of vacuum science and technology*. Academic Press, London, 1998.

- [22] SAES Getters G.B. Ltd., 5 Suthern Court, South Street, Reading, Berkshire RG1.
- [23] OMEGA Engineering Inc. One Omega Drive P.O. Box 4047 Stamford, CT 060907-0047, U.S.A.
- [24] C. Seoighe. *Surface studies of magnetite (100)*. PhD thesis, Physics Department, Trinity College Dublin, October 2000.
- [25] IRCON Inc., 7301 North Caldwell Avenue, Niles, Illinois 60648 U.S.A.
- [26] J.C. Vickerman, editor. *Surface Analysis: The Principal Techniques*. Wiley, New York, 1997. Section 5.3.
- [27] C. Julian Chen. *Introduction to scanning tunneling microscopy*. Oxford University Press, New York, 1993.
- [28] R. Wiesendanger. *Scanning Probe Microscopy and Spectroscopy*. Cambridge University Press, Cambridge, 1994.
- [29] J. Bardeen. *Phys. Rev. Lett.*, 6:57, 1961.
- [30] S.H. Pan. Piezo electric motor. International patent publication No WO93/19194, 1993. Inetrnational bureau, World Intellectulal Property Organisation.
- [31] G. Mariotto, M. D'Angelo, and I.V. Shvets. *Rev. Sci. Instrum.*, 70(9), 1999.
- [32] G. Mariotto, M. D'Angelo, Y. Kresnin, and I.V. Shvets. *Appl. Surf. Sci.*, 144-145, 1999.
- [33] SPM-Group Oxford Instruments, Chesterton Mills, French's Road, Cambridge, CB4 3NP, UK.

-
- [34] Omicron Vakuumphysik. Idsteiner Str.78, D-65232 Taunusstein, Germany.
- [35] Molecular Devices and Tools for NanoTechnology. 103460 Moscow, State Research Institute of Physical Problems, Russia.
- [36] Nanotec Electronica. c/ Padilla, 3. 1 D 28006-Madrid SPAIN.
- [37] M.A. Van Hove, W.H. Weinberg, and C.-M. Chan. *Low-Energy Electron Diffraction*, volume 6 of *Springer Series in Surface Science*. Springer-Verlag, Berlin.
- [38] Physical Electronics. Technical Manual, Model 10-155/15-155 Cylindrical Mirror Analyser.
- [39] D.P. Woodruff and T.A. Delchar. *Modern Techniques of Surface Science*. Cambridge Solid State Series. Cambridge University Press, second edition, 1994.
- [40] Stanford Research Systems, 1290-D Reamwood Ave., Sunnyvale, California, 94089 U.S.A.
- [41] Galileo Corporation, Galileo Park, P.O. Box 550, Sturbridge, MA 01566 U.S.A.
- [42] L.E. Davis, N.C. MacDonald, P.W. Palmberg, G.E. Riach, and R.E. Weber. *Handbook of Auger Electron Spectroscopy*. Physical Electronics Industries, Minnesota, second edition, 1976.
- [43] G.E. McGuire. *Auger Electron Spectroscopy Reference Manual*. Plenum Press, New York, 1979.

-
- [44] J.P. Ibe, P.P. Bey Jr., S.L. Brandow, R.A. Brizzolara, N.A. Burnham, D.P. DiLella, K.P. Lee, C.R.K. Marrian, and R.J. Colton. *J. Vac. Sci. Technol. A*, 8(4):3570, 1990.
- [45] Y. Nakamura, Y. Mera, and K. Maeda. *Rev. Sci. Instr.*, 70, 1999.
- [46] K. Dickmann, F. Demming, and J. Jersch. *Rev. Sci. Instrum.*, 67, 1996.
- [47] H. Bourque and R. M. Leblanc. *Rev. Sci. Instrum.*, 66, 1995.
- [48] B. Hacker, A. Hillebrand, T. Hartmann, and R. Guckenberger. *Ultra-microscopy*, pages 42–44, 1992.
- [49] I.V. Shvets, R. Wiesendanger, D. Burgler, G. Tarrach, H.J. Guntherodt, J.M.D. Coey, and S. Graser. *J. Appl. Phys.*, 71:5489, 1992.
- [50] S. Murphy, J. Osing, and I.V. Shvets. *J. Magn. Magn. Mat.*, 198-199:686, 1999.
- [51] S. Murphy, J. Osing, and I.V. Shvets. *Appl. Surf. Sci.*, 144-145:497, 1999.
- [52] J. Osing, S. Murphy, and I.V. Shvets. *Surf. Sci.*, 454:280, 2000.
- [53] R.M. Cornell and U. Schwertmann. *The Iron Oxides*. Verlagsgellschaft mbH, 1996.
- [54] A. Muan and E.F. Osborn. *Phase Equilibria Among Oxides in Steel-making*. Addison-Wesley Publishing Company, Inc., 1965.
- [55] M.S. Seehra and G. Srinivasan. *J. Phys. C*, 17, 1984.
- [56] R. W. G. Wyckoff. *Crystal structures*. Second edition edition, 1964.
- [57] E.J.W. Verwey and J.H. de Boer. *Rec. Trav. Chim.*, 55:531, 1936.

-
- [58] R. Aragon C.J. Sandberg J.M. Honig J.P. Shepherd, J.W. Koenitzer. *Phys. Rev. B*, 31 (2):1107, 1985.
- [59] F.C. Voogt. *NO₂-assisted molecular beam epitaxy of iron oxide films*. PhD thesis, University of Groningen, 1998.
- [60] A. Ramdani, J. Steinmetz, C. Gleitzer, J.M.D. Coey, and J.M. Friedt. *J. Phys. Chem. Solids*, 48:217, 1987.
- [61] W.H. Bragg. *Nature*, 95:561, 1915.
- [62] P.W. Tasker. *J. Phys. C: Solid State Phys.*, 12:4977, 1979.
- [63] P.W. Tasker. *Phil. Mag. A*, 39(2):119, 1979.
- [64] F. Bertaut. *Compt. Rendu*, 246:3447, 1958.
- [65] F.M.F. de Groot, M. Grioni, J.C. Fuggle, J. Ghijsen, G.A. Sawatzky, and H. Petersen. *Phys. Rev. B*, 40(8):5715, 1989.
- [66] A. Barbieri, W. Weiss, M.A. Van Hove, and D.A. Somorjai. *Surf. Sci.*, 302:259, 1994.
- [67] M.D. Pashley. *Phys. Rev. B*, 40(15):10481, 1989.
- [68] J.P. LaFemina. *Crit. Rev. in Surf. Chem.*, 3:297, 1994.
- [69] B. Stanka, W. Hebenstreit, U. Diebold, and S.A. Chambers. *Surf. Sci.*, 448:49, 2000.
- [70] G. Tarrach, D. Bürgler, T. Schaub, R. Wiesendanger, and H.J. Güntherodt. *Surf. Sci.*, 285:1, 1993.

-
- [71] J.M. Gaines, P.J.H. Bloemen, J.T. Kohlhepp, C.W.T. Bulle-Lieuwma, R.M. Wolf, R.M. Reinders, R.M. Jungblut, P.A.A. van der Heijden, J.T.W.M. van Eemeren, J. aan de Stegge, and W.J.M. de Jonge. *Surf. Sci.*, 373:85, 1997.
- [72] Y.J. Kim, Y. Gao, and S.A. Chambers. *Surf. Sci.*, 371:358, 1997.
- [73] S.A. Chambers and S.A. Joyce. *Surf. Sci.*, 420:111, 1999.
- [74] S.A. Joyce S.A. Chambers, S. Thevuthasan. *Surf. Sci.*, 450:L273, 2000.
- [75] Y. Gao and S.A. Chambers. *Journal of Crystal Growth*, 174:446, 1997.
- [76] D.O. Boerma A.V. Mijiritskii, M.H. Langelaar. *J. Magn. Magn. Mat.*, 211:278, 2000.
- [77] P.J.M. Smulders L. Niesen M.A. James F.C. Voogt, T. Fujii and T. Hibma. *Phys. Rev. B*, 60:11193, 1999.
- [78] R. Wiesendanger, I.V. Shvets, and J.M.D. Coey. *J. Vac. Sci. Technol. B*, 12(3):2118, 1994.
- [79] A.R. Felmy J.R. Rustad, E. Wasserman. *Surf. Sci. Lett.*, 432:L583, 1999.
- [80] J.E. Keem H.R. Harrison, R. Aragon and J.M. Honig. *Inorg. Synth.*, 22:43, 1984.
- [81] Prof. Honig. *Purdue University, Indiana, USA*.
- [82] RTI GmbH, Technologiepark 12, Paderborn, D-33100.
- [83] Surface Preparation Laboratory, Penniweg 69 F, 1507 DE Zaandam, The Netherlands.

-
- [84] R. Aragon, R.J. Rasmussen, J.P. Shepherd, J.W. Koenitzer, and J.M. Honig. *J. Magn. Magn. Mat.*, 54-57:1335, 1986.
- [85] M. Aeschlimann, G.L. Bona, F. Meier, M. Stampanoni, and H.C. Siegmann. *Appl. Phys. Lett*, 49(13):824, 1986.
- [86] J.F. Anderson, M. Kuhn, H. Diebold, K. Shaw, P. Stoyanov, and D. Lind. *Phys. Rev. B*, 56:9902, 1997.
- [87] R. Jansen, V.A.M. Brabers, and H. van Kempen. *Surf. Sci.*, 328, 1995.
- [88] M. Seo, J.B. Lumsden, and R.w. Staehle. *Surf. Sci.*, 50:541, 1975.
- [89] J.T. Yates V.S. Smentkowski. *Surf. Sci.*, 232:113–128, 1990.
- [90] D. Briggs and M.P. Seah. *Auger and X-ray Photoelectron Spectroscopy*, volume 1 of *Practical Surface Analysis*. Wiley, New York, second edition, 1990.
- [91] C. Ruby, J. Fusy, and J M R Genin. *Thin Solid Films*, 352:22–28, 1999.
- [92] O.L.J. Gijzeman H. den Daas and J.W. Geus. *Surf. Sci.*, 290:26–34, 1993.
- [93] W.D. Kingery A. Roshko. *J. Am. Ceram. Soc.*, 68:C–331, 1985.
- [94] M.R. McCartney J.M. Cowley Gajdardziska-Josifovska, P.A. Crozier. *Surf. Sci.*, 284:186, 1993.
- [95] T. Aizawa W. Hayami K. Oyoshi S. Hishita R. Souda, Y. Hwang. *Surf. Sci.*, 387:136, 1997.
- [96] U. Diebold L.P. Zhang, M. Li. *Surf. Sci.*, 412-413:242–251, 1998.

-
- [97] K-O Ng U. Diebold, J.F. Anderson and D. Vanderbilt. *Phys. Rev. Lett.*, 77:1322, 1996.
- [98] S.F. Alvarado, M. Erbudak, and P. Munz. *Phys. Rev. B*, 14:2740, 1976.
- [99] E. Wigner. *Trans. Faraday Soc.*, 34:678, 1938.
- [100] R. Wiesendanger J.M.D. Coey, I. V. Shvets and H.-J. Güntherodt. *J. Appl. Phys.*, 73:6742, 1993.
- [101] J.C. Slonczewski. *J. Physique C*, 8:1629, 1988.
- [102] J.C. Slonczewski. *Phys. Rev. B*, 39:6995, 1989.
- [103] D. Bürgler G. Tarrach H.-J. Güntherodt R. Wiesendanger, I.V. Shvets and J.M.D. Coey. *Z. Phys. B - Cond. Matt.*, 86:1, 1992.
- [104] G. Güntherodt V.A.M. Brabers R. Koltun, M. Herrmann. *Appl. Phys. A*, 73:49–53, 2001.
- [105] S. Iida, K. Mizushima, M. Mizuguchi, K. Kose, K. Kato, K. Yanai, N. Goto, and S. Yumoto. *J. Appl. Phys.*, 53(3):2164, 1982.
- [106] S. Iida, M. Mizoguchi, N. Goto, and Y. Motomura. *J. Magn. Magn. Mat.*, 31-34:771, 1983.
- [107] E. Kita, Y. Tokuyama, A. Tasaki, and K. Siratori. *J. Magn. Magn. Mat.*, 31-34:787, 1983.
- [108] Janis Research Company, Inc., 2 Jewel Drive, Wilmington, MA, USA.
- [109] L. Seravalli. Design and development of a smoke steep. Master's thesis, Physics Department, Trinity College Dublin, September 2000.

- [110] Staveley Sensors Inc., 91 Prestige Park Circle, East Hartford, CT 06108, USA.